

**A PARTICLE-BASED MULTI-SCALE SIMULATION PROCEDURE  
WITHIN THE MATERIAL POINT METHOD FRAMEWORK**

---

A Dissertation

presented to

the Faculty of the Graduate School

at the University of Missouri-Columbia

---

In Partial Fulfillment

of the Requirements for the Degree

Doctor of Philosophy

---

by

**SHAN JIANG**

Dr. Zhen Chen, Dissertation Supervisor

MAY 2014

© Copyright by Shan Jiang 2014

All Rights Reserved

The undersigned, appointed by the dean of the Graduate School, have examined the dissertation entitled

A PARTICLE-BASED MULTI-SCALE SIMULATION PROCEDURE WITHIN THE  
MATERIAL POINT METHOD FRAMEWORK

presented by Shan Jiang,

candidate for the degree of doctor of philosophy

and hereby certify that, in their opinion, it is worthy of acceptance.

---

Professor Zhen Chen

---

Professor Sam A. Kiger

---

Professor Hani A. Salim

---

Professor Hao Li

---

Professor Thomas D. Sewell

.....Dedicated to *Aiden* and *Xin*, for their love and encourage.

.....Thanks, Mom and Dad.

## ACKNOWLEDGEMENTS

I am very proud to be at the close of my Ph.D. studies at University of Missouri and it is very important to me to recognize all the people who helped me dig into the research topics through to the end. Although it would be difficult to name every single person for his/her assistance, encouragement and support, I would like to express my sincere appreciation to each of them.

I would like to thank Dr. Zhen Chen for his great friendship, understanding and encouragement. Without his guidance and inspiration, I would never explore this far on the academic road. The period of my doctoral studies under the supervision of Dr. Chen in the Department of Civil & Environmental Engineering was a wonderful time in my life.

I would also like to express my gratitude to Dr. Thomas Sewell, and Dr. Donald Thompson from Chemistry Department, for their valuable suggestions, comments, and time put into the process. To me, they are like another two co-advisors and their professional writing and editing made our journal articles finally got published with high quality.

Also, I would thank other members of my Ph.D. committee including Dr. Sam Kiger, Dr. Hani Salim and Dr. Hao Li for their sincere help in many areas and at different stages of my graduate study. Meanwhile, I am also grateful to my professors and colleagues, Dr. Yuwen Zhang, Dr. Yuyi Lin, Dr. J. K. Chen, Dr. Vellore Gopalaratnam, Dr. Frank Pai, Dr. Robert Winholtz, Dr. Uee Cho, Dr. Hongwu Zhang, Dr. Yonggang

Zheng, Dr. Yong Gan, Dr. Yonggang Shen, Dr. Suleiman Oloriegbe, Dr. Youqing Yang, Dr. Luming Shen and Dr. Hantao Liu for their helpful instructions and discussions during my study.

Finally I would express my special thanks to the support by the U. S. Defense Threat Reduction Agency under grant number HDTRA1-10-1-0022, the National Natural Science Foundation of China under grant No.11232003, and the University of Missouri Bioinformatics Consortium for providing the Lewis supercomputing-cluster systems.

## TABLE OF CONTENTS

ACKNOWLEDGEMENTS.....	ii
LIST OF ILLUSTRATIONS.....	viii
LIST OF TABLES.....	xiv
LIST OF ABBREVIATIONS.....	xv
ABSTRACT.....	xvi
CHAPTER 1. INTRODUCTION.....	1
1.1    Research Background.....	1
1.1.1    Multi-Scale Simulation.....	1
1.1.2    The Material Point Method.....	4
1.2    Objective of Research.....	6
1.3    Outline of Dissertation.....	7
CHAPTER 2. GOVERNING EQUATIONS AND METHODOLOGY.....	9
2.1    Molecular Dynamics at the Atomic Scale.....	9
2.2    Dissipative Particle Dynamics at the Mesoscale Level.....	11
2.3    Material Point Method at the Continuum Level.....	13
2.4    A Particle-Based Multi-Scale Simulation Procedure.....	18
2.4.1    Initialization and Computational Set-Up.....	20
2.4.2    Scheme of the Concurrent DPD/MPM Simulation.....	21
2.4.3    Interface Treatment between the DPD and MPM Regions.....	25
2.5    Summary.....	26

CHAPTER 3. ATOMISTIC MODELING AND SIMULATION OF METALLIC NANOSTRUCTURES UNDER DYNAMIC AND IMPACT LOADING .....	28
3.1    Introductory Remarks .....	28
3.2    Mechanical Response of Nanowires under Dynamic Loading.....	31
3.2.1 Tension/Torsion and Loading Path Effect.....	32
3.2.2 Deformation Mechanism.....	38
3.2.3 Formation of Special Nanostructures .....	41
3.3    Impact Response of Nanostructures.....	52
3.3.1 Transverse Impact .....	55
3.3.2 Longitudinal Impact .....	65
3.4    Summary .....	72
CHAPTER 4. ATOMISTIC MODELING AND SIMULATION OF NANOPARTICLE INCLUSIONS IN FLUID UNDER HIGH PRESSURE .....	75
4.1    Introductory Remarks .....	75
4.2    Computational Set-up for the Particle-Fluid Model .....	77
4.3    Pressure-Volume Relationship.....	78
4.4    Nanostructural Transition .....	80
4.5    Summary .....	86
CHAPTER 5. MULTI-SCALE SIMULATION OF NANOSTRUCTURES UNDER DYNAMIC AND IMPACT LOADING .....	88
5.1    Introductory Remarks .....	88
5.2    Coupled DPD/MPM-Grid Model .....	91
5.2.1 Impact Test.....	91

5.2.2 Tension Test .....	94
5.3 Concurrent DPD/MPM Model.....	98
5.3.1 Impact Test.....	98
5.3.2 Tension Test .....	101
5.4 Summary .....	106
CHAPTER 6. MULTI-SCALE SIMULATION OF NANOSTRUCTURE ASSEMBLY IN CONFINING FLUID.....	107
6.1 Introductory Remarks .....	107
6.2 Computational Set-up .....	108
6.2.1 Single Inclusion in Confining Fluid .....	108
6.2.2 Particle/Rod Assembly in Confining Fluid .....	110
6.3 Pressure-Volume Relationship.....	113
6.4 Particle/Rod Assembly in Confining Fluid.....	115
6.5 Summary .....	129
CHAPTER 7. CONCLUSION AND FUTURE WORK .....	131
7.1 Summary of the Work.....	131
7.2 Major Findings.....	132
7.3 Recommendations and Future Work .....	135
APPENDIXES .....	138
Appendix 1. Units used for the Concurrent DPD/MPM Model .....	138
Appendix 2. One-Dimensional MPM and DDMP Code for Wave Propagation .....	138
Appendix 3. Publications Related to MD/DPD/MPM/FEM by the Author .....	148
REFERENCES .....	150

Vita.....161

## LIST OF ILLUSTRATIONS

Figure	Page
Figure 2.1 Schematic of the concurrent DPD/MPM modeling. If needed, the computational domain can be divided to several regions with different types of particles, namely, mesoscale/DPD region, classical MPM region, and intermediate region. ....	18
Figure 3.1 Sketch and different loading procedures of (a) pre-tensile torsion and (b) pre-torsional tension on a square cross-section nanowire. The geometry of the wire is characterized by the length $l$ and cross-sectional length $l_c$ . (Jiang et al. 2010).....	33
Figure 3.2 Critical angle pre unit length as a function of temperature for the nanowire with the size of $40a \times 10a \times 10a$ under different pre-tensile strain at 300K. (Jiang et al. 2010) .....	34
Figure 3.3 (a) Yield stress as a function of temperature of the $40a \times 10a \times 10a$ nanowire under tension after various angles of pre-torsion. (b) Scatter plots for determination of Young's modulus for tension after various pre-torsion at 300 K. (Jiang et al. 2010) .	37
Figure 3.4 (a) Nucleation of partial dislocation from the corner of the free surface due to the atomic displacement mismatch and (b) partial dislocation propagation in several close-packed planes, resulting stacking faults lie in these planes. In this figure and Fig.3.5, fcc atoms are shown as white, hcp atoms are as green, disordered atoms are shown in red. The nanowire was subject to a bending load. (Zheng et al. 2009) .....	39
Figure 3.5 (a) Twinning process: (a) a partial is emitted from surface and (b) spreads in the bulk of nanowire, forming a twin by separating the hcp layers of an extrinsic stacking fault; (c) another partial of the same type is emitted and (d) propagates in the bulk, broadening the twin. (Zheng et al. 2009).....	40
Figure 3.6 Schematic diagram of the simulation models of fivefold twinned nanowires. (a) Side view with $\langle 110 \rangle$ axis orientation; (b) Cross-sectional views of three different types of nanowires, namely, cylindrical, pentagonal prismatic and rectangular cuboid nanowires. The tensile loadings are applied along $\pm x$ directions, as indicated by the two arrows. The atoms shown (in current and later figures of this section) in off-white, blue, and red are those in local fcc, hcp and icosahedral lattices; while disordered atoms in gold represent free surfaces or dislocation cores.(Jiang, Shen, et al. 2013) .....	44
Figure 3.7 (a) Stress-strain curve and (b) fraction of hcp atoms as a function of strain for a cylindrical nanowire under tension at a strain rate of $0.001\% \text{ ps}^{-1}$ . The insets are the	

snapshots of atomic configurations at different strain values. In the expanded scaled insets, surface atoms are not shown to facilitate visualizing the twins.(Jiang, Shen, et al. 2013) .....	47
Figure 3.8 Shape and composition of quasi-icosahedral structures formed in the fivefold nanowires. (a) Morphology from the cross-sectional view of the nanowires, with the comparison by a sketch of ideal icosahedron; (b) Spatial distributions of the fivefold twins in the quasi-icosahedral structures from different viewpoints. Only fcc, hcp and icosahedral atoms are shown for clarity. The TBs in panel (a) are marked by colored lines and green dots. The green dots indicate those TBs of the intrinsic fivefold axis that are perpendicular to the y-z plane.(Jiang, Shen, et al. 2013) .....	48
Figure 3.9 Atomic configurations of fivefold twinned (a) Ag and (b) Al nanowires under tension. The atoms shown in off-white, blue and light blue are those in local fcc, hcp and icosahedral lattices. Disordered and surface atoms are removed for clarity. ....	50
Figure 3.10 Generalized stacking fault energy (GSF) curve for Au, Ag, Cu and Al. ....	50
Figure 3.11 Decomposition of the general impact mode among discrete nanostructures, with the middle box on the two beams in transverse impact indicating the periodical boundary conditions to be used in molecular dynamics simulation. In the transverse impact mode, it can be further composed to a particle-beam model and a beam-beam model.....	54
Figure 3.12 Peak stress vs. particle velocity curves for the systems with aspect ratios 1:4 and 1:2, as well as the comparison with the experimental (Chau et al. 2010) and theoretical (Bringa et al. 2004) results for the transverse impact response of single-crystal Cu samples (Chen, Jiang, et al. 2012). .....	58
Figure 3.13 Peak stress vs. particle velocity curves for the systems with aspect ratios 1:4 and 1:2 for the transverse impact response of single-crystal Al samples. ....	59
Figure 3.14 Peak Time histories of the impact pressure and number fractions of target atoms in hcp crystal structures for the Cu systems with aspect ratios 1:4, 1:2, and 1:1, respectively.(Chen, Jiang, et al. 2012) .....	60
Figure 3.15 Stress distribution predicted by MPM simulations with different aspect ratios. ....	60
Figure 3.16 (a) and (b):Target deformation patterns with time. Aspect ratios are: (a) 1:4 and (b) 1:2. (c) and (d): Time histories of the principal stresses in the target. Aspect ratios are: (c) 1:4 and (d) 1:2.....	62
Figure 3.17 Atomic configurations at times 0.05, 0.15, 0.25, and 0.50 ps for (a) simulation 2, (b) simulation 8, and (c) simulation 10. Only the target atoms in the	

region between $0 - 10a$ along the x-direction are shown. The arrows and dashed vertical lines in panel (a) denote the direction and instantaneous position of the shock front.....	63
Figure 3.18 Time histories of (a) the impact pressure and (b) the number fraction of target atoms in the hcp crystal structure for the Cu systems with different size and aspect ratios (Chen, Jiang, et al. 2012). .....	64
Figure 3.19 Schematic diagram of the simulation model(Jiang et al. 2012, Jiang 2013). The geometry of the single crystal Cu nanobar (target) is characterized by the length $l_t$ and height $h$ , i.e., $l_t \times h \times h$ . Two additional regions with length $l_f$ located at either end of the target are treated as flyers. The flyers impact the ends of the target with speed 500 m/s, as indicated by the two red arrows. ....	66
Figure 3.20 Center-of-mass displacement for each layer along the shock direction as a function of time during shock propagation for the nanobars with (a) $10a \times 10a$ , (b) $20a \times 20a$ , and (c) $40a \times 40a$ cross sections. The insets in frames in (a) and (c) are expanded scales to more clearly illustrate the results at short post-impact times (Jiang et al. 2012, Jiang, Shen, et al. 2013, Jiang 2013). ....	71
Figure 3.21 Size Effect on the Deformation Pattern of Nanostructure. ....	72
Figure 4.1 The initial configuration of a representative Kr-Cu system at 298 K and 1 atm, which is used as the starting thermodynamic state for the hydrodynamic compression simulations discussed in connection with Figs. 4.2-4.6. ....	78
Figure 4.2 Pressure-density curves of periodical cubic Cu samples with different cell sizes. ....	79
Figure 4.3 Pressure-volume curves for both finite-size cubic and bulk (3-D periodic) Cu crystals. ....	79
Figure 4.4 Panels (a) and (b): Atomic configurations of the Kr-Cu system at 298 K and 5 GPa for an inclusion with edge length $10a$ . Pressure-loading rates are: (a) 10 MPa/ps and (b) 1 MPa/ps. Panels (c) and (d): As in panels (a) and (b), respectively, but with no inclusion present. ....	82
Figure 4.5. Panels (a) and (b): Atomic configurations of the Kr-Cu system at 298 K and 5 GPa for an inclusion with edge length $10a$ . Pressure-loading rates are: (a) 10 MPa/ps and (b) 1 MPa/ps. Panels (c) and (d): As in panels (a) and (b), respectively, but with no inclusion present. ....	83
Figure 4.6. Atomic configurations of the Kr-Cu system at 298 K and 5 GPa for a spherical inclusion of diameter $10a$ . Pressure-loading rates are: (a) 10 MPa/ps and (b) 1 MPa/ps. ....	85

Figure 4.7 Atomic configurations of the Kr-Cu system at 298 K and 5 GPa for cubic inclusions and pressure-loading rate 1 MPa/ps. Inclusion edge lengths are: (a) $5a$ , (b) $10a$ , and (c) $20a$ . .....	86
Figure 5.1 Schematic of a Cu target impacted by a Cu flyer simulated with (a) the DPD-only model and (b) the DPD/MPM-grid model. ....	90
Figure 5.2 Time histories of displacements of reference region 1 and region 2 in the Cu target, simulated using the DPD-only model (solid curve) and the coupled DPD/MPM-grid model with different MPM cell edge lengths (dashed, dot-dashed, and dotted curves). ....	91
Figure 5.3 Deformed configurations of the Cu target at 10 ps after impact, simulated with (a) the DPD-only model and the DPD/MPM-grid model for MPM cell edge lengths of (b) $2 \text{ \AA}$ and (c) $8 \text{ \AA}$ . ....	92
Figure 5.4 Schematic of a Cu rod subjected to tensile loading at both ends, with (a) the DPD-only model and (b) the DPD/MPM-grid model. ....	95
Figure 5.5 Stress-strain relations for the Cu rod under tensile loading at strain rate $0.02/\text{ps}$ , simulated using the DPD-only model (solid curve) and coupled DPD/MPM-grid model for different MPM cell edge lengths (dashed, dot-dashed, and dotted curves). ....	96
Figure 5.6 Linear fitting of stress-strain ( $\sigma$ - $\epsilon$ ) curve for the Cu rod under tension with DPD-only model. ....	97
Figure 5.7 Schematic of a Cu target impacted by a Cu flyer, simulated using the concurrent DPD/MPM model. The physical situation is the same as in depicted Fig. 5.1 (see Section 5.2.1) except that in the present case the right half of the target (and the flyer) consists of DPD particles and the left half consists of MPM particles. The MPM particles are displayed with an artificially increased diameter for clarity of visualization. ....	98
Figure 5.8 Configurations of the Cu rod subject to impact simulated with and without the interface treatment. The DPD/MPM interface is in the middle of the rod. ....	100
Figure 5.9 Displacement profiles at various times for the physical situation depicted in Fig. 5.6, simulated using the concurrent DPD/MPM model. The edge length of the MPM grid used is $4 \text{ \AA}$ . The interface between the DPD and MPM subdomains is initially located at $x \approx 9.35 \text{ nm}$ . ....	101
Figure 5.10 Schematic of the concurrent DPD/MPM simulation of a Cu rod under tension. The rod is divided into three regions: one DPD region in the middle as shown in green, two equivalent MPM regions symmetrically located at the two sides. ....	102

Figure 5.11 Deformation of the Cu rod under tension with DPD-only model, DPD/MPM models with and without interface treatment.....	103
Figure 5.12 Stress-strain relations for the Cu rod under tensile loading at strain rate of 0.0035/ps., simulated using the DPD-only model (solid curve) and concurrent DPD/MPM model for different MPM cell edge lengths (dashed, dot-dashed, and dotted curves).....	104
Figure 6.1 3-D configurations of the Cu inclusion in the fluid with the concurrent DPD/MPM model.....	110
Figure 6.2 Sketches of the particle/rod assemblies with different arrangements of the components.....	111
Figure 6.3 3-D configurations of a particle/rod assembly (Assembly 4 as an example) in the fluid with the concurrent DPD/MPM model.....	112
Figure 6.4 Pressure-volume curves for finite-size cubic (simulated by concurrent DPD/MPM model) and bulk (3-D periodic) Cu crystals (simulated by both MD and DPD simulations).....	113
Figure 6.5 Snapshots of the solid-state sintering of the particle-particle model at 1 GPa (Assembly 0).....	116
Figure 6.6 Configuration of the dumbbell-shaped particle-particle model after the solid-state sintering.....	117
Figure 6.7 Time history of the neck width of the particle-particle model with the concurrent DPD/MPM model at different pressure levels, compared by that obtained from MD and DPD simulations.....	118
Figure 6.8 Snapshots of the particle/rod assembly model (Assembly 1) at 1 GPa.....	119
Figure 6.9 Snapshots of the particle/rod assembly model (Assembly 2) at 1 GPa.....	120
Figure 6.10 Snapshots of the particle/rod assembly model (Assembly 5) at 1 GPa.....	120
Figure 6.11 Snapshots of the particle/rod assembly model (Assembly 3) at 1 GPa.....	122
Figure 6.12 Snapshots of the particle/rod assembly model (Assembly 6) at 1 GPa.....	122
Figure 6.13 Snapshots of the particle/rod assembly model (Assembly 4) at 0.01 GPa..	123
Figure 6.14 Snapshots of the particle/rod assembly model (Assembly 4) at 0.01 GPa..	123
Figure 6.15 Snapshots of the particle/rod assembly model (Assembly 4) at 1 GPa.....	126

Figure 6.16 Snapshots of the particle/rod assembly model (Assembly 7) at 1 GPa. .... 126

Figure 7.1 Stress profiles of a rod subject to a longitudinal force simulated with (a) DDMP and (b) MPM, respectively.  $L$  is the length and  $C$  is sound the speed in the rod. .... 137

Figure A1. A bar subject to a tensile force. The bar is divided equally into three parts with different numbers of particles per cell ( $N_{ppc}$ ). The maximum  $N_{ppc}$  part is in the middle of the bar where the mass of material particles are the smallest. .... 139

## LIST OF TABLES

Table	Page
Table 3.1. Young's Modulus (GPa) of Cu nanowires with the size of $40a \times 10a \times 10a$ under tension after various pre-torsions. (Jiang et al. 2010).....	36
Table 6.1 Comparison of the CPU time consumed for simulating a particle-particle solid-state sintering with different simulation methods .....	127

## LIST OF ABBREVIATIONS

CNA: Common Neighbor Analysis

DDMP: Dual Domain Material Point Method

DPD: Dissipative Particle Dynamics

EAM: Embedded-Atom Method

FDT: Fivefold Deformation Twins

FEM: Finite Element Method

FTNW: Five-fold Twinned Nanowires

MD: Molecular Dynamics

MEMS/NEMS: Microelectromechanical/Nanoelectromechanical Systems

MPM: Material Point Method

NPT: Isothermal-Isobaric

NVE: Isochoric-Isoenergetic

NVT: Isochoric-Isothermal ensemble

P-V: Pressure-Volume

SF: Stacking Fault

SFE: Stacking-Fault Energy

bcc: Body-Centered-Cubic

fcc: Face-Centered Cubic

hcp: Hexagonal-Close-Packed

A PARTICLE-BASED MULTI-SCALE SIMULATION PROCEDURE WITHIN THE  
MATERIAL POINT METHOD FRAMEWORK

Shan Jiang

Dr. Zhen Chen, Dissertation Supervisor

ABSTRACT

Recent studies of nano energetic composites and nanoelectromechanical systems (NEMS) have underscored the need for an effective multiscale procedure for simulating the responses of discrete nano and sub-micron structures and assemblies to various extreme loading conditions. In this dissertation, a particle-based multi-scale simulation procedure is proposed with a concurrent link between the Dissipative Particle Dynamics (DPD) method and the Material Point Method (MPM), and a hierarchical bridge from Molecular Dynamics (MD) to DPD. Particularly, a simple interfacial treatment is also introduced for concurrent DPD/MPM simulations based on the features of the DPD force expression and the MPM constitutive model. First, to gain a fundamental understanding of deformation mechanisms at the atomic-scale and provide baseline results for the multi-scale simulation, atomistic modelling and simulation of discrete metallic nanostructures under various loading conditions are performed with MD and analyzed using Common Neighbor Analysis (CNA). The loading conditions simulated include basic mechanical loading (tension/torsion/bending), impact loading (transverse and longitudinal impact), and hydrodynamic loading. The detailed deformation mechanisms and mechanical response of these nanostructures are investigated, and the formation of some special

nanostructures (such as single and multiple fivefold twins, and icosahedral structures) are observed. Then, the proposed multi-scale procedure is illustrated using similar simulations of the dynamic and impact responses of discrete metallic nano structures, as well as rod/particle assemblies in a hydrostatic fluid system. It is shown that the DPD forces can be effectively coarse-grained using the MPM background grid, and that the concurrent link between the MPM and DPD enables near-seamless integration of constitutive modeling at the continuum level with force-based modeling at the mesoparticle level. Finally, it is shown that the multi-scale simulation procedure proposed in this work requires much less computational time than the MD simulations to simulate a similar problem.

# CHAPTER 1. INTRODUCTION

## 1.1 Research Background

### 1.1.1 Multi-Scale Simulation

At the nanoscale, the size effect on the discrete structural responses to extreme loading conditions is a hot research topic of current interest due to the potential benefits in modern engineering applications such as devices of nano/micro-electromechanical system (MEMS/NEMS), and nanothermite composites (Lieber 2003, Rossi et al. 2007). Thus it is very important to investigate the mechanical properties, deformation mechanisms, and failure mode of these material/structures for future mechanical design and energetic material synthesis. However, the mechanical deformations and structure failure are inherently multi-scale phenomena in which the mechanical behavior of the material is governed by processes that occur on different length and time scales. As indicated in an extensive review article (Bazant and Chen 1997), the onset and evolution of structural failure are related to the size effects at different scales due to the different features of micro-, meso- and macro-structures such as molecular, grain, cluster, and macroscopic structures. The inelastic deformation can be described as a prompt stress-controlled process if the deformation can occur in a nearly point-wise manner such as dislocation motion. However, the evolution of inelastic deformation appears to be a diffusion process if the deformation involves a length scale and can only occur in an essentially random-walk (disordered) manner subject to geometric constraints.

Continuum methods are excellent in describing the large-scale field, but generally reflect an averaged response. Thus this class of methods cannot provide a complete description that involves a local state of structure at atomic-scale. From a continuum viewpoint, the stress state at any material point depends not only on the strain at that point but also the strain distribution around that point during the evolution of failure. Thus, a failure criterion must be formulated as a nonlocal function that involves a length scale (size effect). As shown by Chen (Chen 1996), a complete failure evolution process could be characterized by the nonlocal transition between discontinuities of different degrees, depending on the structural scale considered.

At micro-scale, the experiments with crystalline materials have demonstrated that sample dimensions would influence the material strength and crystal plasticity due to the geometric constraints (e.g. surface to volume ratios) (Uchic et al. 2004). Nix and Gao (Nix and Gao 1998) have predicted the indentation size effect for crystalline materials based on the concept of geometrically necessary dislocations. The depth-dependent hardness is also related to the indenter shape due to different levels of stress concentration involved. Hence, geometric constraints appear to play a key role in characterizing the size effects at different scales. However, there is a lack of understanding concerning the linkages between different size effects, as can be found from the open literature. Research efforts have been mainly focused on size effects at particular structural scales. To gain new insight into the physical problems at the small scales, atomistic simulations such as molecular dynamics (MD) and Monte-Carlo method are used. With the rapid increases in computer speed and the development of improved interatomic potentials, some problems at larger scales are being simulated directly by

atomistic simulations. While this can provide great details of the atomic-scale dynamics, the length and time scales that could be probed by atomistic methods are still very limited. Many results obtained by MD simulation still cannot be compared directly to those observed in experiments. Therefore, one possible approach that can be applied to solve multi-scale problems is to combine the atomistic or mesoscale simulations with continuum methods.

As one of the simulation methods at continuum level, the Material Point Method (MPM) (Sulsky, Chen, and Schreyer 1994) discretizes a continuum body into material points without rigid mesh connectivity, and thus this particle-based method appears to be attractive for combination with atomistic/mesoscale particle methods. Within the MPM framework, particular advances should be noticed that are relevant for multi-scale simulation: A multi-level refinement scheme has been designed for the Generalized Interpolation Material Point (GIMP) Method (Ma et al. 2005); a hierarchical approach has been proposed and demonstrated in which material points at the fine level in the MPM framework are coupled directly with the atoms in MD simulations (Lu et al. 2006); and a sequential procedure has been recently developed to formulate the EoS, based on MD results, for use in macroscopic MPM simulations (Liu, Wang, and Zhang 2013). However, each of the hierarchical/sequential or multi-level refinement approaches just mentioned requires a transition region between different spatial scales, which limits their usefulness for the study of physical situations where discrete nano/micro structures (for example, nano/micro rods and beams in energetic composites) interact with each other.

In our previous work, a preliminary particle-based multi-scale procedure has been proposed wherein Cluster Dynamics (McDowell, Leach, and Gall) is linked

hierarchically with MD for sub-micron scale domains and concurrently with the MPM for simulations on larger scales (Chen, Han, et al. 2012). The method was used to explore the longitudinal impact response between two metallic microrods with different nanostructures. However, the CD method (Chen et al. 2004) used in the previous work relies on certain assumptions that limit the range of applicability, and much work remains to generalize the method to more realistic situations. Our recent progress in formulating a better mesoparticle potential fitted from atomic-level potentials, which extends the application of Dissipative Particle Dynamics (DPD) (Gan et al. 2014) from fluid to solid, enables the possibility of realizing a particle-based coupling scheme by incorporating both DPD particles at the mesoscale and MPM particles at the continuum-scale for multi-scale simulations. The previous research discussed above stimulates the initial motivation of this work to incorporate the DPD method into the MPM framework, which finally forms a concurrent DPD/MPM model described in this dissertation.

### **1.1.2 The Material Point Method**

Many simulation cases that are related to practical engineering problems and material science includes localized large deformation, crack propagation, and fragment separation, for which the meshless (mesh-free) methods are uniquely suitable while the conventional mesh-based methods are less applicable. The key difference among the various spatial discretization numerical methods is the way quantities related to gradients and divergences are calculated. As compared with mesh-based method such as Finite Element Method (FEM) and Finite Difference Method (FDM), the meshless methods do not require rigid mesh connectivity, and the interpolation in the moving domain of influence is the common feature of different meshless methods.

The Material Point Method (MPM) (Sulsky, Chen, and Schreyer 1994) is a useful meshless computational tool for simulating multi-phase interactions in processes that involve failure evolution, such as impact, penetration, perforation, and blast-fragment interaction. The MPM is an extension to solid mechanics of the hydrodynamics method called FLIP which, in turn, evolved from the Particle-in-Cell Method. The essential idea of the MPM is to take advantage of the strengths of both the Eulerian and Lagrangian methods while avoiding the shortcomings of each. In comparison with the other meshless methods (Chen et al. 2002), the MPM is less complex and has a cost factor of at most twice that associated with the use of corresponding finite elements. In addition, it can be easily interfaced with Finite Element Method (FEM) codes due to the use of the same weak formulation for both methods.

The use of single-valued mapping functions in the MPM results in a nature no-slip contact/impact scheme without introducing master or slave nodes so that interpenetration is naturally avoided in multi-body interaction related problems. In the original MPM (Sulsky, Chen, and Schreyer 1994), however, there exists a cell-crossing issue due to the use of local mapping functions, and special caution must be taken to deal with a moving boundary condition. Much effort has been expended, especially over the past decade, to improve the original MPM through the use of nonlocal treatments (which increase the computational expense), as can be found in the representative references (Bardenhagen and Kober 2004, Sadeghirad, Brannon, and Burghardt 2011, Zhang, Ma, and Giguere 2011). Much research has also been done to apply the MPM to more engineering problems of practical interest (Chen et al. 2003, Guilkey and Weiss 2003, Zhou, Stormont, and Chen 1999), but it is still a challenging task to effectively discretize

different spatial scales in a single computational domain which involves multi-physical and multi-scale phenomena. In this dissertation, an effort has been made to develop a particle-based multi-scale simulation scheme within the MPM framework. The proposed numerical procedure as well as the framework of MPM will be outlined in Chapter 2.

## **1.2 Objective of Research**

The objectives of this doctoral study are aimed at two major areas:

On one hand, to gain the fundamental information at the atomic-level, MD simulations of various discrete nanostructures (nanoparticles, nanorods, nanobeams, and their assemblies) were performed. The study of the deformation mechanism and deformation pattern of the nanostructures under various extreme loading conditions, such as high strain rate and high speed impact loading are studied. Such research will be helpful for understanding the fundamental physics and obtaining baseline results with which to test the results from the proposed multi-scale simulation procedure.

On the other hand, a particle-based multi-scale procedure is proposed. The method consists of a hierarchical bridge from MD to DPD for nanoscale simulations and a concurrent link between DPD and the MPM for micro-scale simulations. Focusing on the link between DPD and the MPM, this work will first demonstrate that the dynamics of DPD particles can be coarse-grained using a straightforward adaptation of the standard MPM algorithm. Then it will be demonstrated that DPD and MPM subdomains in a single simulation domain can be treated concurrently and nearly seamlessly. Meanwhile, particular attention will be devoted to the development of an effective interfacial scheme for use in the concurrent simulations. Finally, the proposed methods will be used to

simulate discrete nanostructures under different loading conditions such as particle/rod assemblies embedded in a hydrostatic fluid.

### **1.3 Outline of Dissertation**

The remaining chapters of this study are arranged as follows:

The essential features of the governing equations for MD, DPD, and the MPM at different scales are first introduced in the first three sections of Chapter 2, to provide the foundation for the proposed particle-based multi-scale simulation procedure. Then, the proposed hierarchical and concurrent multi-scale solution schemes are described in the last section of Chapter 2.

To gain the fundamental understanding of the deformation mechanisms of the materials as well as the reference data to test the proposed multi-scale procedure, atomistic modeling and simulation are presented in Chapters 3 and 4. Research includes the mechanical behavior of nanowires subject to dynamic tension/bending/torsion loading conditions, transverse and longitudinal impact of the nanostructures, and solid particle inclusion in the fluid of initial gaseous state.

Corresponding to the atomistic simulations in Chapter 3, similar representative examples are used in Chapter 5 to illustrate the proposed multi-scale procedure. Test problems include tension and impact loading on the nanorods with both the simply coupled DPD/MPM- background- grid model and the concurrent multi-scale DPD/MPM model.

Corresponding to the atomistic simulations in Chapter 4, single nanostructure inclusions and rod/particle assemblies in fluid with the proposed multi-scale procedure

are simulated in Chapter 6. Different initial arrangements of the components are considered to investigate their effect on the coalescence patterns of the assemblies.

Finally, current research status and major findings of this work are summarized in Chapter 7. Future research tasks and recommendations are also given in this chapter.

## CHAPTER 2. GOVERNING EQUATIONS AND METHODOLOGY

Several computational simulation methods at different scales are introduced in this chapter, to provide the foundation for the proposed particle-based multi-scale simulation procedure. The essential features of the governing equations for MD, DPD, and the MPM are summarized in Sections 2.1, 2.2 and 2.3, respectively. The proposed hierarchical and concurrent multi-scale solution schemes are then described in Section 2.4.

### 2.1 Molecular Dynamics at the Atomic Scale

Molecular dynamics is a widely used tool for atomic simulations. The very early work about modern MD simulations of materials would go back to 1964 when Rahman (Rahman 1964) simulated 864 argon atoms using the Lennard-Jones potential. Since then, MD simulations have been used in many areas for simulating the properties of materials. In the past two decades, with the capability of using the massively parallel computers, large-scale atomistic simulations are able to provide the most detailed information for the study of complicated phenomena at the atomic scale.

Consider a system containing  $N$  particles. The classical equations of motion for this system can be written in various ways. One of the fundamental forms is the Lagrangian equation of motion,

$$\frac{d}{dt} \left( \frac{\partial L}{\partial \dot{q}_i} \right) - \left( \frac{\partial L}{\partial q_i} \right) = 0, \quad (2.1)$$

where the Lagrangian function  $L(\mathbf{q}, \dot{\mathbf{q}})$  is defined in terms of kinetic and potential energies

$$L = K - V. \quad (2.2)$$

With Cartesian coordinates  $\mathbf{r}_i$  and the common definitions of  $K$  and  $V$ , it can be shown that the dynamics of a conservative system consisting of  $N$  particles is governed by Newton's equation of motion for each particle  $i$ :

$$m_i \frac{d^2 \mathbf{r}_i}{dt^2} = m_i \mathbf{a}_i = -\frac{\partial}{\partial \mathbf{r}_i} U_{tot}(\mathbf{r}_1, \mathbf{r}_2, \dots, \mathbf{r}_N) \quad (2.3)$$

where  $m_i$ ,  $\mathbf{r}_i$ , and  $\mathbf{a}_i$  are the mass, position, and acceleration vectors of particle  $i$ , respectively, and  $U_{tot}$  is the total potential energy that depends only on the particle positions.

To solve the ordinary differential equations such as Eq. (2.3), a standard numerical method commonly used is the finite difference approach. Particularly, in MD simulations, the Gear predictor-corrector algorithm is usually employed (Allen and Tildesley 1989).

In addition, stress calculation in MD simulations has been a focus over the past two decades. The virial stress, derived from the virial theorem of Clausius (Clausius 1870) as a thermodynamics approach to the formulation of atomic-scale stress, is widely used to calculate the pressure of a system (Rowlinson and Widom 2002). A study by Cheung and Yip (Cheung and Yip 1991) showed that the virial stress is equivalent to the mechanical definition of stress for a homogeneous system, and that the equivalence can be demonstrated by using the concept of volume average if inhomogeneity happens.

## 2.2 Dissipative Particle Dynamics at the Mesoscale Level

Dissipative particle dynamics (DPD) is initially derived from MD, via coarse-graining the molecular details to capture the physics at mesoscale (Hoogerbrugge and Koelman 1992). It has been developed to simulate complex fluid flows involving colloidal suspension, polymer, phase separation, interface dynamics, membrane and two-phase flow at the mesoscopic scale. DPD is more computationally efficient than MD, and sufficient to capture the mesoscale details than conventional continuum-level simulation techniques. Hoogerbrugge and Koelman (Hoogerbrugge and Koelman 1992) first studied the creep flow through a square array of cylinders and demonstrated the capability of using DPD to simulate hydrodynamic phenomena, in which the fluid flow was limited to creep flow and the inertia effect could be neglected. Boek et al. (Boek et al. 1997) later computed the viscosity of fluid associated to suspended ball, pole and disk. With the modified DPD method proposed by Espanol and Warren (Espanol and Warren 1995), Boek and Schoot (Boek and Van Der Schoot 1998) further investigated the fluid flow through periodic cylinder array and obtained the dimensionless drag force, which demonstrated the applicability of DPD simulation at some limited Reynold numbers. After that, Chen et al, (Chen et al. 2006) and Kim and Philips (Kim and Phillips 2004) computed the fluid flow through a sphere/cylinder. Their simulation results have shown that it is possible to simulate hydrodynamic phenomena at low Reynold numbers, but that it might be inaccurate at high Reynold numbers because of the fluid compressibility.

To bridge the temporal and spatial gaps between nano and sub-micron scale simulations, the DPD with conserved energy (DPDE) method (Stoltz 2006, Lísal, Brennan, and Smith 2006) has been developed starting from the classical isothermal DPD

(Hoogerbrugge and Koelman 1992), in which the atomic-scale details are averaged and associated with effective coarse-grained particles. The extent of coarse graining, that is, the numbers of atoms subsumed by a single DPD particle, varies widely depending on the application. The DPDE governing equations for each coarse-grained particle  $i$  are written as follows:

$$m_i \frac{d^2 \mathbf{r}_i}{dt^2} = m_i \mathbf{a}_i = \mathbf{f}_i^C + \mathbf{f}_i^D + \mathbf{f}_i^R \quad (2.4)$$

$$\mathbf{f}_i^C = \sum_{i \neq j} -\nabla U(\mathbf{r}_{ij}) \mathbf{e}_{ij} \quad (2.5)$$

$$\mathbf{f}_i^D = \sum_{i \neq j} -\gamma_{ij} w^D(\mathbf{r}_{ij}) \mathbf{v}_{ij} \quad (2.6)$$

$$\mathbf{f}_i^R = \sum_{i \neq j} \sigma_{ij} w^R(\mathbf{r}_{ij}) dW_{ij} \mathbf{e}_i \quad (2.7)$$

where  $\mathbf{f}_i^C$ ,  $\mathbf{f}_i^D$  and  $\mathbf{f}_i^R$  represent, respectively, the conservative force, dissipative force, and random force vector acting on particle  $i$ . As before,  $m_i$ ,  $\mathbf{r}_i$ , and  $\mathbf{a}_i$  are, respectively, the mass, position, and acceleration vector of particle  $i$ , and  $U$  is the inter-particle potential. The quantities  $\gamma_{ij}$  and  $\sigma_{ij}$  are coefficients characterizing the strengths of the non-conservative forces,  $w^D$  and  $w^R$  are the weight functions of  $\mathbf{r}_{ij} = \mathbf{r}_i - \mathbf{r}_j$ ,  $\mathbf{v}_{ij} = \mathbf{v}_i - \mathbf{v}_j$  is the velocity difference vector between particles  $i$  and  $j$ , and  $W_{ij}$  is the independent  $d$ -dimensional Wiener processes. The quantity  $\mathbf{e}_i = \mathbf{r}_i / |\mathbf{r}_i|$  is the normalized position vector of particle  $i$  and  $\mathbf{e}_{ij} = \mathbf{r}_{ij} / |\mathbf{r}_{ij}|$  is the unit vector between particles  $i$  and  $j$ .

Particularly for the multi-scale DPD/MPM simulations in this dissertation, the material Cu is considered as a typical example, and our work is focused on an atomic solid (Cu) described using the interatomic potential energy function due to Sutton-Chen

potential (Sutton and Chen 1990). The parameters in the DPD force expression used here were calibrated by using a genetic algorithm to optimize the fit between the Sutton-Chen force field for Cu and an analogous coarse-grained form wherein one mesoparticle corresponds to eight copper atoms and the coarse-grained lattice parameter is twice that the value for atomic Cu in the MD model (Gan et al. 2014). The DPD parameter  $\gamma$  was set to 0.2 amu/ps and the fit was performed based on the 298 K isotherm.

### 2.3 Material Point Method at the Continuum Level

At the continuum scale, the governing differential equations under purely mechanical loading can be derived from the conservation equations for mass and momentum,

$$\frac{d\rho}{dt} + \rho \nabla \cdot \mathbf{v} = 0, \quad (2.8)$$

$$\rho \mathbf{a} = \nabla \cdot \mathbf{s} + \rho \mathbf{b}, \quad (2.9)$$

supplemented with a suitable constitutive equation to describe the internal interactions among material points and the kinematic relation between strain and displacement. In Eqs. (2.8) and (2.9),  $\rho(\mathbf{x}, t)$  is the mass density,  $\mathbf{v}(\mathbf{x}, t)$  is the velocity,  $\mathbf{a}(\mathbf{x}, t)$  is the acceleration,  $\mathbf{s}(\mathbf{x}, t)$  is the Cauchy stress, and  $\mathbf{b}(\mathbf{x}, t)$  is the specific body force due to, for example, gravity. The vector  $\mathbf{x}$  is the time-dependent position vector of the material points in the continuum. For given boundary conditions and initial data, the governing differential equations, if they are well-posed, can be solved either analytically or numerically. The key difference among different spatial discretization methods is how the gradient and divergence terms are calculated.

As a particle method, the MPM discretizes a continuum body in the original configuration into a finite set of  $N_p$  material points (particles) that are tracked throughout the deformation process. Let  $\mathbf{x}_p^t$  denote the position vector of material point  $p$  ( $p = 1, 2, \dots, N_p$ ) at time  $t$ . Each material point at time  $t$  has an associated mass  $M_p$ , density  $\rho_p^t$ , velocity  $\mathbf{v}_p^t$ , Cauchy stress  $\mathbf{s}_p^t$ , strain  $\mathbf{e}_p^t$ , and any other internal state variables required by the constitutive description. Thus, these material points provide a Lagrangian description of the continuum body. Because the mass for a given material point is independent of time, Eq. (2.8) is automatically satisfied. At each time step, information from the material points is mapped to a background computational mesh (grid). This mesh spans the computational domain, and the details of its specification are chosen for computational convenience. After information is mapped from the material points to the mesh nodes, the discrete formulation of Eq. (2.9) can be obtained on the mesh nodes.

The weak form of Eq. (2.9) can be found, based on the standard procedure used in the FEM, to be (Sulsky, Chen, and Schreyer 1994)

$$\int_{\Omega} \rho \mathbf{w} \cdot \mathbf{a} d\Omega = - \int_{\Omega} \rho \mathbf{s}^s : \nabla \mathbf{w} d\Omega + \int_{S^c} \rho \mathbf{c}^s \cdot \mathbf{w} dS + \int_{\Omega} \rho \mathbf{w} \cdot \mathbf{b} d\Omega, \quad (2.10)$$

where  $\mathbf{w}$  denotes the test function,  $\mathbf{s}^s$  specific stress,  $\Omega$  the current configuration of the continuum body, and  $S^c$  the part of the boundary subject to a prescribed traction. A boundary layer can be used to enforce the moving traction boundary condition given by the prescribed traction vector  $\mathbf{c}^s$ . Because the whole continuum body is described with the use of a finite set of material points, the mass density can be written as

$$\rho(\mathbf{x}, t) = \sum_{p=1}^{N_p} M_p \delta(\mathbf{x} - \mathbf{x}_p^t), \quad (2.11)$$

where  $\delta$  is the Dirac delta function with dimension of reciprocal volume. The substitution of Eq. (2.11) into Eq. (2.10) converts the integrals to the sums of quantities evaluated at the material points, namely

$$\begin{aligned} & \sum_{p=1}^{N_p} M_p \left[ \mathbf{w}(\mathbf{x}_p^t, t) \cdot \mathbf{a}(\mathbf{x}_p^t, t) \right] \\ &= \sum_{p=1}^{N_p} M_p \left[ -s^s(\mathbf{x}_p^t, t) : \nabla \mathbf{w}|_{\mathbf{x}_p^t} + \mathbf{w}(\mathbf{x}_p^t, t) \cdot \mathbf{c}^s(\mathbf{x}_p^t, t) h^{-l} + \mathbf{w}(\mathbf{x}_p^t, t) \cdot \mathbf{b}(\mathbf{x}_p^t, t) \right], \end{aligned} \quad (2.12)$$

where  $h$  is the thickness of the boundary layer. As can be seen from Eq. (2.12), the interactions among different material points are only present in the gradient terms, and a suitable set of material points must be chosen to represent the boundary layer. In the MPM, a background computational mesh is required to calculate the gradient terms. To do so, suppose that a computational mesh is constructed of 8-node cubic cells (for three-dimensional problems). These cells are used to define standard nodal basis functions,  $N_i(\mathbf{x})$ , associated with spatial nodes  $\mathbf{x}_i(t)$ ,  $i = 1, 2, \dots, N_n$ , where  $N_n$  is the total number of mesh nodes. The nodal basis functions are selected from conventional finite element shape functions. The spatial coordinates of any material point in a given cell at time  $t$  can then be represented by

$$\mathbf{x}_p^t = \sum_{i=1}^{N_n} \mathbf{x}_i^t N_i(\mathbf{x}_p^t), \quad (2.13)$$

where  $\mathbf{x}_i^t$  are the nodal coordinates. Similarly, the displacement vector of any material point in a cell is defined by the nodal displacements,  $\mathbf{u}_i^t(t)$ , as follows:

$$\mathbf{u}_p^t = \sum_{i=1}^{N_n} \mathbf{u}_i^t N_i(\mathbf{x}_p^t). \quad (2.14)$$

Because the same basis functions are used for both spatial coordinates and displacements, kinematic compatibility requires that the basis functions advect with the material, as in the updated Lagrangian framework; that is, the basis functions must be independent of time. It follows that the velocity and acceleration of any material point in a cell can be represented in the same way as that for the displacement in Eq. (2.14). The test function associated with any material point also has the same form,

$$\mathbf{w}_p^t = \sum_{i=1}^{N_n} \mathbf{w}_i^t N_i(\mathbf{x}_p^t), \quad (2.15)$$

where  $\mathbf{w}_i^t$  is the nodal test function. While the kinematic vectors, Eqs. (2.13)-(2.15), are continuous across the cell boundary, the gradients of these vectors are not – due to the use of linear shape functions for computational efficiency in the original MPM formulation (Sulsky, Chen, and Schreyer 1994) that is used here.

With the use of the above equations and the standard procedure as employed in the FEM, the discretized governing differential equations can be obtained as

$$m_i^t \mathbf{a}_i^t = (\mathbf{f}_i^t)^{int} + (\mathbf{f}_i^t)^{ext}, \quad (2.16)$$

for a lumped mass matrix; where the internal force vector is given by

$$(\mathbf{f}_i^t)^{int} = - \sum_{p=1}^{N_p} M_p \mathbf{s}_p^{s,t} \cdot \mathbf{G}_i(\mathbf{x}_p^t), \quad (2.17)$$

with  $\mathbf{s}_p^{s,t} = \mathbf{s}^s(\mathbf{x}_p^t, t)$  and  $\mathbf{G}_i(\mathbf{x}_p^t) = \nabla N_i|_{\mathbf{x}_p^t}$ ; and the external force vector takes the form

$$(\mathbf{f}_i^t)^{ext} = \mathbf{c}_i^t + \mathbf{b}_i^t, \quad (2.18)$$

where  $\mathbf{c}_i^f$  and  $\mathbf{b}_i^f$  denote, respectively, the specific traction and body force vectors evaluated at the grid nodes. Note that the internal force, which represents the interactions among material points and can be local or nonlocal depending on the stress-strain relation, is not continuous across the cell boundary due to the use of linear shape functions. However, the prescribed traction and body force vectors are continuous across the cell boundary, provided they are continuous before the spatial discretization is performed.

For large-scale simulations, an explicit time integrator is usually used to solve Eq. (2.16) for the nodal accelerations, with a time step that satisfies the stability condition, that is, the quotient of the smallest cell size to the wave speed. If a MPM cell includes multiple material points, the material properties are homogenized over the cell via the mapping and re-mapping scheme. During each time step, the information on each material point is mapped to the corresponding nodes of the cell in which the material point is located. After the equations of motion are solved on the cell nodes, the new nodal values of velocity are then used to update the positions of the material points via the mapping from the cell nodes to the related material points.

The strain increment for each material point is determined from the gradient of the nodal velocity evaluated at the material point position. The corresponding stress increment can then be found from the constitutive model. Internal state variables can also be assigned to the material points and transported along with them. Once the material points have been completely updated, if desired, the background grid can be discarded and a new grid defined for the next time step. Due to the use of the same set of nodal basis functions for both the mapping from material points to cell nodes and the re-

mapping from cell nodes to material points at each time step, the interpenetration between material bodies is precluded in the MPM. This enables simulations of impact and penetration problems without the need for a special contact algorithm.

## 2.4 A Particle-Based Multi-Scale Simulation Procedure

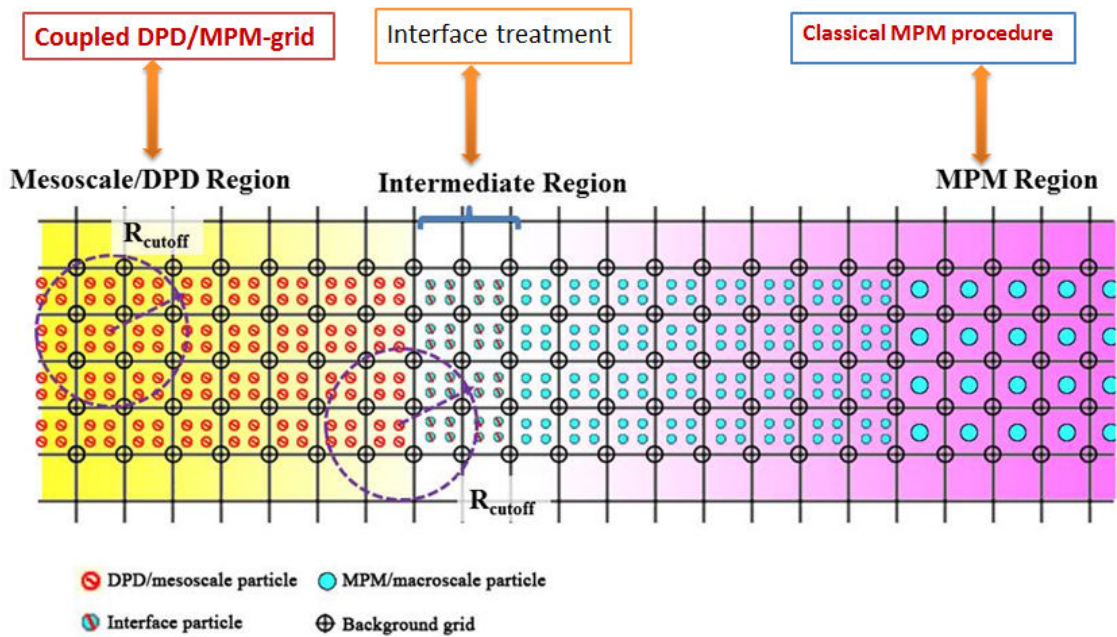


Figure 2.1 Schematic of the concurrent DPD/MPM modeling. If needed, the computational domain can be divided into several regions with different types of particles, namely, mesoscale/DPD region, classical MPM region, and intermediate region.

From Sections 2.1-2.3, it can be seen that Equations (2.3), (2.4), and (2.16) have similar forms although they are formulated at different scales and with different domains of influence. The right-hand sides of these equations – the force expressions, which are different for different materials – include the internal interactions among discrete particles (atoms, DPD particles, or material points) as well as the external forces. The

difference between the MPM and DPD or MD is that Eq. (2.16) is evaluated at the background grid nodes rather than at the material points. As a result, the strain and stress fields in the MPM can be easily determined using the gradient of nodal basis functions and the constitutive model, respectively, instead of defining a representative domain (a cutoff radius) to determine the strain and stress as required in DPD and MD.

In this dissertation, the proposed multi-scale simulation procedure consists of a concurrent link between the DPD and MPM particles to simulate microscale responses and a hierarchical bridge from MD to DPD for nano and sub-micron scale simulations (in which the DPD force expression is determined by fitting to MD results).

A schematic of the concurrent DPD/MPM modeling is shown in Fig. 2.1. As can be seen, the computational domain are divided into two major parts, namely, a DPD (mesoscale particle) region and a classical MPM (material point at the continuum-level) region. If it is need, an intermediate region will be introduced in the interface region between the DPD and MPM parts for a single material/structure. In the concurrent DPD and MPM computational domain, a particle is a DPD one if its force is defined by Eq. (2.4), which involves a cutoff distance. A particle is a material point if a constitutive model at the continuum level is used to calculate the internal force vector as shown in Eq. (2.17). Within the MPM framework, the DPD cutoff distance should be larger than the cubic cell edge length (for three-dimensional problems).

Within the framework of MPM, a single MPM cell can include both DPD and MPM particles at a given time such that the mapping and re-mapping procedure in the MPM algorithm yields a computational homogenization scheme over the cell domain. It will be shown in Chapter 5 that the DPD details can be effectively averaged through the

use of a coarse MPM background grid. Also in Chapters 5 and 6, it will show that the concurrent link between the MPM and DPD enables a nearly seamless integration of constitutive modeling at the continuum level with discrete DPD particle-based forces. The simplicity of the proposed particle-based simulation procedure provides a possible robust way for zoom-in to near-atomic-scale details and zoom-out to microscale responses.

The remaining section of this chapter describes the specific solution steps required for a concurrent MPM and DPD simulation. Equations shown hereafter in this section will be renumbered starting from Eq. (s-1) to describe the scheme of the concurrent multi-scale simulations in a clearer way.

#### **2.4.1 Initialization and Computational Set-Up**

The followings steps are performed prior to the first time step:

1. A continuum body (with single or multiple material phases) is discretized into a finite set of material points determined with respect to the original configuration of the body. Each material point carries its original material properties. The material points are followed throughout the deformation process of the body.
2. An arbitrary background grid with appropriate spatial resolution is defined and used to find the natural coordinates of any material point and to identify the grid cell that contains the material point.
3. All state variables at the material points are initialized, control parameters for the computer code are specified, and the system of DPD particles and/or material points is equilibrated to minimize the stress of the initial system.

### 2.4.2 Scheme of the Concurrent DPD/MPM Simulation

The following detailed steps are performed at each time step increment:

1. For each material point (both DPD and MPM particles), perform the mapping operation from the material point to the cell nodes enclosing the material point.

Map the mass from the material points to the nodes of the cell containing these points,

$$m_i^t = \sum_{p=1}^{N_p} M_p N_i(\mathbf{x}_p^t), \quad (\text{s-1})$$

where  $m_i^t$  is the mass at node  $i$  at time  $t$ ,  $M_p$  is the material point mass,  $N_i$  is the shape function associated with node  $i$ , and  $\mathbf{x}_p^t$  is the location of the material point at  $t$ .

Analogously, for each material point, map the momentum from the material point to the nodes of the cell enclosing the material point,

$$(\mathbf{mv})_i^t = \sum_{p=1}^{N_p} (\mathbf{Mv})_p^t N_i(\mathbf{x}_p^t), \quad (\text{s-2})$$

where  $(\mathbf{mv})_i^t$  denotes the nodal momentum at node  $i$  at time  $t$ , and  $(\mathbf{Mv})_p^t$  is the material point momentum at that same time. Find the internal force vector at the cell nodes for the MPM particles associated with that cell,

$$(\mathbf{f}_i^t)^{int} = - \sum_{p=1}^{N_p} \mathbf{G}_i(\mathbf{x}_p^t) \cdot \mathbf{s}_p^t \frac{M_p}{\rho_p^t}, \quad (\text{s-3a})$$

where  $\mathbf{G}_i(\mathbf{x}_p^t)$  is the gradient of the shape function associated with node  $i$  evaluated at  $\mathbf{x}_p^t$ . The quantities  $\mathbf{s}_p^t$  and  $\rho_p^t$  are, respectively, the particle stress tensor and the

particle mass density at time  $t$ . For the DPD particles associated with that cell, Eq. (s-3a) is replaced with the following expression:

$$\left(\mathbf{f}_i^t\right)^{int} = \sum_{p=1}^{N_p} \left(\mathbf{f}_{pj}^C + \mathbf{f}_{pj}^D + \mathbf{f}_{pj}^R\right) N_i\left(\mathbf{x}_p^t\right), \quad (\text{s-3b})$$

where  $\mathbf{f}_{pj}^C$ ,  $\mathbf{f}_{pj}^D$ , and  $\mathbf{f}_{pj}^R$  represent, respectively, the conservative force, dissipative force, and random force vector on particle  $p$  due to particle  $j$  ( $j=1,2,\dots,N_p^j$ , where  $N_p^j$  is the number of DPD particles within the cutoff radius of particle  $p$ ).

2. Apply essential and natural boundary conditions to the cell nodes, and compute the nodal force vector,

$$\mathbf{f}_i^t = \left(\mathbf{f}_i^t\right)^{int} + \left(\mathbf{f}_i^t\right)^{ext}, \quad (\text{s-4})$$

where  $\left(\mathbf{f}_i^t\right)^{ext}$  denotes the external nodal force vector as defined in Eq. (12).

3. Update the momenta at the cell nodes:

$$\left(m\mathbf{v}\right)_i^{t+\Delta t} = \left(m\mathbf{v}\right)_i^t + \mathbf{f}_i^t \Delta t. \quad (\text{s-5})$$

4. For each material point, perform the mapping operation from the nodes of the cell containing the material point to that point.

Map the nodal accelerations back to the material point:

$$\mathbf{a}_p^t = \sum_{i=1}^{N_n} \frac{\mathbf{f}_i^t}{m_i^t} N_i\left(\mathbf{x}_p^t\right). \quad (\text{s-6})$$

Map the current nodal velocities back to the material point to get the velocity  $\bar{\mathbf{v}}_p^{t+\Delta t}$  of the particle at the current time step:

$$\bar{\mathbf{v}}_p^{t+\Delta t} = \sum_{i=1}^{N_n} \frac{\left(m\mathbf{v}\right)_i^{t+\Delta t}}{m_i^t} N_i\left(\mathbf{x}_p^t\right). \quad (\text{s-7})$$

Compute the current material point position:

$$\mathbf{x}_p^{t+\Delta t} = \mathbf{x}_p^t + \bar{\mathbf{v}}_p^{t+\Delta t} \Delta t, \quad (\text{s-8})$$

which represents a backward integration.

Compute the material point displacement:

$$\mathbf{u}_p^{t+\Delta t} = \mathbf{x}_p^{t+\Delta t} - \mathbf{x}_p^0. \quad (\text{s-9})$$

As can be seen from Eqs. (s-7) and (s-8), nodal shape functions are used to map the nodal velocity continuously to the interior of the grid cell so that the positions of the material points are updated by moving them in a single-valued, continuous velocity field. Because the velocity  $\bar{\mathbf{v}}_p^{t+\Delta t}$  is used to update the material point position, the potential numerical error accumulated by the mapping operations is eliminated, such that the interpenetration between material bodies is precluded. This unique feature of the MPM enables simulations of impact and penetration problems without the need for a special contact algorithm.

5. Map the updated material point momenta back to the nodes of the cells containing these material points:

$$(m\mathbf{v})_i^{t+\Delta t} = \sum_{p=l}^{N_p} (M\mathbf{v})_p^{t+\Delta t} N_i(\mathbf{x}_p^t). \quad (\text{s-10})$$

6. Find the updated nodal velocities:

$$\mathbf{v}_i^{t+\Delta t} = \frac{(m\mathbf{v})_i^{t+\Delta t}}{m_i^t}. \quad (\text{s-11})$$

7. Apply the essential boundary conditions to the nodes of the cells containing the boundary points. For the essential boundary conditions, this treatment is consistent with

the weak form of the governing equations because the test functions  $w_i^t$  are assumed to be zero on the essential boundary.

8. If needed for the constitutive model of a MPM particle, find the current gradient of particle velocity,

$$\mathbf{L}_p^{t+\Delta t} = \sum_{i=1}^{N_n} \mathbf{v}_i^{t+\Delta t} \mathbf{G}_i(\mathbf{x}_p^t), \quad (\text{s-12})$$

and the particle strain increment,

$$\Delta \mathbf{e}_p = (\text{sym} \mathbf{L}_p^{t+\Delta t}) \Delta t, \quad (\text{s-13})$$

so that the stress increment can be obtained from the constitutive model for the given strain increment to update the stress tensor of the MPM particle:

$$\mathbf{s}_p^{t+\Delta t} = \mathbf{s}_p^t + \Delta \mathbf{s}. \quad (\text{s-14})$$

9. Identify which grid cell each material point belongs to, and update the natural coordinates of the material point. This is the convective phase for the next time increment.

10. Repeat steps 1-9 until the time has advanced to the desired value.

The procedures associated with Eqs. (s-1)-(s-14) should apply equally to DPD and MPM particles, simulated within the MPM framework.

As can be seen from Eqs. (s-6), (s-7), and (s-11), the simulation process will fail if  $m_i^t$  is close to zero, which happens when material points are close to the cell boundary.

Various nonlocal mapping procedures have been developed over the past decade to avoid the cell-crossing error in the original MPM (Bardenhagen and Kober 2004, Sadeghirad, Brannon, and Burghardt 2011, Zhang, Ma, and Giguere 2011). However, incorporating these improvements into the proposed multi-scale simulation procedure will incur

considerable computational expense and is beyond the scope of the current work. Instead, a simple measure is taken here to circumvent the cell-crossing issue within the original MPM framework: If  $m_i^t$  is less than a small number set by machine precision, the solutions from the equations in which  $m_i^t$  appears in the denominator are not used to update the variables associated with those equations at that time step.

### 2.4.3 Interface Treatment between the DPD and MPM Regions

In this sub-section, an interfacial treatment for the DPD/MPM model is proposed to capture the essential physics by smoothing the difference in force calculations for DPD and MPM particles. For simplicity in this dissertation, the case is considered where the DPD and MPM particles are of the same size for the same material. The internal force due to the DPD and MPM particles in the interfacial region is calculated using the following equation:

$$\left(\mathbf{f}_i^t\right)^{int} = \sum_{p=1}^{N_p^d} \left(\mathbf{f}_{pj}^C + \mathbf{f}_{pj}^D + \mathbf{f}_{pj}^R\right) N_i\left(\mathbf{x}_p^t\right) - \sum_{p=N_p^d+1}^{N_p^d+N_p^m} \mathbf{G}_i\left(\mathbf{x}_p^t\right) \cdot \mathbf{s}_p^t \frac{M_p}{\rho_p^t}, \quad (\text{s-15})$$

where  $N_p^d$  and  $N_p^m$  are, respectively, the number of DPD and MPM particles within the interfacial region. For each DPD particle in the interfacial region,  $\mathbf{f}_{pj}^C$ ,  $\mathbf{f}_{pj}^D$ , and  $\mathbf{f}_{pj}^R$  in the first term of Eq. (13) are determined as follows:

$$\mathbf{f}_{pj}^C = \sum_{k=1, k \neq j}^{N_p^j} -\nabla U\left(\mathbf{r}_{jk}\right) \mathbf{e}_{jk} \quad (\text{s-16})$$

$$\mathbf{f}_{pj}^D = \sum_{k=1, k \neq j}^{N_p^j} -\gamma_{jk} W^D\left(\mathbf{r}_{jk}\right) \mathbf{v}_{jk} \quad (\text{s-17})$$

$$\mathbf{f}_{pj}^R = \sum_{k=1, k \neq j}^{N_p^j} \sigma_{jk} w^R(r_{jk}) dW_{jk} \mathbf{e}_j, \quad (\text{s-18})$$

where  $N_p^j$  is the total number of the particles within the cutoff radius of DPD particle  $p$ . In combination with Eq. (s-15), Eqs. (s-3a) and (s-3b) are used to find the internal forces due to the MPM and DPD particles respectively, outside the interfacial region. From Eqs. (s-16) to (s-18), it can be seen that each DPD particle inside the interfacial region is subject to interactions with the MPM particles within its cutoff radius. Similarly, because Eq. (s-14) includes the internal force contributions from both DPD and MPM particles located within the interfacial region, each interfacial MPM particle is also connected with its neighbor DPD particles via the mapping and re-mapping process within the MPM framework.

With the use of the proposed interface treatment between the DPD and MPM region, the concurrent link between the MPM and DPD enables the near-seamless integration of constitutive modeling at the continuum level with force-based modeling at the mesoparticle level. It will be shown in Chapter 5 that by using the concurrent DPD/MPM model with the interface treatment, a single nanostructure can act as a complete whole, with predicted mechanical properties and deformation patterns similar to those obtained using DPD-only models.

## 2.5 Summary

In this chapter, the essential features of the governing equations for MD, DPD, and the MPM at different scales are summarized, to provide firstly the theoretical preparations for the multi-scale simulation. Then, a particle-based multi-scale simulation procedure is described that includes a hierarchical bridge from MD to DPD and a

concurrent link between DPD and the MPM. Finally, a simple interfacial treatment to deal with the mechanical response of a single material/structure has been proposed for concurrent DPD/MPM simulations based on the features the DPD force expression and the MPM constitutive model.

Because the method has not been applied previously to DPD particles, it is necessary to determine whether (or under what conditions) the “coarse grained DPD” that results from using the MPM mapping/remapping algorithm will reproduce the results obtained using standard, energy-conserving DPD (i.e., DPDE, Eqs. (2.4)-(2.7)). This intermediate description, which is referred to as the *DPD/MPM-grid* model, is tested later in this dissertation in Section 5.2.1 for the case of a Cu nanorod flyer impacting a Cu nanorod target, and in Section 5.2.2 for symmetric tensile extension of a Cu nanorod. Specifically, results obtained using DPDE (hereafter, the *DPD-only* model) will be compared to those obtained using the *DPD/MPM-grid* model for several choices of MPM background grid resolution. These *DPD/MPM-grid* model calculations are a necessary validation step on the path to the fully concurrent *DPD/MPM* framework, which is referred to as the *DPD/MPM* model. The overall capability of the proposed multi-scale simulation procedure will be demonstrated by simulating the dynamic and impact responses of discrete nano structures with various shapes and compositions, as will be shown in Chapter 5 and Chapter 6.

# CHAPTER 3. ATOMISTIC MODELING AND SIMULATION OF METALLIC NANOSTRUCTURES UNDER DYNAMIC AND IMPACT LOADING

## 3.1 Introductory Remarks

To gain the basic physics and new insights into multi-scale phenomena, atomistic simulation of structures/materials at nanoscale plays a significant role in scientific research with the ability to investigate atomic-scale dynamics in great detail (Gan, Shi, and Jiang 2012, Gan and Jiang 2013, Jiang, Zhang, et al. 2013). As one of the most important nanostructures, nanowires can provide ideal objects for people to study the unique electrical, optical and mechanical properties at nanoscale, which can serve as the fundamental parts for solving multi-scale problems. In 2001, scientists assembled molecules into basic circuits, raising hopes for a new world of nanoelectronics, which was listed as a breakthrough of that year by *Science* (Service 2001) due to the outstanding achievement in the field of low-dimension nanomaterials. As D. Appell describing in an editorial in *Nature* (Appell 2002): “nanowires, nanorods or nanowhiskers, it doesn’t matter what you call them, they’re the hottest property in nanotechnology.”

During the past decade, these nanowires with various shapes and geometries have been extensively studied because of the outstanding physical-mechanical properties (Lieber 2003, Seryogin et al. 2005), such as high melting point, high hardness and wide band gap (Verheijen et al. 2006). For instance, solid metal nanowires exhibit extremely

high strengths up to 100 times that of bulk materials (Wu, Heidelberg, and Boland 2005) and tubular  $\text{Fe}_3\text{O}_4$  nanowires have been measured to have a magneto-resistance of  $\sim 1\%$  at the temperature of 77 K when a magnetic field of 0.7 T is applied (Liu et al. 2005). It was found that hollow  $\text{Co}_3\text{O}_4$  nanowires can be used as components in lithium-ion batteries, chemical sensing, field-emission and electro-chromic devices (Li, Tan, and Wu 2006). Tubular gold and silver nanowires can serve as channels for protein transport (Yu, Lee, and Martin 2003) and nano-sized electrodes (Qu et al. 2004), respectively. They are regarded as the most promising building blocks for various nanodevices, including acoustic transducers and sensors (Chang et al. 2004), optoelectronics components (Seryogin et al. 2005) and logic gates (Verheijen et al. 2006).

Among various kinds of nanowires, metallic nanowires have attracted great interests as key building blocks of both electronic and electromechanical devices, i.e. as nanoscale interconnects and ultra-thin nanobridges (Agrait, Yeyati, and Van Ruitenbeek 2003). The interests in these one-dimensional metallic nanostructures are mostly driven by their superior physical properties in contrast to their bulk counterparts (Agrait, Yeyati, and Van Ruitenbeek 2003, Wu, Heidelberg, and Boland 2005). These low-dimensional nanostructures have a large aspect ratio of surface area to volume, and interact with each other mostly through their surfaces. Thus, their superior properties and the functionalities of nanowire-based devices may be strongly altered by changing their shapes (Li and Wang 2003). Therefore, prior to any feasible applications as well as possible incorporation in multi-scale modeling and simulation, the mechanical characteristics of individual nanowires under external loads (Tan et al. 2007, Zheng et al. 2008) need to be well evaluated.

Meanwhile, metal and metal-oxide nanorods/nanowires are also playing an important role in making nanothermite as an alternative energy source. In the past few years, nanocomposites of ordered porous iron oxidizer and Al nanoparticles (Mehendale et al. 2006), and self-assembled nanothermite comprising CuO nanorods and Al particles (Apperson et al. 2007) have been produced, which attracted an increasing attention. The fast energy generation of nanothermite, which involves severe chemical and physical exchanging processes, is affected significantly by the impact velocity and the ways of mixing the nanoparticle-based nanothermite with nanorod-based catalyst (Apperson et al. 2007). Bending and twisting behaviors of nanowires induced by the interactions with the fast-moving nanoparticles might be ubiquitous during the deformation process. Therefore, a better understanding of the interaction between nanoparticles and nanorods, as well as the impact response of the nanorods is important for the study of nanothermite properties. Since the real-time monitoring for extremely high loading rate is limited with the current experimental technique, it is difficult to describe the dynamic deformation process in detail. Under this circumstance, atomistic simulation provides an alternative approach to study the mechanical behavior of these nanostructures.

In this chapter, atomistic models of metallic nanowires/nanorod/nanobeam and nanoparticles are constructed to investigate the mechanical properties of these nanostructures under various extreme loading conditions, including both basic external mechanical loading (tension/torsion/bending) and high-speed impact loading. By means of MD simulations and atomic local structure identification, the deformation processes of the nanowires subject to these loading conditions are studied in detail. Meanwhile, the formation of defects and some special nanostructures during deformation processes are

also examined. Because the novel structure successfully produced in the experiments (Kim et al. 2008, Wu et al. 2006), the nanowires with five-fold twinning structures are also considered in the MD simulations, which shows a different deformation pattern than that from those with a single crystal structure. Based on these studies, a fundamental understanding of deformation mechanism at atomic-scale will be provided, and the mechanical properties of these materials obtained from the atomistic simulation will be considered as references for the multi-scale simulations.

### **3.2 Mechanical Response of Nanowires under Dynamic Loading**

To explore the mechanical response as well as the basic parameters of material properties of metallic nanowires, many studies have been conducted in the past two decades, with the consideration of the size, loading rate and thermal effects. The first goal is to evaluate the strength and understand the deformation mechanism of these nanostructures subject to four basic mechanical loading conditions, namely, tension (Ohnishi, Kondo, and Takayanagi 1998, Ikeda et al. 1999, Kondo and Takayanagi 2000, Koh et al. 2005, Park and Zimmerman 2005), compression (Lee, Lee, and Cho 2010, Lin and Pen 2007), bending (McDowell, Leach, and Gall 2008, Zheng et al. 2008, Zheng et al. 2009) and torsion (Kang and Hwang 2001, Jiang et al. 2009). In particular, strain rate induced amorphization in nickel and NiCu nanowires under tension was reported by Ikeda et al (Ikeda et al. 1999). Yielding and fracture mechanisms of metallic nanowires have been investigated at various strain rates, wire sizes and temperatures (Ikeda et al. 1999, Koh et al. 2005, Liang and Zhou 2005, Kang and Hwang 2001).

Although these basic loading cases have been investigated in the previous work, the mechanical responses such as deformation details of these nanowires under more

general loading conditions are still not well-understood. Since the potential metallic nanowire-based devices might work under more complicated conditions, and certain factors of the working environment such as thermal effect may have much influence on their functions, it is necessary to study the mechanical behavior of nanowires under various loading paths at different temperatures. Meanwhile, some special deformation patterns of these nanostructures formed during loading process need to be studied for better understanding the formation mechanism under different conditions (Zheng et al. 2009, Zheng et al. 2008, Jiang et al. 2010). In the remainder of this section, our studies of these nanowires subject to more complicated cases of combined tension-torsion loads will be briefly discussed in Section 3.2.1. Then, the deformation mechanism and the formation of some special nanostructures will be shown and studied in Section 3.2.2.

### **3.2.1 Tension/Torsion and Loading Path Effect**

As shown in Fig. 3.1, MD simulations were conducted to study the mechanical response of single crystalline Cu nanowires under different loading conditions of pre-tensile torsion and pre-torsional tension. Square cross-section copper nanowires were created with the initial crystallographic orientations, [100], [010] and [001], which coincided with the global x, y and z axes, respectively. The dimensions of the nanowire are indicated by  $l$  and  $l_c$ , as shown in Fig.3.1. The length of nanowire  $l = 40a$ , and the values of  $l_c$  can be set to  $5a$ ,  $10a$ ,  $15a$ , respectively, where  $a = 0.3615$  nm is the lattice constant of bulk face-centered-cubic (fcc) crystal copper.

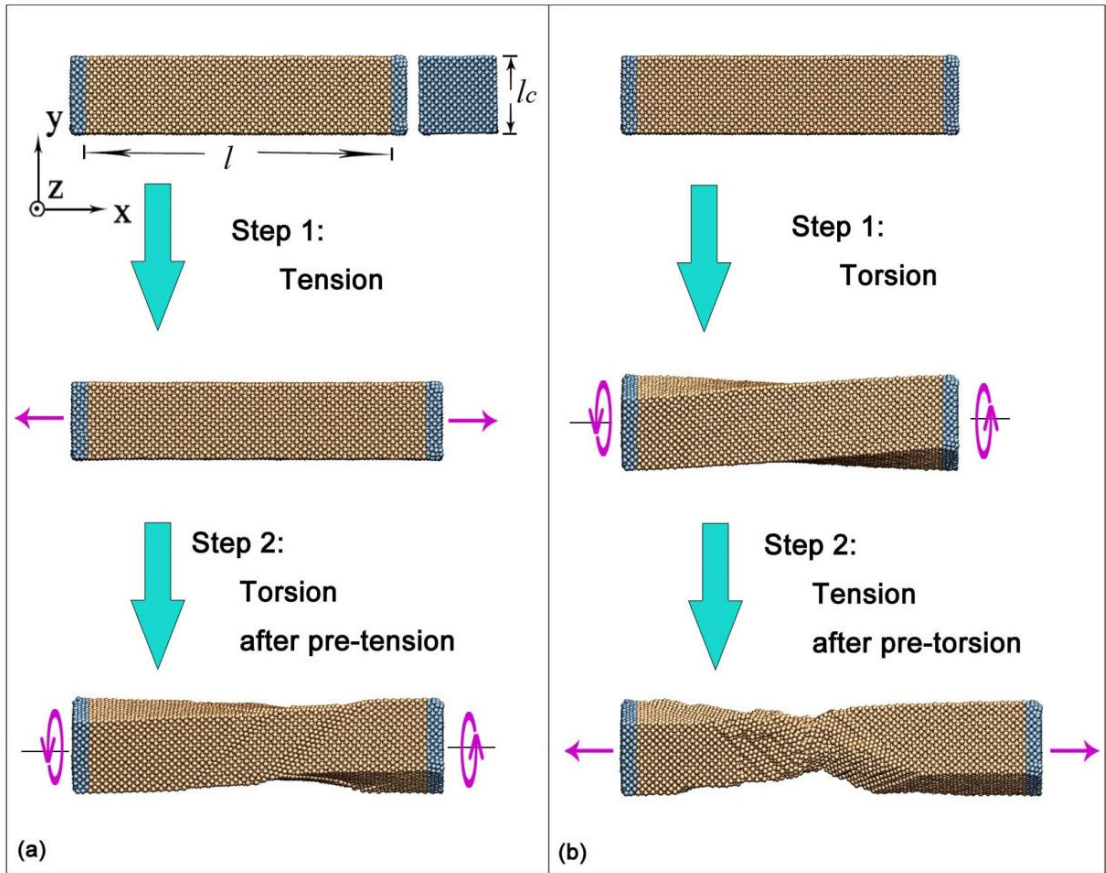


Figure 3.1 Sketch and different loading procedures of (a) pre-tensile torsion and (b) pre-torsional tension on a square cross-section nanowire. The geometry of the wire is characterized by the length  $l$  and cross-sectional length  $l_c$ . (Jiang et al. 2010)

To describe the interatomic interactions between copper atoms, the embedded-atom method (EAM) (Daw and Baskes 1984) developed by Mishin et al (Mishin et al. 2001) was adopted for material Cu. The MD simulations were conducted in the constant isochoric-isothermal (NVT) ensemble with velocity-Verlet integrator (Plimpton 1995). First, the wires were thermally equilibrated at a specified temperature to obtain an initial equilibrium configuration. During the whole relaxation and loading processes, non-periodic boundary condition was used and the time step was 2 fs, while the temperature

was controlled using a Nosé-Hoover thermostat (Nosé 1984, Hoover 1985). To investigate the thermal effect, different values of temperature from 10K to 400K were set. The stresses were calculated using the Virial theorem (Clausius 1870, Rowlinson and Widom 2002).

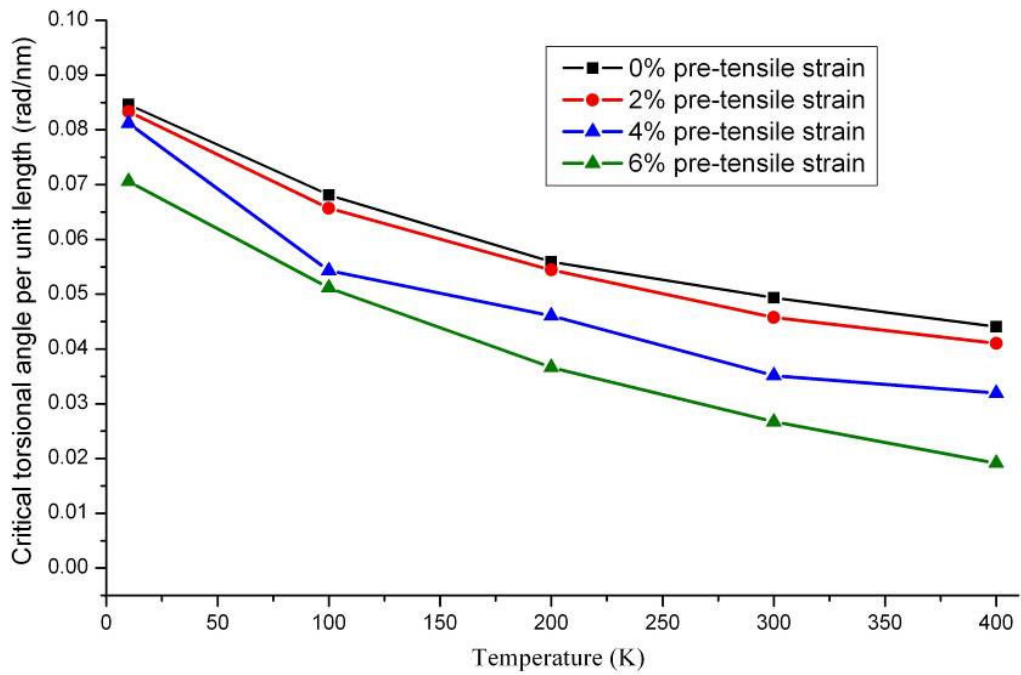


Figure 3.2 Critical angle pre unit length as a function of temperature for the nanowire with the size of  $40a \times 10a \times 10a$  under different pre-tensile strain at 300K. (Jiang et al. 2010)

In the case of pre-tensile torsion, a pair of tensile loads was first applied to the two boundaries of the wire. The tensile strains were set to 0%, 2%, 4% and 6%, respectively. After a certain strain was achieved, a pair of torsional loads was applied to the two end of wire instead of the previous tensile loads, as can be seen in Fig. 3.1(a). Similarly, in pre-torsional tension [see in Fig. 3.1(b)], the pre-torsional angle were set to

0, 0.2, 0.4 and 0.6 rad, respectively, after the torsional loads were applied. Then, torsional loads were removed and tensile load begins. It should be noted that the case of 0 rad pre-torsional tension referred to uniaxial tension. In all simulations, the tensile strain rate was set to  $0.1\% \text{ ps}^{-1}$  and torsional loading rate was  $6.92 \times 10^7 \text{ rad}\cdot\text{s}^{-1}\cdot\text{nm}^{-1}$ .

For the pre-tensile torsion, coupled effects of pre-tensile strain and temperature are shown in Fig. 3.2. Generally, the critical torsional angle per unit length  $\theta_{cpl}$  decreases with the increase of pre-tensile strain and temperature. In most loading cases, the decrease of  $\theta_{cpl}$  induced by thermal effect is more evident when the temperature changes at a lower level. As the temperature is elevated to a higher level, thermal effect induced decrement of  $\theta_{cpl}$  becomes smaller. In the case of large pre-tensile strain, such as 6% pre-strain, decrement of  $\theta_{cpl}$  is very large but the decrement value changes little as the temperature increases. Thermal effect can lead to more obvious weakness of stiffness when the pre-tensile strain increases to a certain level. At larger pre-strain and higher temperature, coupled effects of weakening in the lattice structure and large atomic vibrations speed the transformation from elasticity to plasticity.

For the cases of pre-torsional tension, tensile strengths of the nanowires under different levels of pre-torsional angle of nanowires at different temperatures are shown in Fig. 3.3. The results reflect the coupled loading path and thermal effect on the mechanical properties of nanowires. It can be found that values of yield stress decrease with the increase of temperature in all the pre-torsional loading paths. When the pre-torsional angle is lower than 0.6 rad, yield stress drops quickly with the temperature variation range from 10 K to 200 K. As the temperature increases further, the decrease of yield stress continues but changes in a much smaller degree, which indicates that the thermal

effect becomes less evident at higher level of temperature. However, in the case of 0.6 rad pre-torsion from 200 K to 300 K, the yield stress as a function of temperature shows that the trend of yield stress remains in a high rate of decreasing, which indicates that stretching response after larger pre-torsional angle can reinforce the temperature effect on weakening the strength of nanowires.

Table 3.1. Young's Modulus (GPa) of Cu nanowires with the size of 40a×10a×10a under tension after various pre-torsions. (Jiang et al. 2010)

Loading case	10 K	300 K
0 rad pre-torsion	100.9	85.11
0.2 rad pre-torsion	100.3	81.26
0.4 rad pre-torsion	99.42	81.23
0.6 rad pre-torsion	98.43	71.64

Furthermore, computational simulations were conducted to evaluate the Young's modulus of Cu nanowires at various loading paths of pre-torsional tension and temperatures. Scatter plots of the stress-strain responses before the onset of plastic deformation for the nanowire under different pre-torsional tension at 300 K are presented in Fig. 3.3(b). The slopes of the linear fits for the stress-strain responses under 0 to 0.4 rad pre-torsional tension do not show much divergence, implying that the Young's modulus does not depend too much on the loading path effect. This phenomenon is more obvious at lower temperature of 10 K, as can be seen in table 1. At this temperature level, Young's modulus obtained from 0.6 rad pre-torsion tension is only 2.4% smaller than that from 0 rad pre-torsional tension. However, when the temperature increase to 300 K, the Young's modulus is 71.64 GPa under 0.6 rad pre-torsional tension, 15.8% smaller

than that under 0 rad pre-torsional tension. The temperature effect on reducing Young's modulus is much greater than pre-torsional loading path effect and values of Young's modulus decrease much at higher temperature and larger pre-torsional angle.

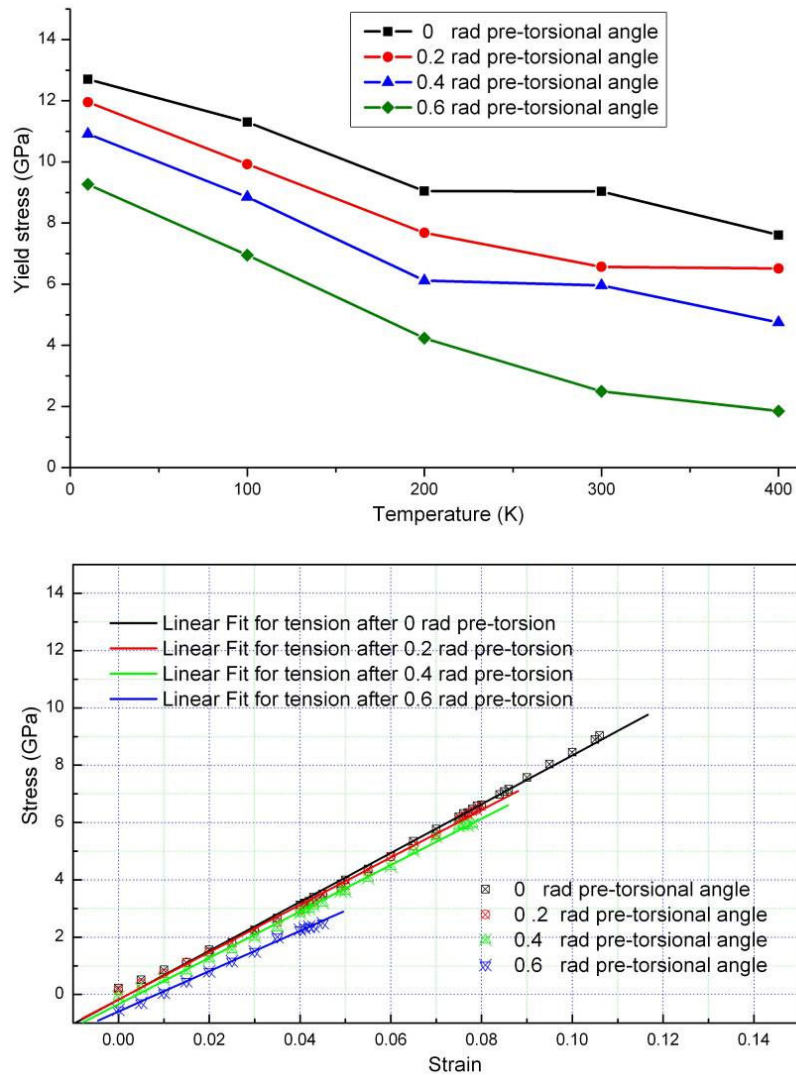


Figure 3.3 (a) Yield stress as a function of temperature of the  $40a \times 10a \times 10a$  nanowire under tension after various angles of pre-torsion. (b) Scatter plots for determination of Young's modulus for tension after various pre-torsion at 300 K.

(Jiang et al. 2010)

### 3.2.2 Deformation Mechanism

In our previous work (Jiang et al. 2009, Zheng et al. 2009, Jiang et al. 2010), the deformation mechanism of the metallic nanowires (Cu as an example) under different external loading conditions was studied. It was found that the deformation process can be divided into the following four different stages/moments (Jiang et al. 2009, Zheng et al. 2009):

(1) Elastic stage, in which the atomic structures undergo purely elastic deformation. The local lattice order of all atoms does not change and there is no dislocation in the sample. The corresponding total energy of the wire increases with the increase of tensile strain or the bending/torsional angle, that is, the external work done by the loads is transformed into the potential energy.

(2) Onset of the plastic deformation, where several partial dislocations emit from surfaces due to displacement mismatches between neighboring surface atoms, and then transmit in the close-packed planes of the wire. The corresponding total energy drops suddenly at this moment, which indicates that the plastic deformation starts.

(3) Earlier loading stage after the onset of plastic deformation, in which more and more dislocations appear and interact with each other. Thus, a lot of lattice defects, including stacking faults and twin boundaries, are formed and transect the sample, forming a defect network. The network evolves and the densities of defects increase rapidly in this stage.

(4) Later loading stage, in which dislocation activities are inhibited due to the pinning effect of the defect network. Therefore, the network becomes relatively stable and the densities of dislocation and stacking fault have little change in this phase. The

average coordination number of all atoms increases, because some atoms move into the interior of the sample. This change results in a decrease of the total surface area of the system via arranging atoms in a more close-packed pattern. Hence, the total energy decreases with the further increase of the tension or bending/torsion loads. It should be noted that although the initial sample may have a symmetrical geometry, but its deformed nanostructures are not symmetrical owing to thermal fluctuations.

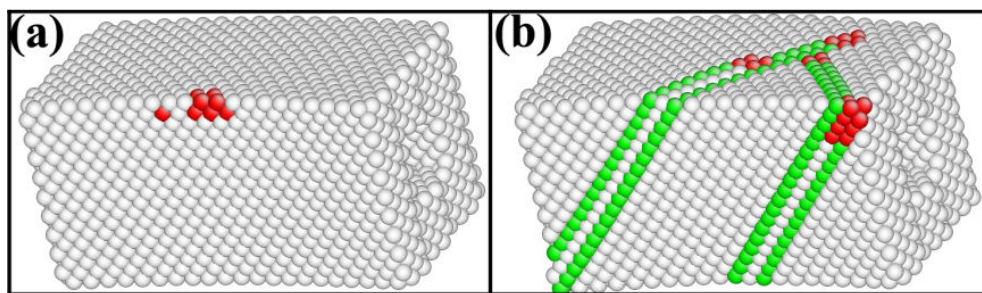


Figure 3.4 (a) Nucleation of partial dislocation from the corner of the free surface due to the atomic displacement mismatch and (b) partial dislocation propagation in several close-packed planes, resulting stacking faults lie in these planes. In this figure and Fig.3.5, fcc atoms are shown as white, hcp atoms are as green, disordered atoms are shown in red.

The nanowire was subject to a bending load. (Zheng et al. 2009)

In the previous studies on the deformation mechanism for nanocrystalline materials (Van Swygenhoven et al. 1999), it has been found that the plastic deformation is mainly accommodated by grain boundary sliding and dislocation activity. Thus, the material properties are dominated by the competition and interplay between these two mechanisms. However, in metallic nanowires shown in our studies, slip events occur initially at the places adjacent to free surfaces, which results in the emission of partial dislocations. Fig. 3.4 demonstrates the most common process of the nucleation of a

partial dislocation during the bending process. Since there are a large portion of atoms locating at the surfaces, surface-related activities play a dominant role in determining the mechanical properties of the nanowire.

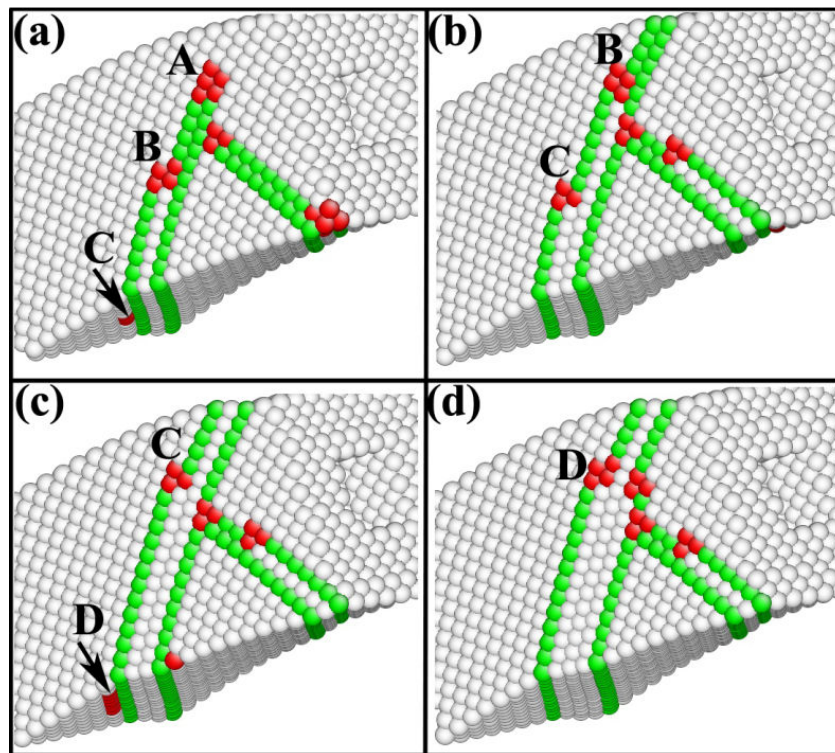


Figure 3.5 (a) Twinning process: (a) a partial is emitted from surface and (b) spreads in the bulk of nanowire, forming a twin by separating the hcp layers of an extrinsic stacking fault; (c) another partial of the same type is emitted and (d) propagates in the bulk, broadening the twin. (Zheng et al. 2009)

In the plastic deformation stage, twinning is found to be a popular deformation mode due to the sequent emission and propagation of partial dislocations. Fig. 3.5 shows a twinning process: First, a stacking fault is formed by the propagation of partials A and B in the  $\{\bar{1}11\}$  plane. Then, a partial C, which is of the same type as A and B, nucleates

from the bottom surface [see Fig. 3.5(a)] and transmits in the same  $\{\bar{1}11\}$  plane, separating the two hexagonal-close-packed (hcp) layers of the extrinsic stacking fault [see Fig. 3.5(b)]. Later, another partial D emits and propagates in the  $\{\bar{1}11\}$  plane, broadening the twin [see Figs. 3.5 (c) and (d)].

### 3.2.3 Formation of Special Nanostructures

Besides the general deformation mechanism discussed above, some special nanostructures, such as single, two and multi-conjoint fivefold twins (FTs) were also observed in our previous work (Jiang et al. 2010, Zheng et al. 2009, Jiang, Shen, et al. 2013). The fivefold twinned structures have attracted extensive interest due to their unique properties, ever since 1957 (Hofmeister 1998) when the early observation was reported. Over the past decades, they have been widely found in nanowires/nanorods (Lisiecki et al. 2000, Wu et al. 2006, Zheng et al. 2009) as well as in nanoparticles (Buffat et al. 1991, Cleveland, Luedtke, and Landman 1998, Cleveland et al. 1997, Nam et al. 2002), nanocrystalline metals and alloys (Liao et al. 2004, An et al. 2011). Symmetrical icosahedral and truncated icosahedral metallic nanoclusters with fivefold twins, for instance, have been routinely detected under various conditions in both experiments and simulations (Buffat et al. 1991, Cleveland, Luedtke, and Landman 1998, Cleveland et al. 1997, Ascencio et al. 1998, Wang, Teitel, and Dellago 2005).

In particular, with the success in laboratorial preparation of twinned nanowires (Wu et al. 2006, Kim et al. 2008, Sun and Li 2005), extensive studies have revealed many novel features of these wires, such as enhanced yield strength (Wu, Heidelberg, and Boland 2005, Cao and Wei 2006b), enhanced elastic modulus (Yoo, Oh, and Jeong 2010), and induced coiling motion (Zhu et al. 2012) due to the introduction of the intrinsic

fivefold axis, indicating that nanostructure-controlling mechanisms play an important role in tailoring the mechanical properties. Although multiple twinned icosahedra were commonly observed for spherical-like nanoparticles, previous study (Lisiecki et al. 2000) showed that only the direction of the fivefold axis of decahedra was possible for the growth of these well-defined long twinned nanorods.

Unlike conventionally utilizing thermal process for fine-sized nanoclusters (Cleveland, Luedtke, and Landman 1998, Nam et al. 2002, Baletto, Mottet, and Ferrando 2001, Apra et al. 2004), to explore the formation of the FTs in high-aspect-ratio nanowires and nanocrystalline materials, many efforts have been made by applying various external mechanical loadings, including tension (Cao, Wei, and Mao 2007), bending (Zheng et al. 2009, Zheng et al. 2008), combined torsional-tension (Jiang et al. 2010) and other loading conditions (Liao et al. 2004, Zhu et al. 2009). Only a single-formed FTs were found in most of these investigations (Liao et al. 2004, Cao and Wei 2006a, Jiang et al. 2010) with a few bi- and tri-conjoint FTs in the rest (Zheng et al. 2008, Zheng et al. 2009). Our most recent study (Jiang, Chen, et al. 2013) has showed that hex-conjoint FTs could be formed in bent fivefold twinned nanowires (FTNWs) before the dynamic failure occurs, which indicates that the intrinsic fivefold twin boundaries (TBs) may facilitate the formation of some possible multiple-twinned structures by carefully choosing external loading conditions.

However, no evidence has been reported in the open literature about the formation of icosahedral structures with multi-conjoint FTs in nanowires. In this section, our simulation results will show that the symmetrical quasi-icosahedral structures, which are rather similar to the icosahedral nanoclusters but actually different, can be formed in

several kinds of fivefold twinned metallic nanowires (Cu, Au and Ag) under dynamic tensile loading. This observation indicates that these quasi-icosahedral structures can also serve as one kind of possible deformation patterns in the twinned nanowires within the plasticity regime. By performing molecular dynamics (MD) simulations, the fivefold twinned nanowires with different cross-sectional shapes were modeled and simulated. To investigate whether the morphology of nanowire could affect the formation of the multiple twinned quasi-icosahedral structures, circular and pentagonal (Lisiecki et al. 2000, Wu et al. 2006, Kim et al. 2008, Sun and Li 2005) cross-sections that are commonly synthesized in experiments, as well as square ones that are studied in the previous theoretical work (Cao and Wei 2006b), were both considered.

For the current research in this dissertation, all MD simulations were performed using the semi-empirical EAM developed by Daw and Baskes (Daw and Baskes 1984). The Cu nanowire as a typical example were first considered. The parameters from the work of Mishin *et al.* (Mishin et al. 2001) were adopted for the EAM to describe the interactions between Cu atoms, which had been shown to accurately predict cohesive energy, elastic coefficients and stacking fault (SF) energy. The nanowires with uniform interior FTs along the entire wire length were constructed by rotating coherent twins about  $\langle 110 \rangle$  axis and then were trimmed to form certain cross-sectional shapes, as depicted in Fig. 3.6. The radii of the cylindrical and pentagonal prismatic nanowires are  $\sim 6a$  (lattice constant  $a$  is 3.615 Å for Cu), while the width and height of the cuboid were set to  $10a$  to make the cross-section areas closed to each other. The lengths for all types of nanowires were chosen as  $60a$ .

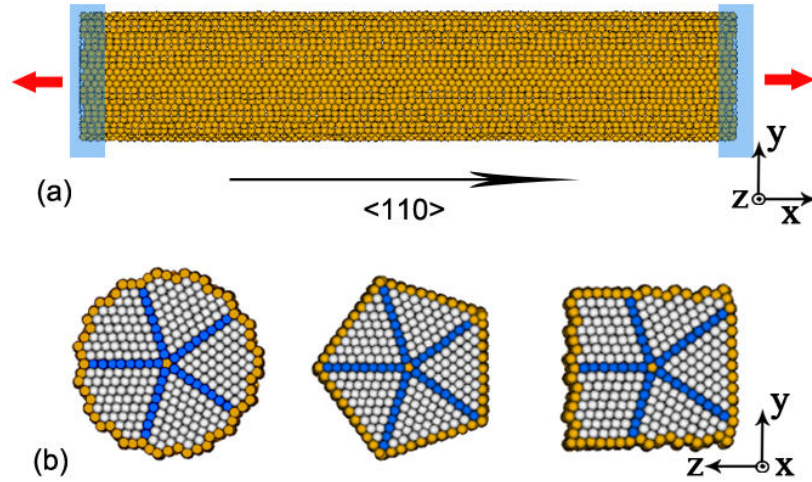


Figure 3.6 Schematic diagram of the simulation models of fivefold twinned nanowires. (a) Side view with  $\langle 110 \rangle$  axis orientation; (b) Cross-sectional views of three different types of nanowires, namely, cylindrical, pentagonal prismatic and rectangular cuboid nanowires. The tensile loadings are applied along  $\pm x$  directions, as indicated by the two arrows. The atoms shown (in current and later figures of this section) in off-white, blue, and red are those in local fcc, hcp and icosahedral lattices; while disordered atoms in gold represent free surfaces or dislocation cores. (Jiang, Shen, et al. 2013)

After the initial geometrical models were established, each nanowire was thermally equilibrated at the room temperature (298 K) for 100 ps by using a Nosé-Hoover thermostat (Nosé 1984, Hoover 1985). Then, dynamic tensile loads with a set of strain rates ( $0.001\% \text{ ps}^{-1}$ ,  $0.01\% \text{ ps}^{-1}$  and  $0.1\% \text{ ps}^{-1}$ ) were applied to the samples at the two ends, which was similar to the procedures used by Ikeda, Zhou, Park and co-workers (Ikeda et al. 1999, Park and Zimmerman 2005, Liang and Zhou 2005). The system temperature was controlled at 298 K, and no periodical boundary conditions were used during this process. Based on CNA (Tsuzuki, Branicio, and Rino 2007), the local atomic

structures were classified to facilitate the identification of the dislocation cores, SFs and TBs.

Our simulations first demonstrated that the quasi-icosahedral structure can be formed by the interplay between the secondary fivefold deformation twins (FDTs) and the intrinsic fivefold axis at the stage of necking process during the plastic process. An example of a tensile process at a strain rate of  $0.001\% \text{ ps}^{-1}$  for a cylindrical FTNW is shown in Fig. 3.7. The typical stress-strain curve plotted in Fig. 3.7(a) shows that the tensile stress keeps increasing with the increase of the strain until the limit strength is achieved within the elastic regime. Then, an abrupt drop of the stress around  $\sim 6\%$  strain indicates that the plastic deformation starts and defects are nucleated. The stress decrease also corresponds to a rapid increase on the fraction of atoms in the hcp lattice, as shown in Fig. 3.7(b). However, unlike the rearrangement of the hcp atoms to fcc atoms as observed in the previous work (Wen et al. 2012), the fraction of hcp atoms still experiences a slight increase and TBs (mostly containing hcp atoms) are formed. These TBs are connected with each other and build up secondary FTs in each subunit around the original fivefold axis. As illustrated in the snapshot at  $\sim 8\%$  tensile strain, a well-defined symmetrical intermediate twinned structure is visually formed with the initially shrinkage of wire cross-section. This structure consists of five pairs of two conjoint FDTs, which are very similar to those reported in our previous work for single crystal nanowires. Interestingly, this intermediate twinned pattern distributes almost equally on both sides of the necking region with each pair of the adjacent FTs sharing the same TB in the middle, forming another smaller “FTNW” in the neck. The fivefold axis of the neck actually has a relative twisted angle to the original one of the entire wire. As the

strain further increases, the “smaller nanowire” is elongated to a much thinner chain with longer TBs (see the snapshot at the strain of ~17%). The neck region breaks apart upon the tensile strain reaches ~20%, and finally forms two quasi-icosahedral structures at the fracture point of each broken part. These quasi-icosahedral structures are shown to be stable once they are formed, with the capability of remaining their morphology even after the breakage of the nanowire.

The peculiarities of the quasi-icosahedral structures are illustrated with the atomic configurations in Fig. 3.8. The first panel of Fig. 3.8(a) geometrically shows the construction of an ideal icosahedron with its 12 vertices orthogonally projected to the y-z plane along  $\langle 110 \rangle$  direction. The dots labeled by letters denote the loci of fivefold symmetrical centers with 30 edges corresponding to the intrinsic and deformation TBs. The quasi-icosahedral structures actually formed in the nanowires are shown in the other panels of Fig. 3.8(a). The cylindrical wire in the second panel can be taken as a typical example to compare the similarity and difference between the ideal and quasi icosahedral structures. Similar to an icosahedron, the quasi-icosahedral structure is bound by 30 TBs, but five of them are initially from the preexisting fivefold axis. Unlike the 20 identical equilateral tetrahedrons included in the ideal icosahedron, there are only 15 tetrahedral fcc subunits in the quasi-icosahedral structures. Another five subunits are actually the original quasi-triangular prisms with the fivefold symmetry, and their outer facets enclose the wire cross-section. Thus, instead of 12 vertices, the quasi-icosahedral structure only have 11 fivefold centers (O and  $\alpha-\kappa$ ) formed in the fractured region, with a long intrinsic fivefold axis (center marked as O'). The finally formed FDTs (denoted as O) is coaxial with the center O' of the wire, but each TB has a  $\sim 36^\circ$  off the original corresponding one,

which makes the fivefold axis appear to be twisted upon the quasi-icosahedral structure forms.

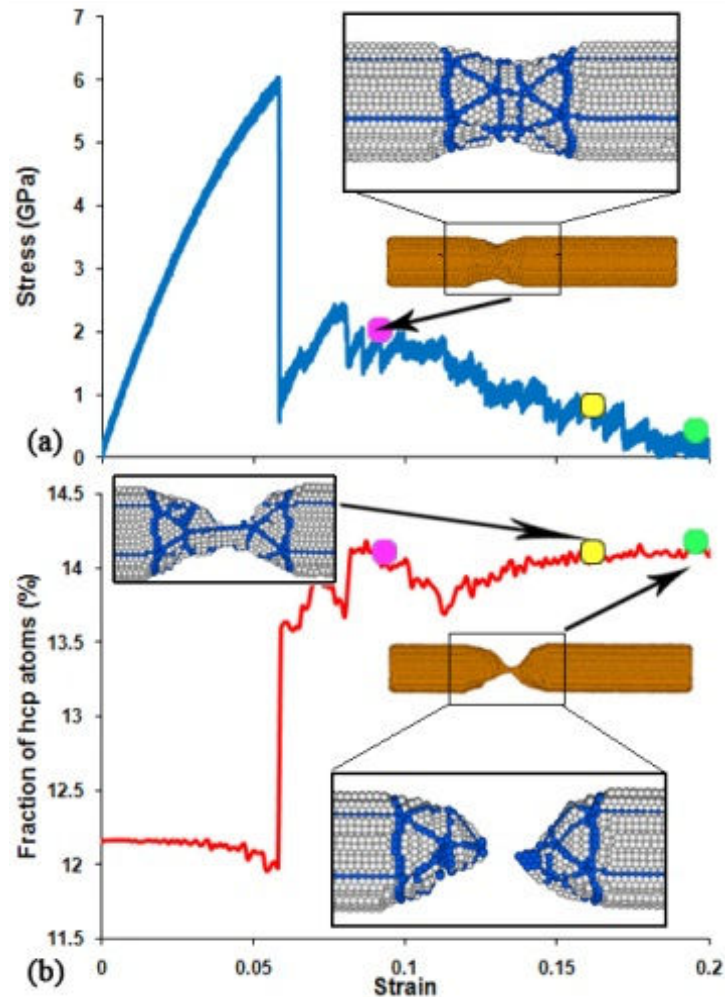


Figure 3.7 (a) Stress-strain curve and (b) fraction of hcp atoms as a function of strain for a cylindrical nanowire under tension at a strain rate of  $0.001\% \text{ ps}^{-1}$ . The insets are the snapshots of atomic configurations at different strain values. In the expanded scaled insets, surface atoms are not shown to facilitate visualizing the twins. (Jiang, Shen, et al. 2013)

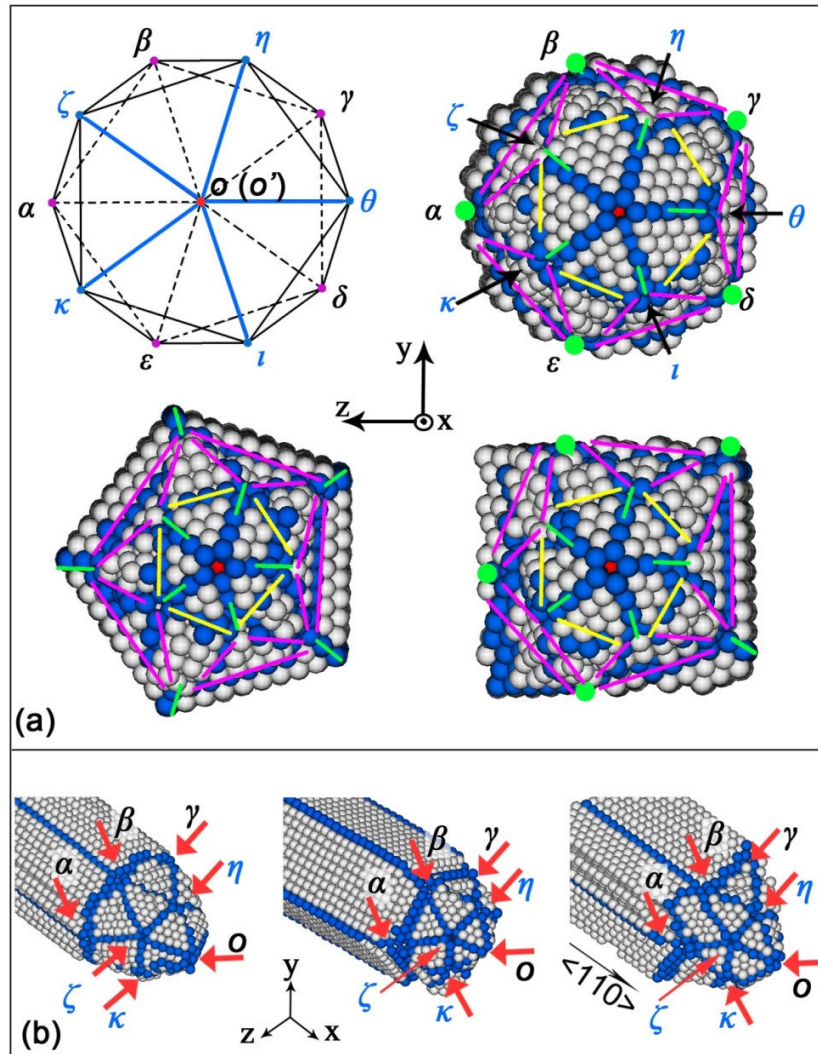


Figure 3.8 Shape and composition of quasi-icosahedral structures formed in the fivefold nanowires. (a) Morphology from the cross-sectional view of the nanowires, with the comparison by a sketch of ideal icosahedron; (b) Spatial distributions of the fivefold twins in the quasi-icosahedral structures from different viewpoints. Only fcc, hcp and icosahedral atoms are shown for clarity. The TBs in panel (a) are marked by colored lines and green dots. The green dots indicate those TBs of the intrinsic fivefold axis that are perpendicular to the y-z plane.(Jiang, Shen, et al. 2013)

Besides the FTs O and O', other ten secondary FDTs are hierarchically distributed along the  $\langle 110 \rangle$  fivefold axis between O and O' by two groups. The relative positions of the two groups of FTs are shown in Fig. 3(b) from clearer viewpoints. The centers of FDTs  $\alpha-\varepsilon$  are located on the same plane perpendicular to the wire axis. They are adjacent to the undeformed part of the wire, sharing the preexisting TBs with the fivefold axis of the wire. The centers of FDTs  $\zeta-\kappa$  are located on another plane which is more closed to the breakpoint of the nanowire. Each of them contributes one TB and forms the FTs by sharing a common center denoted as point O. From Fig. 3.8(b), one can also observe that the outline of the quasi-icosahedral structures is actually different from that of those "spherical-like" icosahedral nanoclusters. These structures are hemispherical-like and serve as "caps" in the ends of the newly formed "broken" nanowires after the abrupt at their limit strain. Thus, they define the profile of the fractured regions to be a closely hemispherical shape with 25 TBs formed during the tensile deformation process.

Besides fivefold twinned Cu nanowires discussed above, other three metals including Au, Ag and Al with EAM parameters from Foiles (Foiles, Baskes, and Daw 1986), Mishin and co-workers (Zope and Mishin 2003), respectively, were further considered in the current work. Quasi-icosahedral structures were also observed in Au and Ag FTNWs, while have not been found so far in our tensile simulation of Al ones (see Fig. 3.9). This can be explained by the different stacking-fault energy (SFE) of the metals. For relatively low SFE metal, such as Au, Ag, and Cu, twins and partial dislocations can be abundant and thus increase the possibility of forming multiple-twinned structures (Liao et al. 2004). In contrast, for high SFE metals like Al, the material usually deform by glide of full dislocations and twins can be rarely found

(Rohatgi, Vecchio, and Gray Iii 2001), as illustrated in Fig. 3.10. Thus the quasi-icosahedral structure is very difficult to form in Al nanowires.

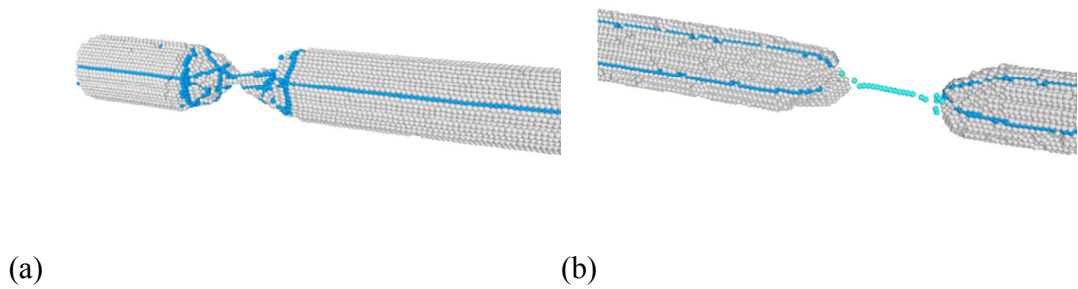


Figure 3.9 Atomic configurations of fivefold twinned (a) Ag and (b) Al nanowires under tension. The atoms shown in off-white, blue and light blue are those in local fcc, hcp and icosahedral lattices. Disordered and surface atoms are removed for clarity.

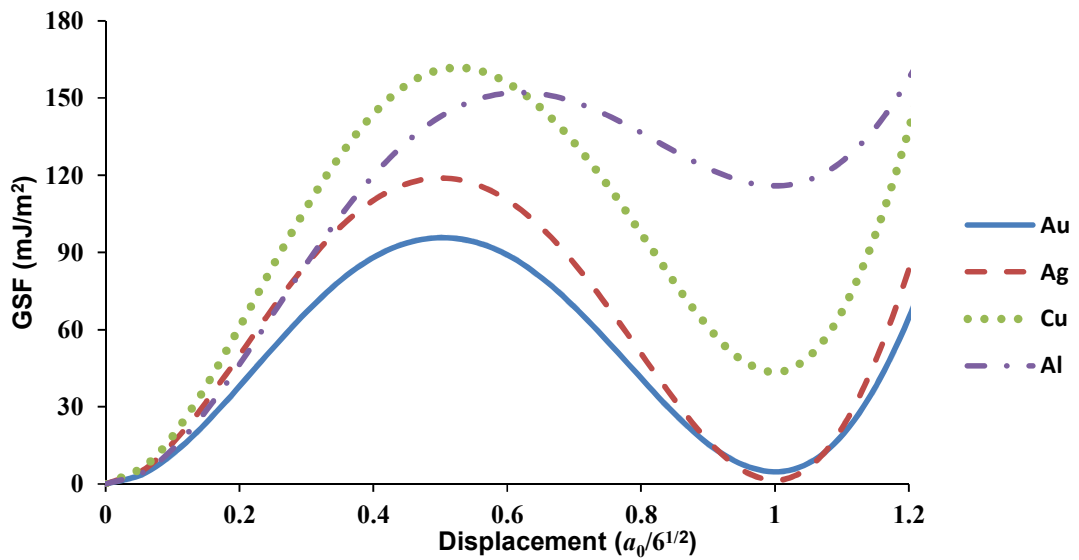


Figure 3.10 Generalized stacking fault energy (GSF) curve for Au, Ag, Cu and Al.

The formation of quasi-icosahedral structures, which has not been reported in the previous studies, indicates that the unique multi-twinned pattern could also be a possible mode for plastic deformation in the FTNWs under external mechanical loading. The results in Fig. 3.8 also demonstrate the independence of these structures on the cross-sectional shape, since they are observed in all the cases including cylindrical, pentagonal prismatic and cuboid nanowires. Furthermore, the configurations of these structures actually evolve during the successive twinning processes with three different strain rates used in this study from 0.001% to 0.1% ps<sup>-1</sup>. As a result, the strain rate effect, which is considered as an important factor on the limit strength and structural transformation for single crystal nanowires (Ikeda et al. 1999, Liang and Zhou 2005, Park and Zimmerman 2005), appears to be negligible for the formation of the quasi-icosahedral structures from the fivefold twinned ones. As compared with the negligible effects of cross-sectional shape and strain rate, the intrinsic fivefold twinned axis plays an important role in facilitating the successive twinning process, serving as a natural framework for these quasi-icosahedral structures to occur. On the other hand, the icosahedral structure is known to be more stable than crystalline structures, since it presents only (111) closed-packed surfaces and a lower surface/volume ratio at small sizes (Baletto, Mottet, and Ferrando 2001, Apra et al. 2004). However, additional deformation energy is required to form this structure due to the distortion of the lattice. As the necking process in the nanowires evolves, there is a localized deformation (energy) zone in the rapidly decreased cross-sectional area, which is the reason why the necking regions become more favorable locations for the quasi-icosahedral structures to form.

Unlike the conventionally thermal process for the formation of icosahedral structures in nanoclusters (Nam et al. 2002, Cleveland et al. 1997, Cleveland, Luedtke, and Landman 1998, Baletto, Mottet, and Ferrando 2001, Apra et al. 2004) associated with liquid-solid phase transition (Shen, Wu, and Lu 2013), the simulation results shown in this section indicate that the quasi-icosahedral structures can form in the nanowires with tensile loading at room temperature without any phase transition. An ideal fivefold-twinning process in those nanoclusters is usually accommodated by elastic strain (Gryaznov et al. 1999, Shen, Wu, and Lu 2013), while in these pre-twinned nanowire, the aforementioned plastic deformation in the necking region as well as the intrinsic FTs can serve as driven-forces to facilitate the formation of quasi-icosahedron by providing an additional stress field for the nucleation of secondary FTs. These quasi-icosahedral structures with multi-conjoint FTs might have a stronger twinning-reinforcement effect on the mechanical properties of nanowires. Recent results have also shown that the phase transformation and plasticity could be affected by the temperature in the Fe FTNWs (Wu et al. 2011). However, it is not clear whether there is an influence of temperature on the formation of the quasi-icosahedral structure, which requires a further study.

### **3.3 Impact Response of Nanostructures**

As reviewed in Sec 3.1, the impact response of nanostructures has become a research topic of current interest due to its potential use in nanocomposites subject to extreme loading conditions. Atomistic simulations of shock-induced plasticity in Cu carried out by Holian and Lomdahl (Holian and Lomdahl 1998) have revealed that stacking faults can be nucleated by preexisting extended defects for shock strengths below the yield strength of the perfect crystal. Bringa *et al.* (Bringa et al. 2006)

performed MD simulations of shocked Cu designed to obtain a detailed understanding of dislocation flow at high strain rates; they observed three distinct regimes of lattice relaxation, namely, dislocation nucleation, transport, and immobilization due to tangling and other interactions. They found that the stress can relax to an approximately hydrostatic state and the dislocation velocity can drop to nearly zero. Tanguy *et al.* (Tanguy et al. 2003) investigated the mechanism for the nucleation of defects responsible for plastic flow in a  $\langle 100 \rangle$  face-centered-cubic (fcc) perfect crystal under impact, and estimated the activation energy for the formation of an edge dipole under high pressure. Using MD simulations, Luo *et al.* studied the spallation in solid and liquid Cu at high strain rates induced by planar shock loading (Luo, Germann, and Tonks 2009), explored the anisotropic shock response of columnar nanocrystalline Cu (Luo et al. 2010), and investigated the effect of asymmetric grain boundaries on the shock response of Cu bicrystals (Han et al. 2012); their results show pronounced deviation from planar loading due to the grain boundaries and strong anisotropy in both elasticity and plasticity.

Collectively, these studies above have demonstrated the complexity of impact responses at the nanoscale. However, because they were performed for simulation cells periodic in the directions transverse to the shock direction, there is still a lack of understanding of the effects of sample size and impactor/target aspect ratio on the responses of the nanostructures to impact loading. It appears from the transmission electron microscopy images that discrete zero-dimensional (particle) and one-dimensional (rod and beam) nanostructures of certain sizes will interact with each other via longitudinal (particle to rod or rod to rod), transverse (particle to beam or beam to beam) and/or mixed impact modes when detonation occurs (Apperson et al. 2007). Due

to the limitation of available experimental techniques, it is still not feasible to observe and measure the nanoscale interactions under impact loading in real-time.

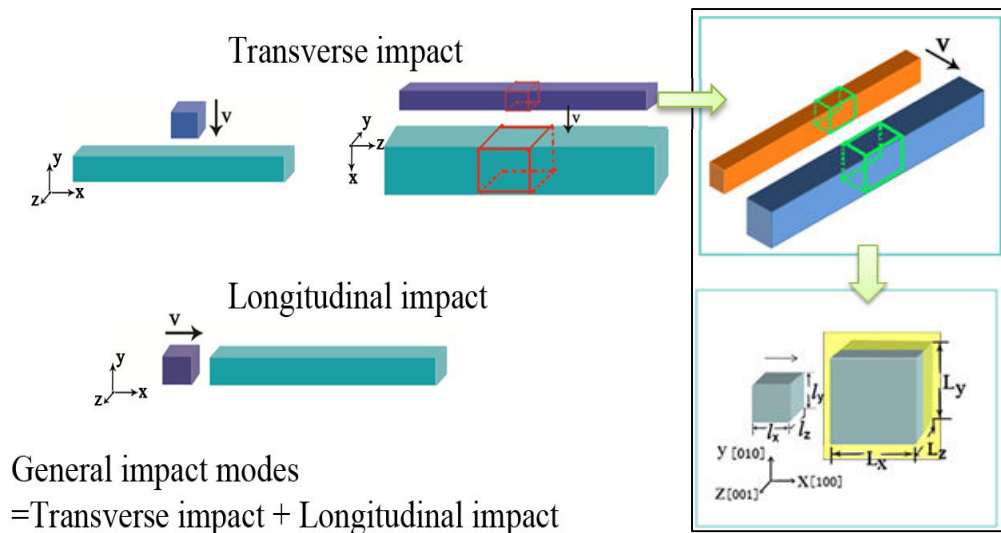


Figure 3.11 Decomposition of the general impact mode among discrete nanostructures, with the middle box on the two beams in transverse impact indicating the periodical boundary conditions to be used in molecular dynamics simulation. In the transverse impact mode, it can be further composed to a particle-beam model and a beam-beam model.

To simplify the problem, the computational models of impact mechanics are proposed in our current study, decompose the general impact mode into the longitudinal and transverse one, respectively, as illustrated in Fig. 3.11. In this chapter, our recent findings are summarized about the size effect on the impact responses of nanostructures to the separate transverse and longitudinal loading conditions. Atomistic modeling and simulations were performed to study the size effect on the responses of nanostructures (Cu and Al as representatives) to transverse and longitudinal impact loading, respectively, with a focus on the impact pressure, defect nucleation and growth (Chen,

Jiang, et al. 2012, Chen, Jiang, and Gan 2012, Jiang et al. 2012, Jiang, Chen, et al. 2013). Since the MD simulations of nanostructural responses to impact loading are based on the embedded-atom method (EAM) (Daw and Baskes 1984), the results presented here are applicable to the type of metal nanostructures governed by the EAM potential. The research presented in this chapter might provide the promising avenues for investigating the size effects on the general responses of nanostructures to impact loading.

### 3.3.1 Transverse Impact

As illustrated in Fig. 3.11, the transverse impact mode can be further composed to a particle-beam model and a beam-beam model. The major findings discovered in this sub-section will be only focused on the beam-beam model, with discussions of the stress state, defect formation, and size and aspect ratio effect. The atomistic modeling and simulation of particle-beam model can be found in detail in our recent publications (Jiang 2013, Jiang, Chen, et al. 2013).

The beam-beam impact model used for MD simulations is depicted in Fig. 3.11 via the middle box on the two beams in the mode of transverse impact. The simulation model consists of a metallic single-crystal flyer with width  $\times$  height  $\times$  thickness of  $l_x \times l_y \times l_z$  impacting along the  $x$ -direction onto a metallic single-crystal target with width  $\times$  height  $\times$  thickness of  $L_x \times L_y \times L_z$ . The system is periodic along the  $z$ -direction (the beam axis) but non-periodic along the  $x$ - and  $y$ -directions, and therefore corresponds to the face-to-face impact between two infinitely long nanobeams. The aspect ratio between the flyer and target is defined as the ratio of  $l_y/L_y$  between flyer and target heights.

The MD simulations were performed using the simulation package (LAMMPS) with the EAM force field (Mishin et al. 2001, Daw and Baskes 1984, Plimpton 1995).

Starting with the flyer and target separated by a face-to-face distance of 7.26 nm, the system was equilibrated for 25 ps at  $T = 298$  K in the isochoric-isothermal (NVT) ensemble using the Nosé-Hoover thermostat (Nosé 1984, Hoover 1985) in order to relieve the stressed state resulting from the introduction of free surfaces in the x- and y-directions. Then, an initial impact velocity was applied to the x-component of the velocities of the atoms in the flyer, and the impact process is simulated in the isochoric-isoenergetic (NVE) ensemble for 15 ps. All simulations were performed using the velocity Verlet integrator with a time step of 0.5 fs.

Similar to the atomistic modeling and simulation discussed in Section 3.2, CNA (Tsuzuki, Branicio, and Rino 2007) was used to facilitate the visualization of the local structural deformation. In the simulation results to be described in the remaining parts of Section 3.3, fcc atoms are shown as grey, hcp atoms blue, other twelfefold-coordinated atoms green, and the remaining atoms (classified as disordered) brown. A local crystalline structure is referred to an intrinsic stacking fault if it contains two adjacent layers of atoms in the local hcp structure, an extrinsic stacking fault if it contains two hcp layers separated by a single fcc layer, and a twin boundary if it consists of a single hcp layer. Disordered or non-structured atoms are typically located at free surfaces or dislocation cores.

Two materials, Cu and Al, were considered with the EAM parameters developed by Foiles et al., (Foiles, Baskes, and Daw 1986) and Zope and Mishin (Zope and Mishin 2003), respectively. As a result, the MD simulation results are representative of a class of fcc metal single crystals. For all the simulation cases, the widths of the flyer and target samples are selected to be  $l_x = 10a$  and  $L_x = 40a$ , with  $a$  being the lattice length. Suitable

sample thickness  $l_z = L_z$  along the axial direction of the nanobeams must be chosen in order to eliminate the finite-size effect on the formation and growth of geometrically constrained dislocations due to the periodic boundary conditions in the  $z$ -direction. The effect of sample thickness on the deformation patterns and corresponding impact pressure in the target has been investigated in our recent study (Chen, Jiang, et al. 2012). The impact pressure is defined to be the negative of the principal stress along the impact direction (along the  $x$ -axis), calculated from the average stress tensor evaluated for a subset which is initially centered on the centerline of the target at the distance  $5a$  from the impact surface, and is tracked during the impact process. The size of the subset is chosen such that increasing the number of atoms in it does not lead to significant change in the calculated stress value. The time origin for trajectory analysis is taken to be the instant at which the flyer contacts the target. As discussed in our recent work (Chen, Jiang, et al. 2012), it was concluded that increasing the system thickness beyond a certain value (*i.e.*,  $40a$ ) does not significantly affect the pressure time history. The flyer and sample thickness  $l_z = L_z = 40a$  is chosen for all subsequent calculations in this sub-section.

To describe the size and aspect ratio effects on the transverse impact response of fcc metal single crystals, the relationship between the particle velocity (one half of impact velocity for the problem considered here) and peak pressure is illustrated in Fig. 3.12 for different Cu specimens. In addition to the obvious dependence of the peak pressure on the particle velocity, the shock Hugoniot is also dependent on the aspect ratio with a constant target height  $L_y$ . The results for both aspect ratios are well described by a quadratic relationship; this general outcome is consistent with empirical expectations. However, different flyer sizes yield different quadratic curves, a result that cannot be explained with

the existing theories. The Hugoniot loci for single-crystal Cu obtained experimentally by Chau et al. (Chau et al. 2010) for shock wave loading into the elastic-plastic (two-wave) region and from MD simulations by Bringa et al. for elastic shock wave loading are also shown in Fig. 3.12; both of those results fall between the current ones and are well-described by quadratic fits.

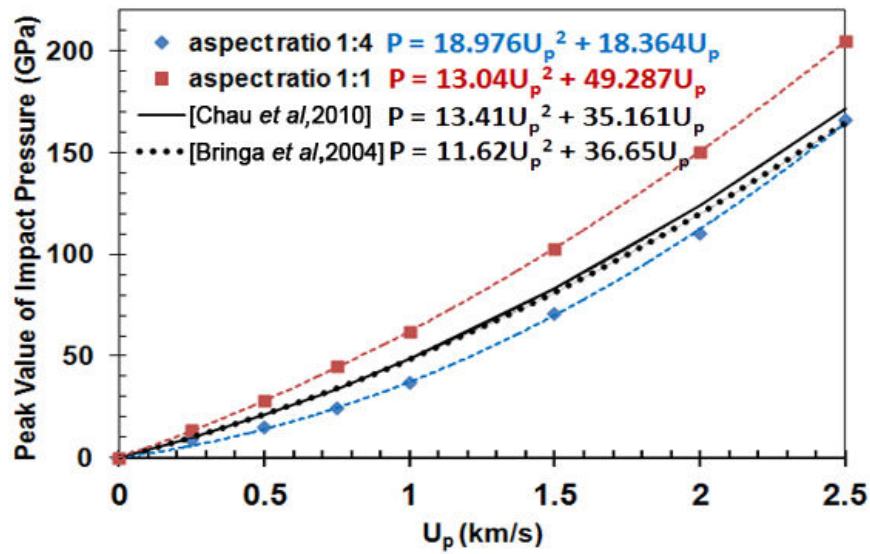


Figure 3.12 Peak stress vs. particle velocity curves for the systems with aspect ratios 1:4 and 1:2, as well as the comparison with the experimental (Chau et al. 2010) and theoretical (Bringa et al. 2004) results for the transverse impact response of single-crystal Cu samples (Chen, Jiang, et al. 2012).

The results on the transverse impact response of Al single crystals are given in Fig. 3.13. Although there are no corresponding experimental data available for comparison, the simulated Hugoniot loci for both Cu and Al single crystals exhibit the similar trend as can be seen from Figs. 3.12 and 3.13. It appears from the comparison between the MD simulation at nanoscale and experimental data at microscale for Cu single crystals that the MD simulation results with a smaller flyer and those with a larger flyer size might provide the lower and upper bounds of the experimental data,

respectively. Hence, it would be significant for better characterizing the shock responses of metal structures if the mechanism behind this observation is understood.

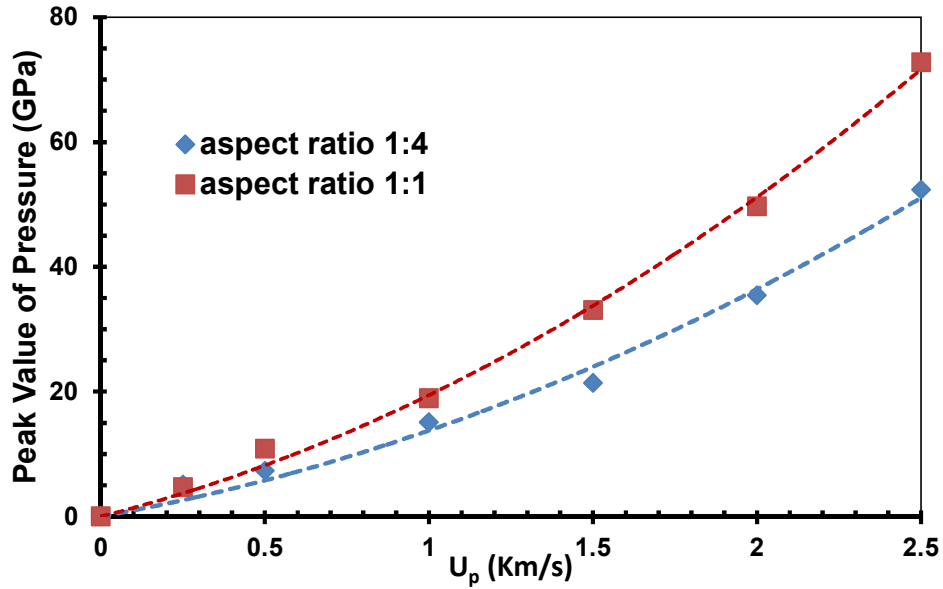


Figure 3.13 Peak stress vs. particle velocity curves for the systems with aspect ratios 1:4 and 1:2 for the transverse impact response of single-crystal Al samples.

To clarify the size and aspect ratio effects, the effect of aspect ratio  $l_y/L_y$  on the impact stress and number fraction of hcp atoms in the Cu target sample is shown in Fig. 3.14 for the fixed target size of  $40a \times 40a \times 40a$ . It can be observed that (1) the peak pressure values are reached within 1 ps after impact; (2) the peak pressure for the system with the 1:4 aspect ratio is only about 55% of that for the system with the 1:1 aspect ratio; and (3) the peak number fraction of hcp atoms occurs about 7 ps after impact, corresponding approximately to the time when the release wave reaches the impact surface for all three aspect ratios; and (4) the maximum number fraction of hcp atoms decreases with decreasing aspect ratio for a fixed value of  $L_y$ . Although for  $l_y/L_y \neq 1:1$  the shock wave will be divergent (approximately cylindrically expanding), the shock waves

for all three aspect ratios can be considered to be approximately planar at the location where the peak pressure is reached, because the impact pressure is measured near the impact surface (Chen, Jiang, et al. 2012).

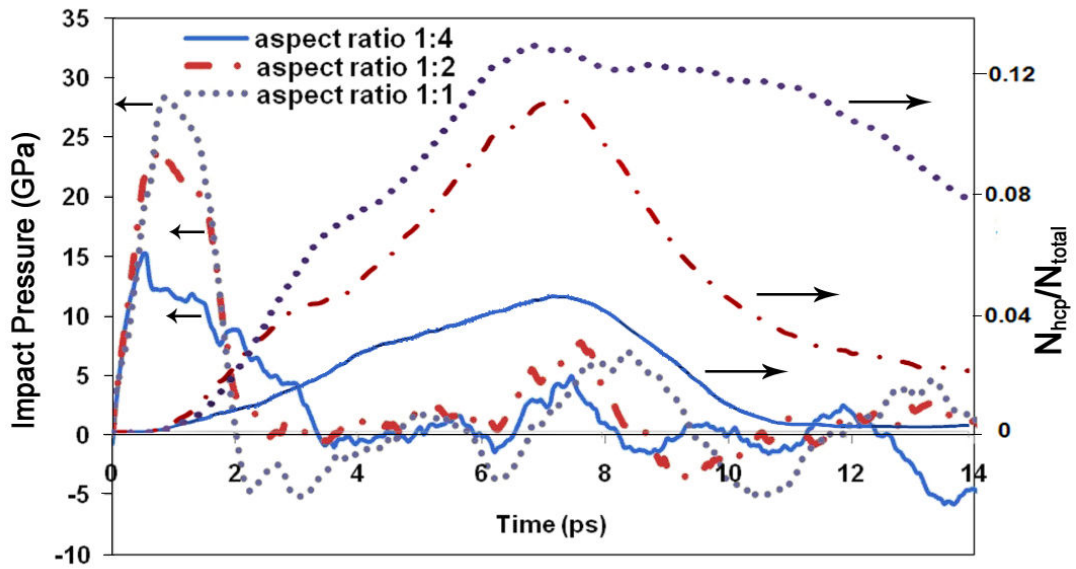


Figure 3.14 Peak Time histories of the impact pressure and number fractions of target atoms in hcp crystal structures for the Cu systems with aspect ratios 1:4, 1:2, and 1:1, respectively.(Chen, Jiang, et al. 2012)

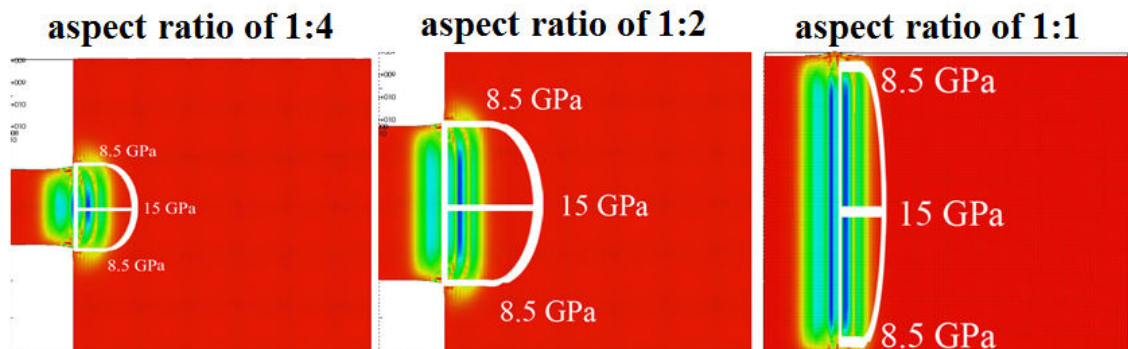


Figure 3.15 Stress distribution predicted by MPM simulations with different aspect ratios.

For the purpose of qualitative comparison, numerical solutions for the nanobeam

impact problem based on continuum mechanics (MPM simulations) were also obtained for the systems with the same relative dimensions as considered here. As shown in Fig. 3.15, MPM simulations show that the average impact pressure is independent of the flyer size although they predict a higher impact pressure in the middle and lower pressure at the corners of the impact surface due to stress concentration effects.

By contrast, the impact pressure in the MD simulation is found to decrease with decreasing aspect ratio, as shown in Fig. 3.14. The explanation for the apparent aspect ratio effect might be due to the distance between the two corners of the impact surface. As shown in Fig. 3.16(a) and (b) for aspect ratios 1:4 and 1:2, respectively, the disordered atoms in the MD simulations first appear approximately uniformly across the impact surfaces then evolve toward the midline of the target sample. Due to the shorter distance between the surface corners, the disordered atoms in the sample with smaller  $l_y$  coalesce sooner than those in the sample with larger  $l_y$ . As further demonstrated in Fig. 3.16(c) and (d) for the aspect ratio 1:4 and 1:2, the stress state in the highly disordered regions in the sample with smaller aspect ratio is more liquid-like, based on the smaller difference between the maximum and minimum principal stresses, and therefore less able to support large shear stresses. Hence, the smaller the distance between the two corners of the impact surface, the lower the peak stress that can be attained, an effect that becomes more pronounced with increasing impact speed, as demonstrated by the results in Fig 3.12. In addition, the overall fraction of disordered atoms increases with the increase of  $l_y$ , due to the larger volume of material within which the probability of dislocation nucleation is high. Consequently, the number fraction for the hcp atoms increases with the increase of  $l_y$ , as shown in Fig. 3.14.

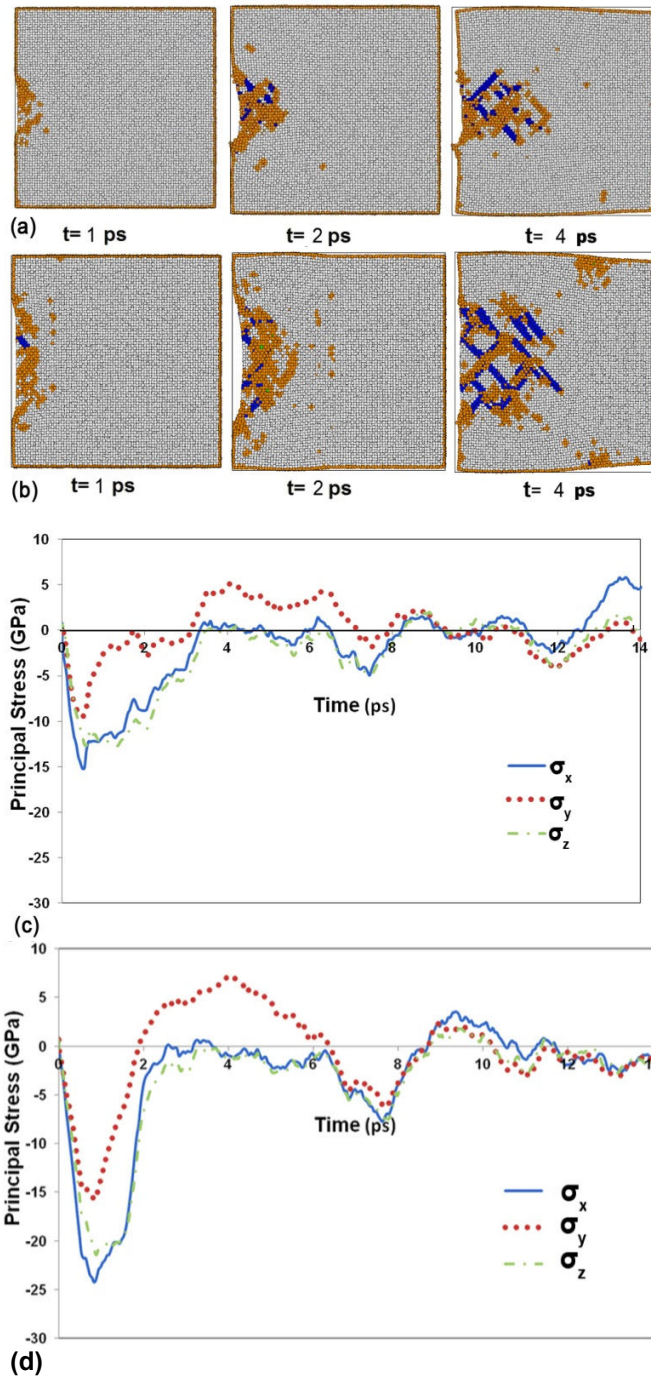


Figure 3.16 (a) and (b): Target deformation patterns with time. Aspect ratios are: (a) 1:4 and (b) 1:2. (c) and (d): Time histories of the principal stresses in the target. Aspect ratios are: (c) 1:4 and (d) 1:2.

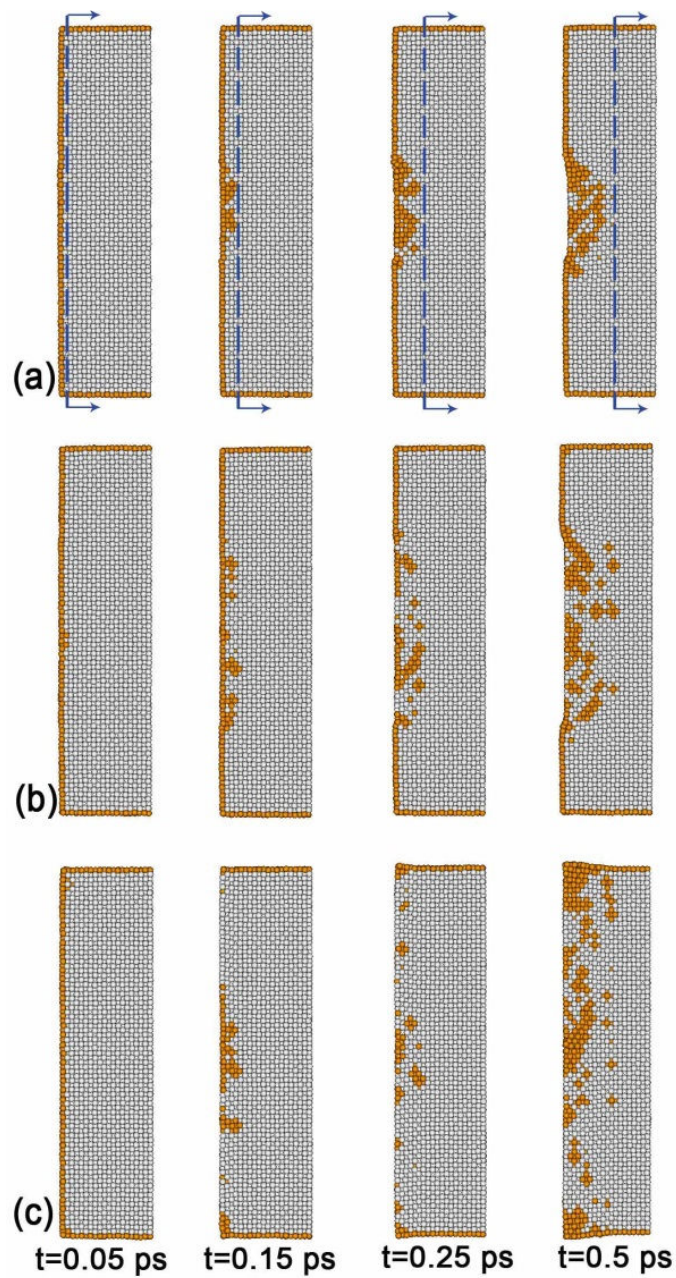


Figure 3.17 Atomic configurations at times 0.05, 0.15, 0.25, and 0.50 ps for (a) simulation 2, (b) simulation 8, and (c) simulation 10. Only the target atoms in the region between 0 – 10a along the x-direction are shown. The arrows and dashed vertical lines in panel (a) denote the direction and instantaneous position of the shock front.

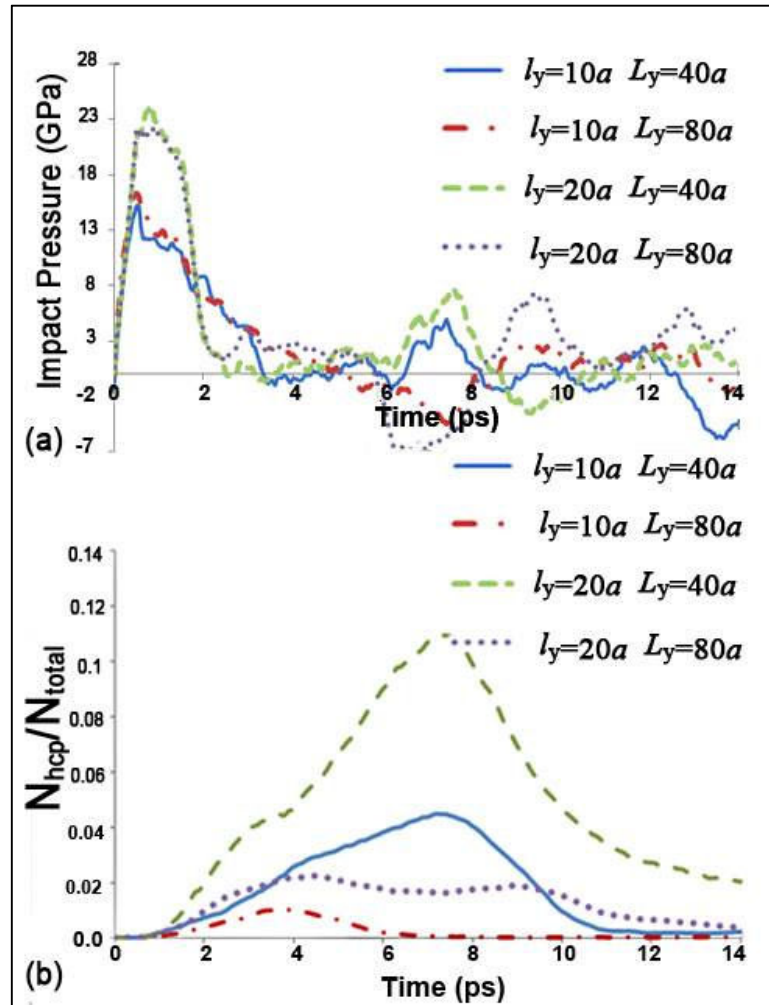


Figure 3.18 Time histories of (a) the impact pressure and (b) the number fraction of target atoms in the hcp crystal structure for the Cu systems with different size and aspect ratios (Chen, Jiang, et al. 2012).

Furthermore, the front of disordered atoms developing near the impact surface propagates initially at a speed close to the shock wave speed, as shown in Fig. 3.17 for the target region adjacent to the impact surface; and then slows down as dislocations form, as illustrated for the whole target sample in Figs. 3.16(a)-(b), noting that the shock wave at  $t = 1$  ps is about 1/3 of the way through the 40a width of the target. It can also be observed from Fig. 3.17 that the disordered atoms in the sample with smaller  $l_y$  coalesce

sooner than those in the sample with larger  $l_y$  due to the shorter distance between the corners of the impact surface.

To confirm that the distance  $l_y$  between corners of the impact surface is the key factor for explaining the above observations, the simulation results for the Cu systems with different size and aspect ratios are shown in Fig. 3.18. As can be seen from Fig. 3.18(a), the impact pressure is not sensitive to the aspect ratio for a given flyer size but instead is dependent mainly on  $l_y$ . The explanation is that for a given aspect ratio  $l_y/L_y$ , increasing the flyer size  $l_y$  will increase the impact pressure, for the reasons discussed above. Hence, the “aspect ratio effect” is due mainly to the distance between the corners of the impact surface. Figure 3.18(b) demonstrates that the number fraction of hcp atoms in the target decreases with increasing target size, because the total number of atoms in the large target is greater than that in the small target. In other words, the hcp zone appears to be localized.

### 3.3.2 Longitudinal Impact

To investigate the size effect on the longitudinal impact response in Fig. 3.11, atomistic models of Cu nanorods were considered, as illustrated in Fig. 3.19. The initial crystallographic directions [100], [010], and [001] coincide with the x-, y- and z-axis, respectively. The nanobars are comprised of a central target region of length  $l_t$  sandwiched between two flyers with the same length  $l_f$ . All three regions have equal square cross-sectional areas defined by edge length  $h$ . Thus, in a given simulation there are two flyers of size  $l_f \times h \times h$  and a target with size  $l_t \times h \times h$ ; the three regions initially are contiguous such that the overall initial system size is  $(2l_f + l_t) \times h \times h$ . Symmetric impacts are generated by assigning the two flyers equal but opposite velocities parallel to

the  $x$ -axis. In all cases the initial values of  $l_f$  and  $l_t$  are chosen to be  $20a$  and  $100a$ , respectively, with  $a$  being the Cu lattice constant. In order to study the size effect,  $h$  is set to three different values, namely  $10a$ ,  $20a$ , and  $40a$ , as can be found in detail in our recent work (Jiang et al. 2012).

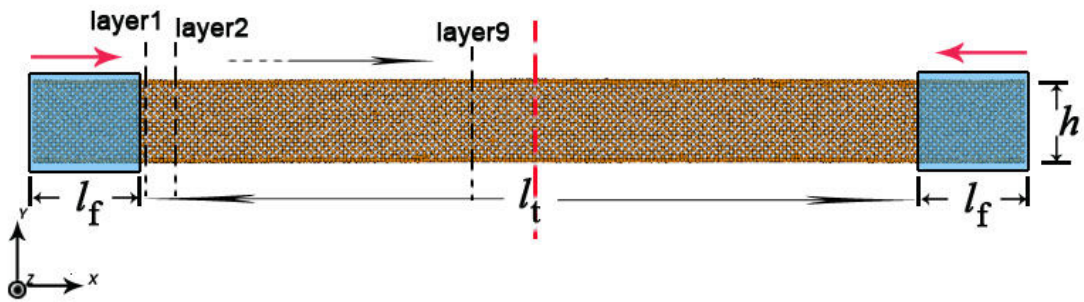


Figure 3.19 Schematic diagram of the simulation model (Jiang et al. 2012, Jiang 2013).

The geometry of the single crystal Cu nanobar (target) is characterized by the length  $l_t$  and height  $h$ , i.e.,  $l_t \times h \times h$ . Two additional regions with length  $l_f$  located at either end of the target are treated as flyers. The flyers impact the ends of the target with speed 500 m/s, as indicated by the two red arrows.

All the results to be discussed in this sub-section are based on the same MD simulation procedure as described in Section 3.2.1, except the difference in the boundary treatment. Simulations of the nanobars were performed without using periodic boundary conditions. Systems corresponding to quasi-infinite slabs with primary simulation cell sizes  $100a \times 10a \times 10a$  and  $100a \times 40a \times 40a$  and with the periodic boundaries applied along the  $y$ - and  $z$ -axis, respectively, were also investigated, to assess directly the effects of free surfaces. In all cases the average lattice parameter  $a = 0.363$  nm obtained from a 3-D

periodic isothermal-isobaric (NPT) simulation of duration 0.5 ns performed for a crystal containing 2048 atoms at  $T = 298$  K and zero pressure was employed to build the sample/flyer assemblies. The starting configurations for the nanobars were equilibrated for 100 ps at  $T = 298$  K using the Nosé-Hoover thermostat (Nosé 1984, Hoover 1985). This step was performed to relieve the stresses resulting from the introduction of free surfaces and to achieve a thermal distribution of atomic velocities; analogous simulations were performed in the NVT ensemble for the two quasi-infinite systems after adding a large gap along the shock direction to prevent interactions between the two ends of the flyer/target assemblies. Next, the impact velocity  $\pm 500$  m/s is added to the  $x$ -component of the thermal velocities of the atoms comprising the flyers after which the impact process is simulated in the  $NVE$  ensemble for 30 ps (corresponding to approximately  $5\times$  the time required for the shocks to propagate from the impact surfaces to the center of the target).

Atomic layers oriented perpendicular to  $[100]$  in the unshocked material are used to facilitate trajectory analysis. Nine Lagrangian regions evenly distributed from an initial distance  $0.5a$  (layer 1) to  $40.5a$  (layer 9) from the impact surface are used to monitor the shock front propagation. A static, Lagrangian-like assignment of atoms to a given layer is used; each layer is one unit cell thick perpendicular to the shock direction and contained 662 atoms, 2522 atoms, and 9842 atoms for the cases of nanobar edge length  $10a$ ,  $20a$ , and  $40a$ , respectively. Due to the symmetry of the counter propagating elastic precursor shock waves, equivalent layers  $n$  and  $n'$  are defined for the two halves of the target and the results for those symmetry-equivalent layer pairs averaged to improve the precision of simulation results; hereafter the results for a given layer-pair  $(n, n')$  are discussed in terms

of a single layer  $n$ . The outermost layer, initially centered at the distance  $a/2$  from the impact surface, is defined to be the first layer, with successive layers separated by  $5a$  along the shock direction and extending to the distance  $40.5a$  into the sample to yield nine layers for each case studied. The instantaneous position of the shock front, and hence the shock velocity, is determined from the time histories of the center-of-mass positions of the layers. Additional details concerning how the shock front is tracked can be found in the associated references (Siavosh-Haghighi et al. 2009, He, Sewell, and Thompson 2011)

The center-of-mass displacements for each layer along the shock direction are plotted as functions of time in Fig. 3.20. Panels (a), (b), and (c) correspond to the nanobars with  $10a \times 10a$ ,  $20a \times 20a$ , and  $40a \times 40a$  cross sections, respectively. As expected, the displacement of each layer increases rapidly as the shock wave passes over it. The maximum displacement of layer 1 (the layer closest to the impact surface) for the smallest nanobar (Fig. 3.20(a)) is much larger than that for the nanobars with larger cross sections. For the larger nanobars (Figs. 3.20 (b) and (c)), the displacement of each layer becomes approximately constant at about 15 ps after impact and even begins to decrease somewhat in the case of the  $40a \times 40a$  cross-section nanobar for time greater than  $\sim 20$  ps (corresponding to partial, albeit small, recovery of the sample). The results in Fig. 3.20 demonstrates that, for the  $500 \text{ m}\cdot\text{s}^{-1}$  impact velocity applied to the Cu system, the smaller the cross section of the nanobar the larger the shock-induced compressive strain and the greater the extent of plastic deformation. This might be due to the larger ratio of the surface area to the volume as the cross section is decreased. In general, atoms in a crystal oscillate about their equilibrium positions in the lattice. Atomic-scale defects can be

nucleated if an atom gains enough energy, for example by application of an external load, to be displaced significantly from the original lattice site. Normally the activation barrier for heterogeneous defect nucleation (as would occur at a free surface) is lower than that for homogeneous defect nucleation (as would occur inside a material sample with no free surfaces or pre-existing defects). Thus, the nanobars with smaller cross section will contain greater relative numbers of surface atoms that can be activated by the shock waves. The smaller the cross-sectional area, the more readily the nanobar undergoes shock-induced plastic deformation. The peak stress near the impact surface in the  $10a \times 10a$  nanobar is approximately 15 GPa (not shown, but calculated from layer 1). Because this stress exceeds the strength limit (Jiang et al. 2010, Liu, Zhao, and Wang 2009) of the  $10a \times 10a$  nanobar, it is not surprising that extensive plastic deformation occurs in this case.

The effective shock wave speeds can be estimated from the plots of layer displacement vs. time based on the locus of times at which the individual layers undergo initial acceleration due to shock passage. For the  $10a \times 10a$  nanobar approximately 5.0 ps is required for commencement of the initial acceleration of layer 9, initially located at the distance  $40.5a$  from the impact surface (see the inset to Fig. 3.20(a)). By contrast, for the  $20a \times 20a$  and  $40a \times 40a$  nanobars this initial acceleration in layer 9 occurs approximately 4.0 ps and 3.2 ps following impact, respectively. Thus, the associated effective wave speeds for the  $10a \times 10a$ ,  $20a \times 20a$ , and  $40a \times 40a$  nanobars are  $\sim 8$   $a/ps$ ,  $\sim 10$   $a/ps$ , and  $\sim 12.5$   $a/ps$ , respectively; increasing nanobar cross-sectional area leads to increasing effective shock wave speed. This is in good agreement with the results reported for nanowires subjected to high strain rate tensile loading (Wu, Ma, and Xia 2005). A

possible explanation can be derived from the wave speed formula for idealized one-dimensional wave propagation, for which the wave speed is proportional to the square root of the Young's modulus under the assumption of fixed material density. Indeed, multiple data show that the Young's modulus of a nanowire increases with increasing cross-sectional area (Branicio and Rino 2000, Koh and Lee 2006, Wu, Ma, and Xia 2005), which would be expected to lead to increased wave propagation speed in the material. Eliminating the transverse free surfaces from the systems with the use of quasi-infinite slabs (*i.e.*, systems with periodic boundary conditions applied along directions transverse to the shock propagation direction but not parallel to it) has further confirmed the findings and interpretations discussed above (Jiang et al. 2012). The wave propagation speed increases with increasing cross-sectional area with free surfaces, and eventually approaches the value obtained for quasi-infinite slab samples, which is similar to the macroscopic value.

In addition to the size-dependence of wave speed due the existence of free surfaces, extensive plasticity that occurs across the entire lengths of the nanobars can be another reason. The size effect on the deformation pattern in the nanobars is illustrated in Fig. 3.21. For the smallest nanobar ( $10a \times 10a$  cross-sectional area), the material fully reorients from  $\langle 100 \rangle / \{100\}$  to  $\langle 110 \rangle / \{111\}$  with few stacking faults and twins. Nanobars with  $20a \times 20a$  cross-sectional area do not reorient completely; the local crystal deformation is mediated mainly by partial dislocations activity leading to predominantly non-intersecting stacking faults and twins. Nanobars with  $40a \times 40a$  cross-sectional area exhibit similar behavior but show greater propensity for intersecting stacking faults.

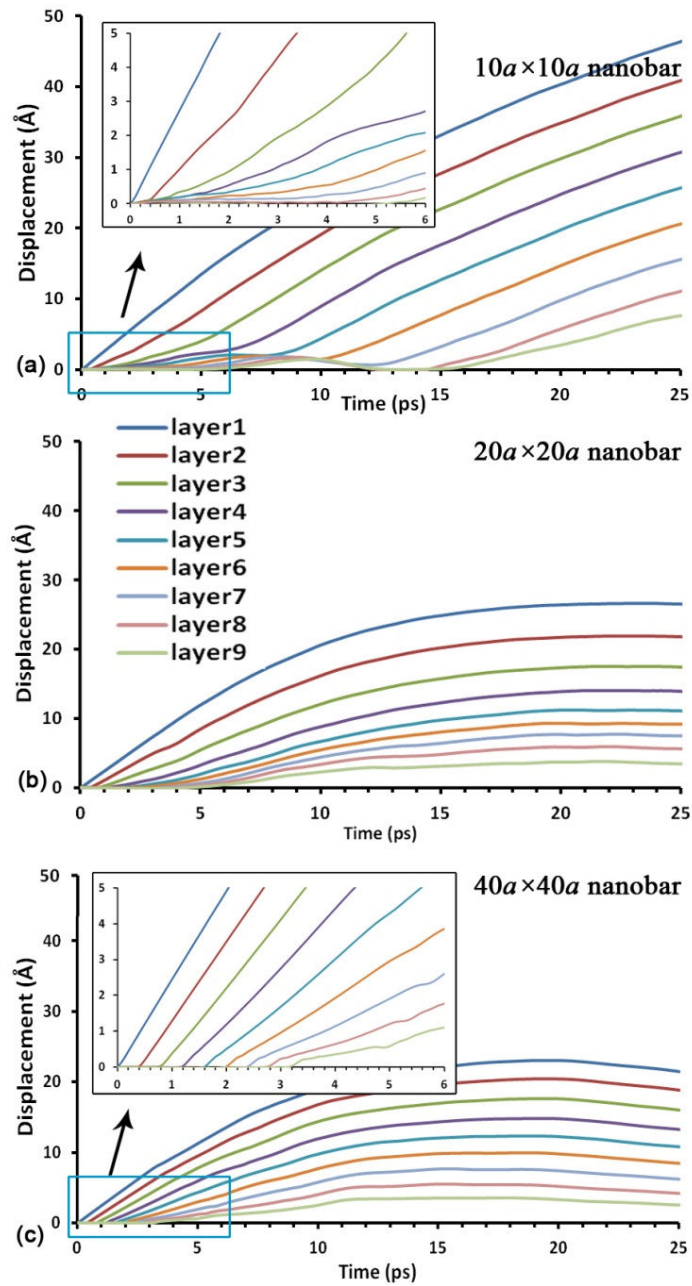


Figure 3.20 Center-of-mass displacement for each layer along the shock direction as a function of time during shock propagation for the nanobars with (a)  $10a \times 10a$ , (b)  $20a \times 20a$ , and (c)  $40a \times 40a$  cross sections. The insets in frames in (a) and (c) are expanded scales to more clearly illustrate the results at short post-impact times (Jiang et al. 2012, Jiang, Shen, et al. 2013, Jiang 2013).

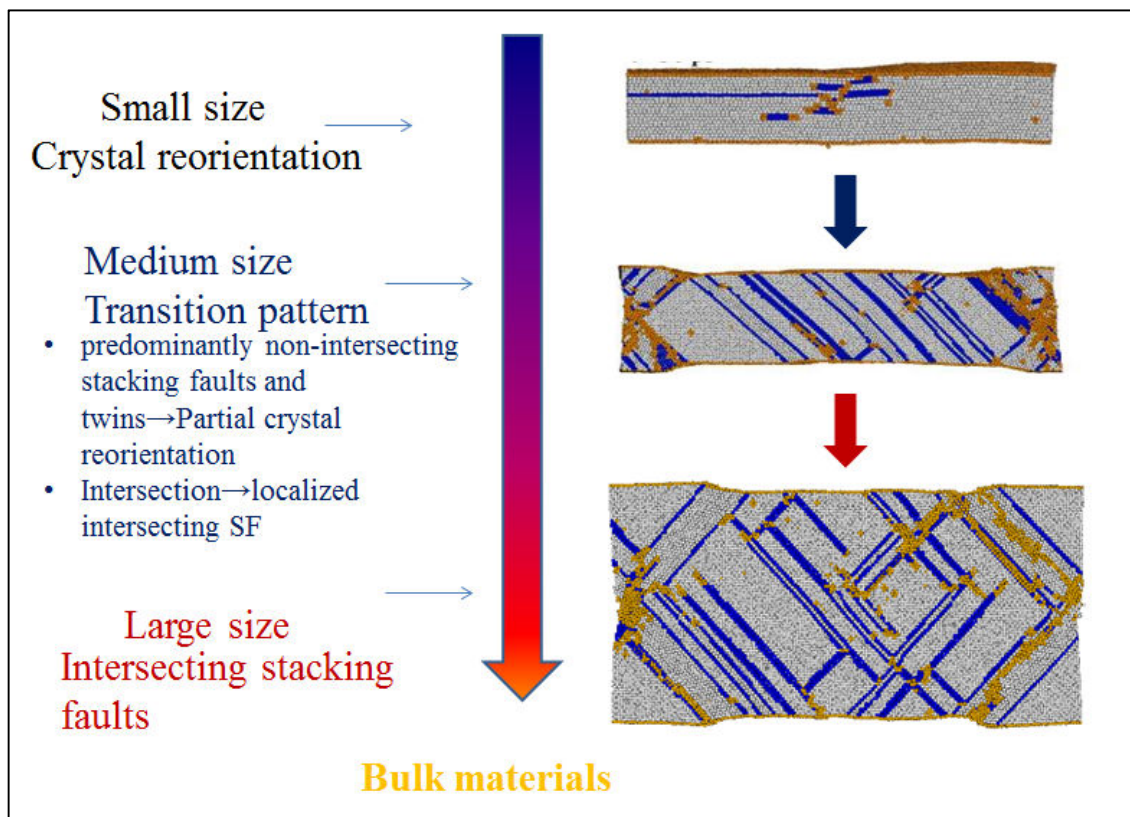


Figure 3.21 Size effect on the deformation pattern of nanostructure.

### 3.4 Summary

The results from our recent research on the atomistic modeling and simulation of metallic nanostructures subject to various loading conditions have been presented in this chapter, which have revealed interesting phenomena that are not expected to exist at the macroscopic scale. The major results in this chapter are summarized as follows:

First, metallic nanowires have been simulated in this chapter by using MD simulations and local crystal structure analysis. The general deformation mechanism of these low-dimensional nanostructures was studied. Local crystal structure analysis showed that the lattice slip can occur initially at the places adjacent to free surfaces,

which results in the emission of partial dislocations. Because there are a large portion of atoms locating at the surfaces, surface-related activities play a dominant role in determining the mechanical properties of the nanowire.

Second, the simulation results have shown that the crystal plasticity and the deformation patterns of the nanostructures depend not only on the sample geometry (shape and size), but also on the loading conditions and stress states (Jiang et al. 2010, Jiang, Chen, et al. 2013, Jiang, Zhang, et al. 2013). Some special nanostructures can be formed during the deformation process. By performing MD simulations on metallic FTNWs, the formation of quasi-icosahedral structures under dynamic tension loading was observed. These structures composed of multiple-twins are commonly found in metals with low SFE (e.g. Au, Ag and Cu), while have not been observed in those with very high one (e.g. Al), indicating that the SFE plays an important role in the formation of these multiple-twinned structures. Unlike the icosahedral structure found in the nanoclusters, the quasi-icosahedral structure reported here consists of a twisted original fivefold-twinned axis and ten secondary FDTs, with five preexisting prismatic and fifteen tetrahedral subunits joined together. Thus, this unique multiple-twinned structure divides the fracture surface of the nanowire into fifteen small triangular facets. Formation of these structures is found to be independent of the nanowire cross-sectional shapes, and also appears to be insensitive to different strain rates. The intrinsic fivefold axis serves as the framework to facilitate the successive twinning process during plastic deformation, which finally develops a hemisphere-like “cap” of the nanowire after the fracture of the necking occurs.

Finally, two types of representative problems in impact mechanics have been considered in this chapter. The transverse impact response (beam–beam impact) corresponds to the plate impact (uniaxial strain state), and the longitudinal one (particle–rod–particle) to the uniaxial stress state. In this chapter, the size-dependent impact responses of a certain kind of metal nanostructure – fcc single crystals without any internal imperfection and grain boundary were described. The size effect on the transverse impact response appears to be related to the distance between sample corners (sources of stress or strain concentration), while the size effect on the longitudinal impact response relies on the ratio of free surface to volume and can induce a significant change in the deformation pattern in the nanorods.

Based on the fundamental understanding of mechanical response deformation mechanism at atomic-scale, the mechanical properties of these materials will serve as the initial input data and be considered as references for the multi-scale simulations.

# CHAPTER 4. ATOMISTIC MODELING AND SIMULATION OF NANOPARTICLE INCLUSIONS IN FLUID UNDER HIGH PRESSURE

## 4.1 Introductory Remarks

At the nanoscale, the size effect on the discrete structural responses to extreme loading conditions is a hot research topic of current interest due to the potential benefits in modern engineering applications such as MEMS/NEMS devices and nanothermite composites. As reviewed for the responses of homogeneous nanostructures to high pressure (San-Miguel 2006), the first benefit of using high pressure is the potential for obtaining new material phases of nanostructural morphologies (San-Miguel 2006, Davidson et al. 2011). In addition to the transverse and longitudinal impact conditions shown in the last chapter, the nanostructural responses to hydrodynamic loading might provide alternative insight into the size effect because the free surfaces are compressed under high pressure. However, there is a lack of understanding about the nanostructural responses to hydrodynamic loading. Especially, the size effect on the hydrodynamic responses is unknown. Hence, this chapter will be focused on the hydrodynamic response of metal nanostructures, which would advance our knowledge in multi-scale structural responses to extreme loading conditions.

When investigating the responses of liquid and solid krypton (Kr) to high confining pressure, it appears from the available experimental data that the elastic

anisotropy decreases with increasing pressure due to reduction of free volume. However, the effects of loading rate and impurity inclusions on the anisotropy are still open issues. In addition, experiments under non-hydrodynamic loading have demonstrated that sample dimensions influence strength and crystal plasticity (Shimizu, Saitoh, and Sasaki 1998). Our recent work (Chen, Jiang, et al. 2012) shown in Chapter 3 concerning the size effect on plate impact responses of Cu nanostructures has illustrated that the pressure-particle velocity ( $P-U_p$ ) relationship depends on sample dimensions, which is qualitatively consistent with the experimental observation under quasi-static loading (Uchic et al. 2004). In this chapter, MD simulations are used to explore the hydrodynamic response and crystallization properties at the nanoscale of initially fluid phase krypton subjected to high dynamic pressure loading. Simulations were performed for three different rates of pressure increase, with or without a Cu inclusion in the fluid, and for three different sizes of cubic or spherical inclusions when the inclusion is present.

As illustrated in Fig. 4.4 for the  $10a$  inclusion, the stress state in Cu remains hydrodynamic (all three normal stress components are the same) when the confining pressure is increased at the highest rates studied (20 MPa/ps and 10 MPa/ps in panels (a) and (b), respectively). By contrast, the stress state starts to deviate from the hydrodynamic one starting at  $t \approx 2$  ns when the loading rate is 1 MPa/ps (panel (c)). This implies that there has been a structural transition in the Kr. Similar results were obtained for the  $5a$  and  $20a$  inclusions. To explore the transition pictorially, the “front half” of the system containing the  $10a$  Cu inclusion was removed to expose the cross-section of CNA-classified atoms (as shown in Fig. 4.5).

## 4.2 Computational Set-up for the Particle-Fluid Model

The MD simulations were performed using the LAMMPS code (Plimpton 1995). The EAM force field (Daw and Baskes 1984, Mishin et al. 2001) was used to describe the interatomic interactions among Cu atoms. Interactions between Kr atoms and between Kr and Cu atoms were modeled using the Lennard–Jones 12–6 potential with parameters  $\sigma = 0.3633$  nm and  $\varepsilon/k_B = 176$  K as well as the cutoff distance  $r_c = 2.5\sigma$  for both cases (Sofos, Karakasidis, and Liakopoulos 2009). The velocity-Verlet integrator was used to integrate the equations of motion with a 1.0 fs time step.

A gaseous fluid system containing 256,000 Kr atoms in a cubic-shaped three-dimensionally (3-D) periodic simulation cell was equilibrated for 200 ps at 1 atm and 298 K by using the NPT ensemble with independent barostats for all three normal stress components. The values for the thermostat and barostat coupling parameters were 100 fs and 200 fs, respectively. The fluid was prepared in a primary cell of initial size  $\sim 218 \times 218 \times 218$  nm<sup>3</sup>.

As shown in Fig. 4.1, wherein the expanded view to the right shows the atomic detail, a cubic (or spherical) Cu crystal with a certain size was then embedded into the geometric center of the simulation cell containing the Kr, and the system equilibrated for another 200 ps at 298 K using the NVT ensemble. Next, the system pressure was increased at a prescribed constant rate using the NPT ensemble until a target pressure was reached, after which the system was equilibrated at that constant pressure for 200 ps to obtain the volume averaged over the last 100 ps at that pressure and 298 K. Except for where otherwise noted, the Cu inclusions are of cubic shape. Copper inclusions with edge lengths  $5a$ ,  $10a$ , and  $20a$  (where  $a = 3.615$  Å is the lattice parameter of Cu) were

embedded into the fluid to study the size effect under hydrodynamic loading. The results were compared to those for bulk Cu obtained from 3-D periodic simulations with a  $10a \times 10a \times 10a$  primary simulation cell.

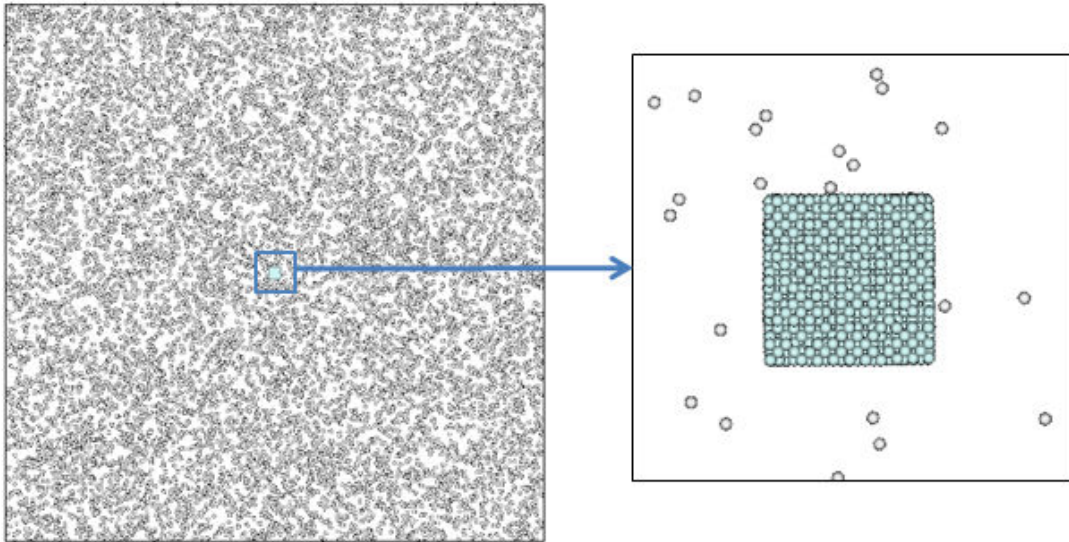


Figure 4.1 The initial configuration of a representative Kr-Cu system at 298 K and 1 atm, which is used as the starting thermodynamic state for the hydrodynamic compression simulations discussed in connection with Figs. 4.2-4.6.

### 4.3 Pressure-Volume Relationship

Based on the Cu-Kr solid- fluid model shown in Section 4.2, the Pressure-Volume (P-V) relationship is calculated first. After the Cu particles with edge lengths of  $10a$  and  $20a$  were embedded into Kr system and equilibrated at certain pressure (see the details in Section 4.2), the volume changes ( $V/V_0$ ) of Cu particles were examined.  $V_0$  is the initial volume of the Cu inclusion that is obtained at 1 atm and 298 K.  $V$  is the current volume

of the Cu inclusion at current pressure level. The volumes of the sample were estimated by calculating the products of the absolute lengths in three directions of the cubic sample.

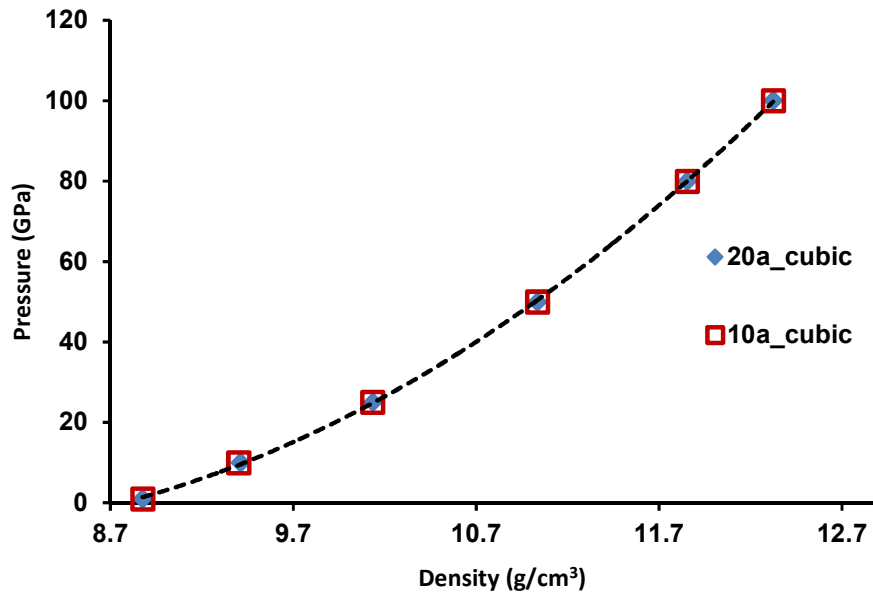


Figure 4.2 Pressure-density curves of periodic cubic Cu samples with different cell sizes.

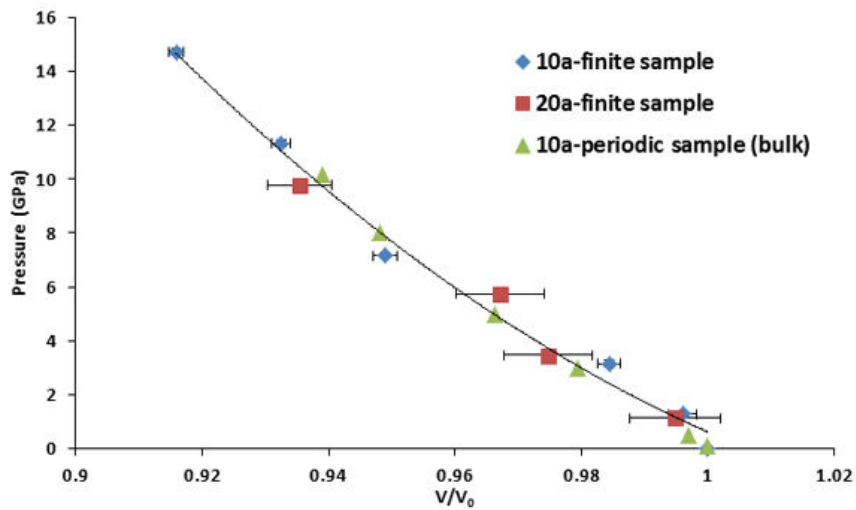


Figure 4.3 Pressure-volume curves for both finite-size cubic and bulk (3-D periodic) Cu crystals.

For comparison, periodic samples of Cu with different cell sizes were also simulated at different pressure levels. As can be seen from Fig. 4.2, the pressure-density curves of the periodic cubic cells with different cell sizes coincide with each other. This anticipated result is reasonable because the bulk modulus of the same material should be independent of the periodical cell size. Hence, only the periodic sample with the cell length of  $10a$  was chosen as a reference to the hereafter simulations of Cu inclusions.

The pressure-volume compression ratio curves in Fig. 4.3 show that the results for the finite-size inclusions are close to those for bulk Cu (for which the periodical boundary conditions are used along all the directions without embedding the Cu crystal into Kr atoms), and there is no obvious size effect on the Cu P-V equation of state as the size of the Cu inclusion edge length is increased from  $10a$  to  $20a$ . Because the size effect depends mainly on the ratio of free surface to volume (Chen, Jiang, et al. 2012), the hydrodynamic loading constrains the free surfaces so that the size effect disappears.

#### **4.4 Nanostructural Transition**

For the pressure loading rates, system size, and time scale studied here (0.5-10.0 ns during NPT simulations, depending on  $dP/dt$ ), pure Kr transforms from a fluid to a nanocrystalline solid, the statistical properties of which depend on the rate of pressure increase as shown later. Some simulations were repeated using different random number seeds, and found to yield the similar results. CNA (Faken and Jónsson 1994, Tsuzuki, Branicio, and Rino 2007) was used to characterize the local crystal structure in the solids. Individual atoms are color-coded at a given instant of time based on their instantaneous local environment determined from the CNA. In the following, fcc atoms are shown as

hcp atoms are red, and body-centered-cubic (bcc) atoms are blue. The remaining atoms are classified as disordered, and shown as white.

The results in Fig. 4.5 are for the times when the instantaneous pressure in the Kr reaches  $P = 5$  GPa at the respective pressure loading rates. Panels (a) and (b) are for the case of the  $10a$  Cu inclusion, and panels (c) and (d) for the case of no inclusion. Panels (a) and (c) are for 10 MPa/ps, and panels (b) and (d) for 1 MPa/ps. It appears from Fig. 4.5(a) that, sufficiently far from the inclusion, an approximately isotropic configuration exists for the high loading rate.

By contrast, for the low loading rate (Fig. 4.5(b)), an orthotropic structure consisting of layered hcp and fcc regions develops that extends throughout the simulation domain and results in the non-hydrodynamic stress state in the Cu inclusion even though the overall stress state in the system is hydrodynamic. Stress concentration at the edges of Cu inclusions leads to disordered Kr atoms along the diagonals at the high loading rate. These disordered regions along the diagonals disappear when the loading rate is decreased. The hard-soft crystal interaction under high pressure can be viewed as the “indentation” of (mechanically hard) Cu into (mechanically soft) Kr. The high loading rate would yield the high modulus of solid Kr so that the volume space for large variations of the anisotropy in Kr is reduced and the deformed configuration becomes isotropic as shown in experiments (Shimizu, Saitoh, and Sasaki 1998).

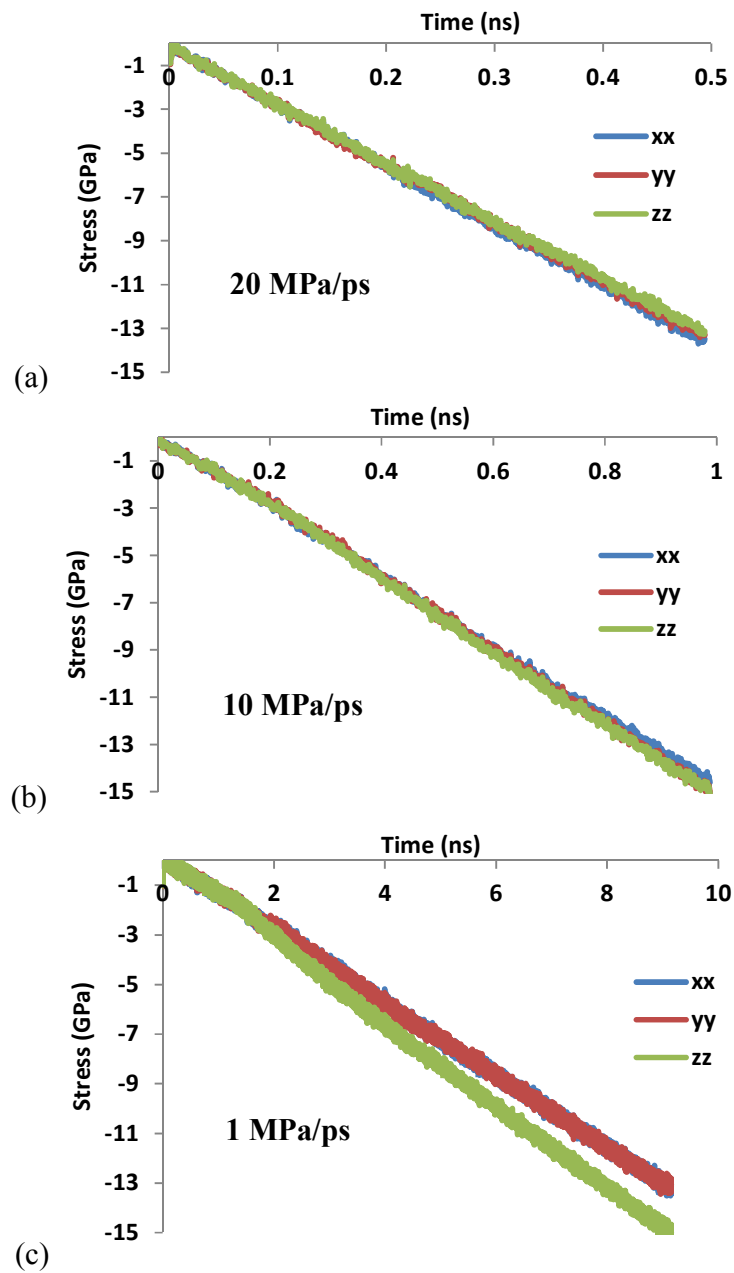


Figure 4.4 Panels (a) and (b): Atomic configurations of the Kr-Cu system at 298 K and 5 GPa for an inclusion with edge length  $10a$ . Pressure-loading rates are: (a) 10 MPa/ps and (b) 1 MPa/ps. Panels (c) and (d): As in panels (a) and (b), respectively, but with no inclusion present.

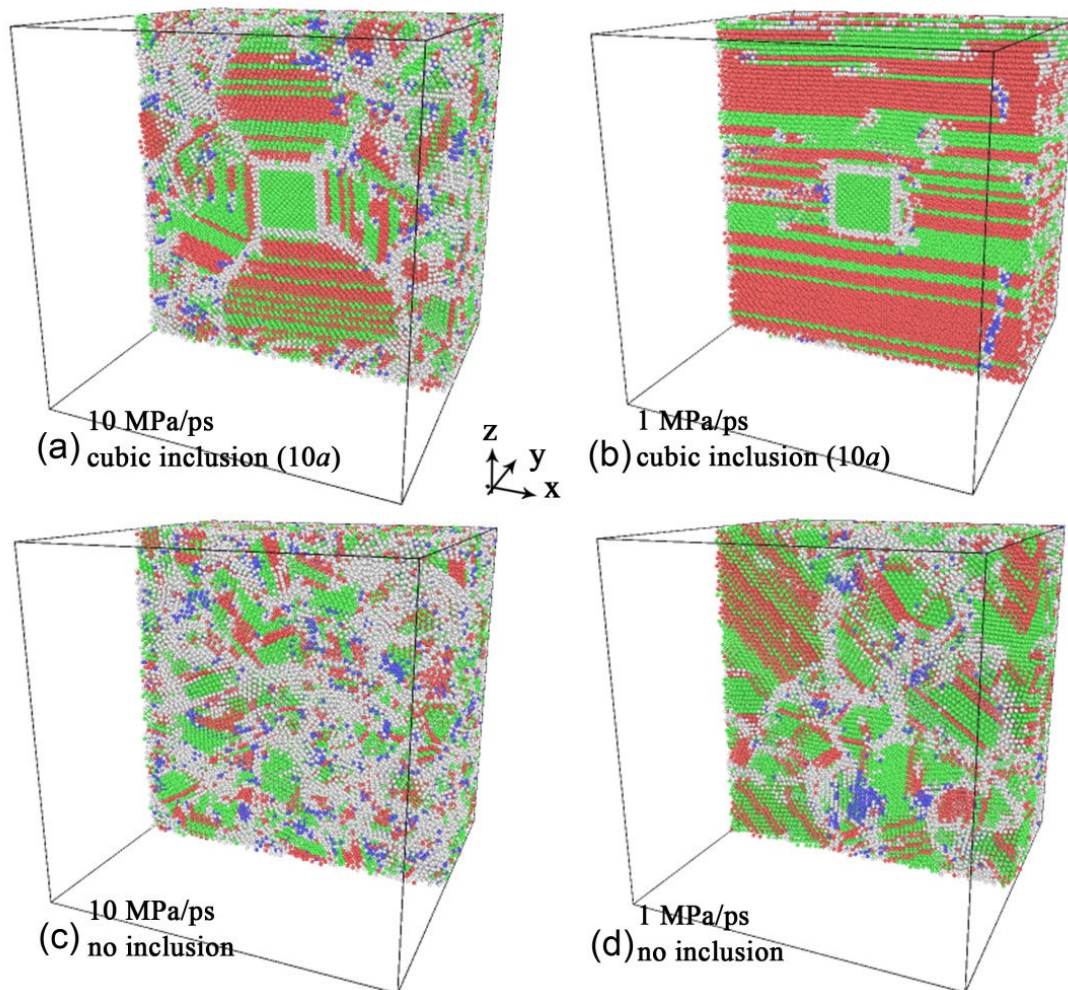


Figure 4.5. Panels (a) and (b): Atomic configurations of the Kr-Cu system at 298 K and 5 GPa for an inclusion with edge length  $10a$ . Pressure-loading rates are: (a) 10 MPa/ps and (b) 1 MPa/ps. Panels (c) and (d): As in panels (a) and (b), respectively, but with no inclusion present.

For the slower loading rate there is more time for the Kr atoms to anneal into the less-disordered layered structure whereas for the faster loading rate metastable local nanocrystalline configurations are more likely to become trapped. As shown in Figs. 4.5(c) and (d), in the absence of the Cu inclusion there is an approximately isotropic distribution of Kr nanocrystal orientations, with smaller nanocrystals and larger regions

of disordered atoms (grain boundary regions) for the case of rapid compression (panel (c)); the observation of an isotropic distribution of nanocrystalline orientations is consistent with experiments (Shimizu, Saitoh, and Sasaki 1998).

After obtained the atomic configurations shown above, one may ask a question: what are the dominant factors that affect the room-temperature pressure-induced nanocrystallization of Kr from the fluid in the presence of the Cu inclusion? As can be deduced from Figs. 4.5(a) and 4.5(b), the stress concentration around the Cu inclusion edges likely plays an important role in the nanostructural transition. To assess this hypothesis, simulations were performed for the same  $dP/dt$  values discussed in connection with Fig. 4.5, but with the cubic  $10a$  Cu inclusion replaced with a spherical one of diameter  $10a$ . As can be seen from Fig. 4.6, the presence of the spherical Cu inclusion does not result in long-range order of nanocrystal orientation in the Kr; the result is similar to what was observed in the absence of Cu (Figs. 4.5(c) and 4.5(d)). Note however the difference in grain size distribution as compared to the result where a cubic inclusion is present (Figs 4.5(a) and 4.5(b)).

To evaluate the effect of stress concentration on the nanostructural transition, Cu inclusions with different edge lengths were embedded in the Kr fluid and the systems pressurized at 1 MPa/ps. As shown in Fig. 4.7, layered structures consisting of fcc and hcp atoms form for a sufficiently large Cu inclusion. From a mechanics viewpoint, this will occur when the stress concentration level at the edge of the Cu inclusion reaches a certain value. The increase of the edge length results in the decrease of strain gradient (as also occurs in the nano-indentation process under quasi-static loading), which would reduce the hardness of the Kr away from the edge (Nix and Gao 1998).

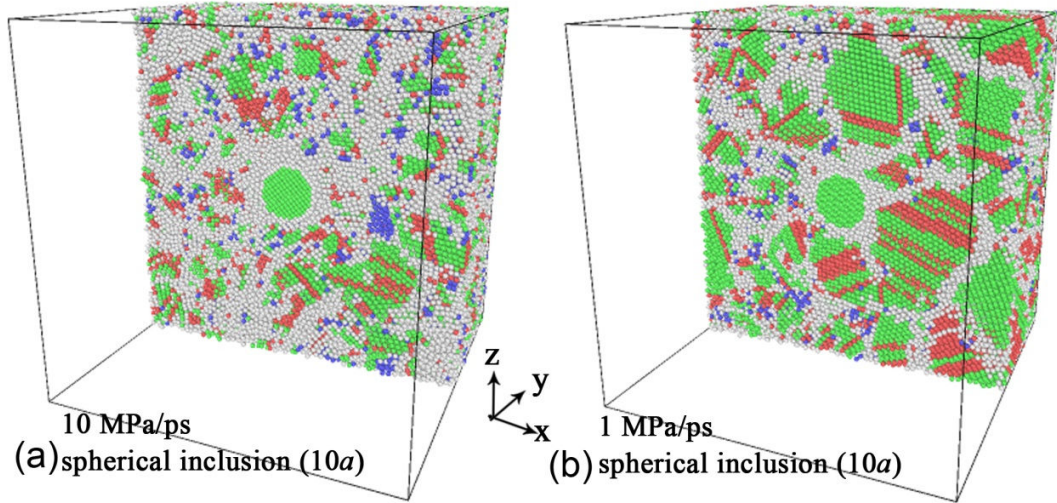


Figure 4.6. Atomic configurations of the Kr-Cu system at 298 K and 5 GPa for a spherical inclusion of diameter  $10a$ . Pressure-loading rates are: (a) 10 MPa/ps and (b) 1 MPa/ps.

Increase in the Cu inclusion size also leads to the formation of a narrower interphase (disordered region) between the Cu inclusion and the Kr nanocrystalline domains. For sufficiently long edge length, there is a transition from a nanostructure that is orthotropic over the entire domain (Fig. 4.7(b)) to one that is locally orthotropic with the hcp/fcc stacking patterns oriented normal to the Cu inclusion surfaces (Fig. 4.7(c)). Hence, at least for the size of the primary simulation cell used (initially  $\sim 218 \times 218 \times 218$  nm<sup>3</sup> when the pressure is 1 atm), the inclusion edge length affects the level of deformation anisotropy in the Kr polycrystalline domain.

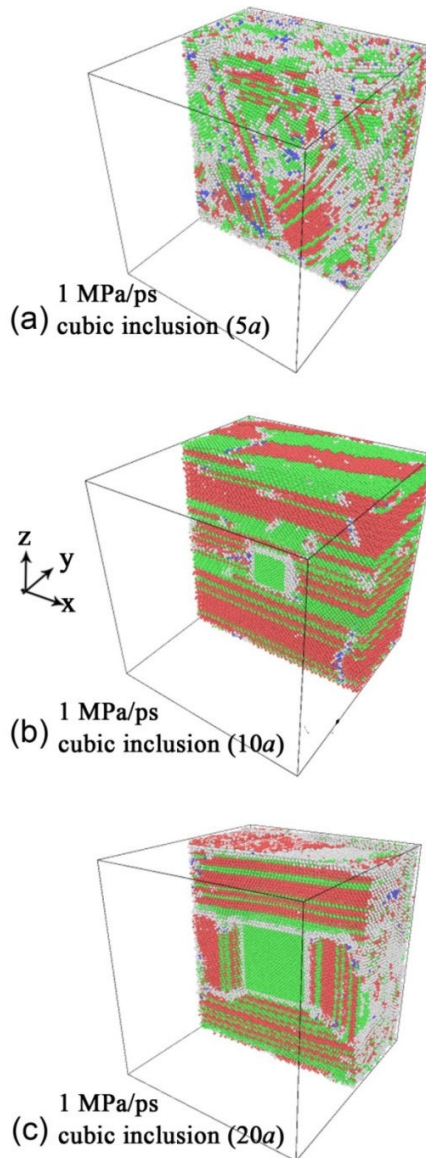


Figure 4.7 Atomic configurations of the Kr-Cu system at 298 K and 5 GPa for cubic inclusions and pressure-loading rate 1 MPa/ps. Inclusion edge lengths are: (a)  $5a$ , (b)  $10a$ , and (c)  $20a$ .

## 4.5 Summary

In this chapter, atomistic modeling and simulation of nanoparticle inclusion in the fluid have been performed. First, the P-V relations of solid Cu nanoparticles were

obtained by inserting them in the Kr gaseous fluid at various hydrostatic states. Then, the deformation evolution of the Cu-Kr system was examined under hydrodynamics loading.

From the simulation results, it is found that Kr is predicted to exhibit a rate-dependent pressure-induced nanostructural transition. The nature of the resulting nanostructure is affected by the presence, size, and shape of a hard inclusion (Cu). The pressure-volume relation for the Cu inclusion embedded in the Kr is size-insensitive under high confining pressure. For low pressure-loading rate (1 MPa/ps), the stress state in Cu changes from hydrodynamic to non-hydrodynamic; the onset of the change appears to be correlated with the formation of a long-range orthotropic hcp/fcc layered nanostructure that forms in the Kr. The factors affecting this transition appear to include the Cu inclusion geometry and interactions at the hard-soft material interface, and possibly also the primary simulation cell size. Based on the preliminary results of a parametric sensitivity study, the results reported here are robust with respect to the reasonable changes in force field parameters and pressure loading rates.

## **CHAPTER 5. MULTI-SCALE SIMULATION OF NANOSTRUCTURES UNDER DYNAMIC AND IMPACT LOADING**

### **5.1 Introductory Remarks**

As reviewed in Chapter 1 and Chapter 3, energetic composites containing metallic fuel (e.g. particles, powder) and inorganic oxidizer have become a research topic of current interest due to their high energy density, tunable energy release rate and ignition sensitivity, and benign reaction products (Rossi et al. 2007, Dreizin 2009, Apperson et al. 2007, Gan et al. 2010). While simple physical mixing leads in general to a nonhomogeneous distribution of fuel and oxidizer nanostructures (Apperson et al. 2007, Gan et al. 2010), optimal performance would require tailored structure and morphology. Toward this end, composite system designs, such as the self-assembled thermitic composites consisting of discrete CuO and Al nano-structures, have been produced (Apperson et al. 2007, Gan et al. 2010). The Al/CuO composite system has been investigated at the continuum level using an equation of state (EoS) for the reaction products, formulated under the assumption of a pressure-dependent reaction rate that is infinite for the pressure greater than some threshold value but zero otherwise, and complete neglect of nano structural features (Gan et al. 2010). However, the real combustion behavior of a nano energetic composite is affected by several important factors such as ingredient ratio, mass density, composite morphology, and the often diffusion-limited interactions among discrete nano structures of various sizes and shapes.

Obviously, inclusion of such details in a high-fidelity simulation requires the use of a suitable multi-scale method.

As discussed in Chapter 3, under impact loading, discrete zero-dimensional (particle) and one-dimensional (rod and beam) nano structures of suitable sizes will interact with each other via longitudinal (particle-to-rod or rod-to-rod), transverse (particle-to-beam or beam-to-beam), and/or mixed modes. Available experimental techniques do not enable direct, real-time observation of the nanoscale interactions under impact loading. While recent molecular dynamics simulations have demonstrated size effects on the responses of single-crystal Cu nanostructures to transverse (Chen, Jiang, et al. 2012, Chen, Jiang, and Gan 2012) and longitudinal (Jiang et al. 2012) impact loading, the complex nature of general impact modes hinders computer simulations of nanoscale impacts with atomic resolution due to the large number of particles required to simulate non-trivial geometries and associated large CPU requirements. Hence, an effective spatial discretization procedure needs to be developed to model and simulate the multi-scale interactions involved in the impact responses of nano energetic composites.

In Chapter 2, the particle-based multi-scale procedure was described, which combine a hierarchical bridge from MD to Dissipative Particle Dynamics (DPD) for nanoscale simulations with a concurrent link between DPD and the MPM for microscale simulations. In this chapter, focusing on the link between DPD and the MPM, first in Section 5.2 it is demonstrated that the dynamics of DPD particles, which interact via pairwise particle-particle force expressions, can be coarse-grained using a straightforward adaptation of the standard MPM algorithm. Using this capability, in Section 5.3 it is then demonstrated how DPD and MPM subdomains can be treated concurrently, and nearly

seamlessly, in a single simulation domain. Particular attention is devoted to the development of an effective interfacial scheme for use in the concurrent simulations. Representative examples to illustrate the proposed multi-scale simulation procedure include nanorods subject to a longitudinal tensile and impact loading, which are similar to those studied with atomistic simulations in the previous chapters.

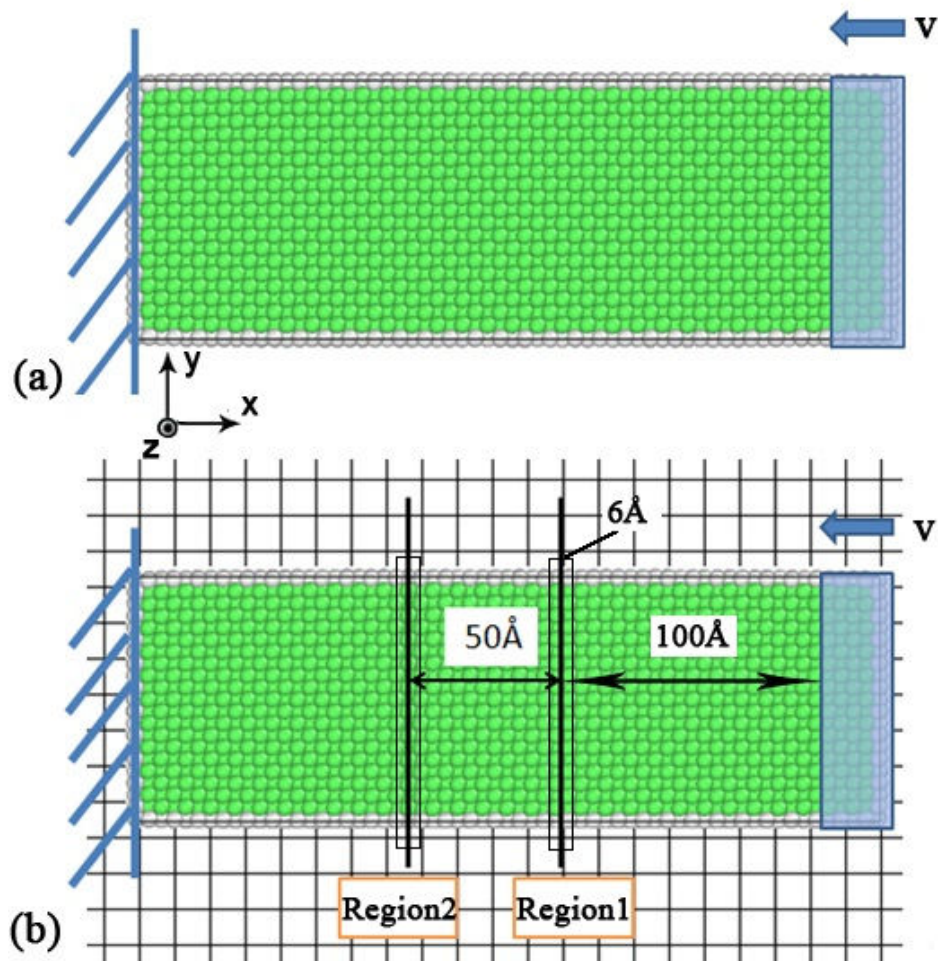


Figure 5.1 Schematic of a Cu target impacted by a Cu flyer simulated with (a) the DPD-only model and (b) the DPD/MPM-grid model.

## 5.2 Coupled DPD/MPM-Grid Model

The aim of this section is to first demonstrate that the dynamics of DPD particles, which interact via pairwise particle-particle force expressions, can be coarse-grained using a straightforward adaptation of the standard MPM algorithm. This numerical coupling method is referred to as “Coupled DPD/MPM-grid” method in this dissertation. The first demonstration of this proposed multi-scale simulation procedure is the impact of a Cu flyer onto a Cu target, followed by a tension test performed for Cu rod.

### 5.2.1 Impact Test

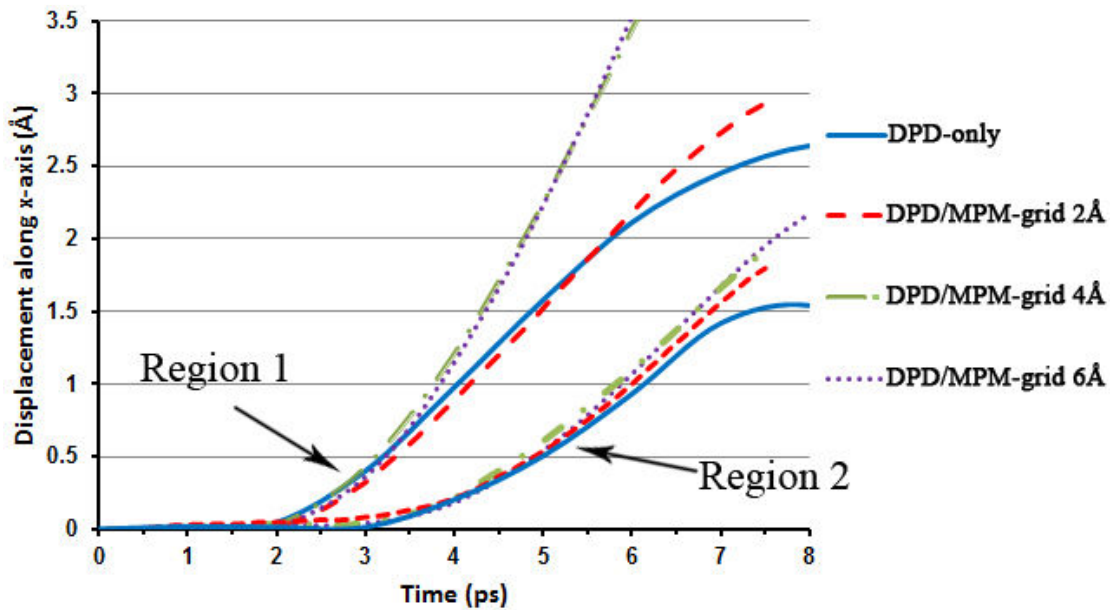


Figure 5.2 Time histories of displacements of reference region 1 and region 2 in the Cu target, simulated using the DPD-only model (solid curve) and the coupled DPD/MPM-grid model with different MPM cell edge lengths (dashed, dot-dashed, and dotted curves).

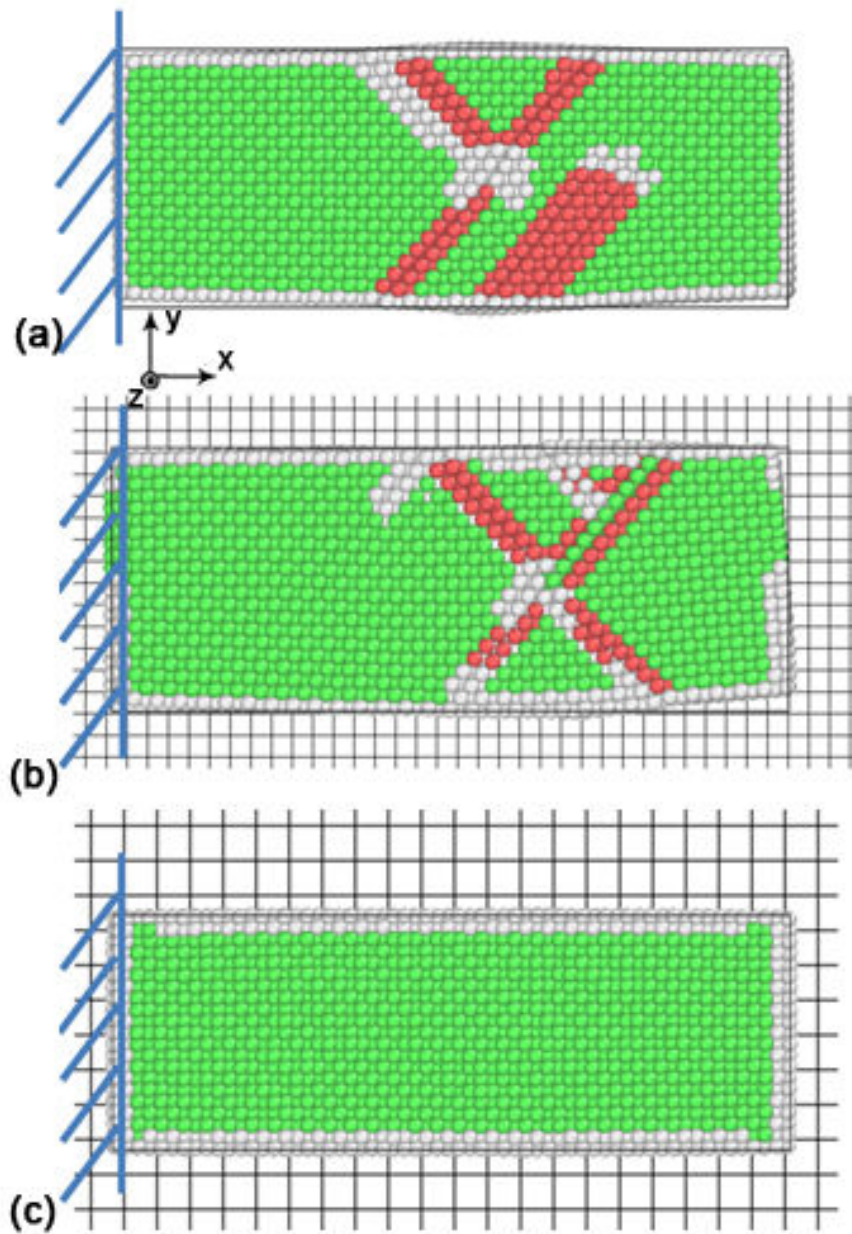


Figure 5.3 Deformed configurations of the Cu target at 10 ps after impact, simulated with (a) the DPD-only model and the DPD/MPM-grid model for MPM cell edge lengths of (b) 2 Å and (c) 8 Å.

Two simulation models, the DPD-only model are considered here, as shown in Fig. 5.1(a) and the DPD/MPM-grid model in which DPD particles are coupled to the MPM background grid as shown in Fig. 5.1(b).

The target size is  $216 \text{ \AA} \times 72.3 \text{ \AA} \times 72.3 \text{ \AA}$  ( $10a \times 10a \times 30a$ , where  $a = 7.23 \text{ \AA}$  is the coarse-grained lattice constant for face-centered-cubic (fcc) Cu crystal). The system is non-periodic in all three directions. The flyer is  $15 \text{ \AA}$  thick and is treated as a rigid body with initial velocity  $5 \text{ \AA/ps}$ . Two reference regions of thickness  $6 \text{ \AA}$  each are centered at  $100 \text{ \AA}$  and  $150 \text{ \AA}$  from the impact surface in order to estimate the longitudinal wave speed. Prior to impact, the initial DPD configuration was equilibrated for 1000 ps at 298 K by using the Berendsen thermostat (Berendsen et al. 1984). The final phase space point from the equilibration was used as the initial condition for the DPD-only model governed by Eqs. 2.4-2.7. That same phase space point was also embedded into the MPM background grid for the coupled DPD/MPM-grid simulations. CNA with the lattice constant  $a$  was used to identify the local coarse-grained crystal structures. In the results discussed about the particle configurations (i.e., Fig.5.3), fcc coarse-grained particles are shown as green, hcp particles are shown as red, and the remaining atoms (classified as disordered or surface particles) are shown as white.

As shown in Fig. 5.2, the time histories of displacements of reference regions 1 and 2 in the Cu target, simulated with the DPD/MPM-grid model for three choices of the background mesh resolution, apparently converge to that obtained from the DPD-only model for sufficiently small cell edge length during the MPM mapping and re-mapping operation. Although the displacement values obtained from the simulations with different cell sizes may be different at a given time, the wave speeds estimated by examining the

displacement history – in particular the difference in times at which particles in regions 1 and 2 first undergo significant displacements – are almost the same for the two models ( $\sim 5.32a/\text{ps}$ ,  $\sim 3846$  m/s), which indicates that DPD/MPM-grid coupling captures the essential features of elastic wave propagation. The estimated wave speed is close to the value ( $\sim 5a/\text{ps}$ , 3630 m/s) obtained in a previous all-atom MD simulation of a Cu nanobar (Jiang et al. 2012). Thus, the elastic wave speed is not strongly affected by the coarse-graining process.

By contrast, as can be seen in Fig. 5.3, the MPM mapping and re-mapping operation leads to coarsening of the detailed features of the deformation, as characterized using CNA, compared to the DPD-only result. The DPD-only result is shown in Fig. 5.3(a) and serves as a baseline. Corresponding results for the DPD/MPM-grid model are shown in Figs. 5.3(b) and 5.3(c) for grid edge lengths 2 Å and 8 Å, respectively. The DPD/MPM-grid result for the 2 Å grid is similar, though by no means identical, to the DPD-only result. By contrast, for the 8 Å grid there is no sign of local structural evolution. This is not surprising as the mapping/remapping is effectively a coarse-graining procedure and thus increasing loss of structural detail is expected as the spatial resolution is decreased.

### 5.2.2 Tension Test

In this sub-section, a Cu rod under dynamic tensile loading is considered using the DPD-only and DPD/MPM-grid models, as illustrated in Fig. 5.4. The rod has the dimension of  $216 \text{ Å} \times 72.3 \text{ Å} \times 72.3 \text{ Å}$ . The two ends, each of thickness 15 Å, are treated as rigid bodies with a constant velocity of  $2.169 \text{ Å /ps}$  applied in opposite directions. The

loading procedure is similar to that adopted in our previous MD simulations (Jiang et al. 2010, Jiang, Shen, et al. 2013) shown in Chapter 3.

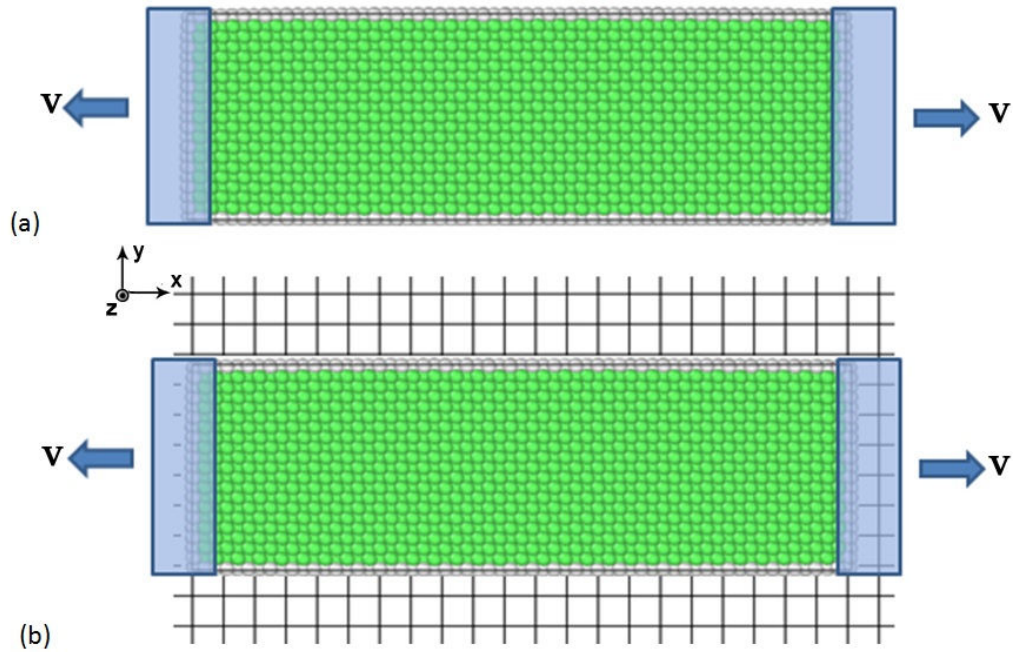


Figure 5.4 Schematic of a Cu rod subjected to tensile loading at both ends, with (a) the DPD-only model and (b) the DPD/MPM-grid model.

Figure 5.5 contains plots of the stress-strain relations of the Cu rod under tensile loading. As can be seen there, the elastic responses for the DPD-only model and the coupled DPD/MPM-grid model are generally consistent. The initial slope of the stress-strain curve is quite similar, which implies that, for sufficiently small MPM grid edge length, the elastic modulus is independent of the spatial resolution of the MPM background grid; and, therefore, the elastic wave speed is not affected by the coupling between DPD and the MPM background grid, a conclusion that was reached independently in connection with Fig. 5.2. Moreover, it can be seen that as the resolution of the grid is increased the peak stress approaches the value predicted by the DPD-only

model, which is consistent with the convergence study of displacement histories discussed in connection with Figs. 5.2 and 5.3.

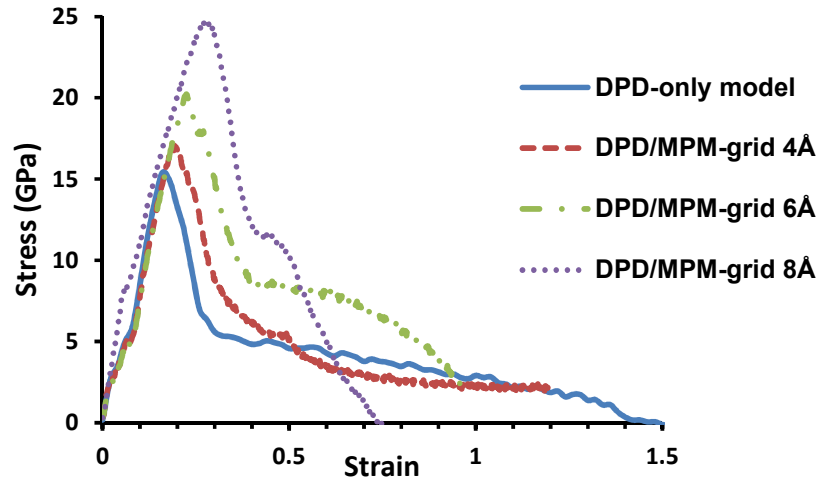


Figure 5.5 Stress-strain relations for the Cu rod under tensile loading at strain rate 0.02/ps, simulated using the DPD-only model (solid curve) and coupled DPD/MPM-grid model for different MPM cell edge lengths (dashed, dot-dashed, and dotted curves).

Figure 5.6 shows the curve fitting of stress-strain relationship of the Cu rod under tension. Since the slopes of the curves in Fig. 5.5 are close to each other for the DPD-only model and DPD/MPM-grid models with different cell size length of 4 Å and 6 Å. The curve obtained from DPD-only model is used as a baseline here to calculate Young's modulus for the rod. The estimated Young's modulus in Fig. 5.6 is 87.186 GPa, which is very close to the one (85.11 GPa at 300 K) obtained with all-atom MD simulation, as compared to Table 3.1. Compared by the results of MD simulations at the atomic-scale, it indicates that both the mesoscale DPD-only model and coupled DPD/MPM-grid models are able to predict reasonable elastic properties of the material.

Thus, the elastic modulus of 87.186 GPa for Cu as an initial input used for the von-Mises constitutive law of the particles in MPM regions that will be shown later in this chapter.

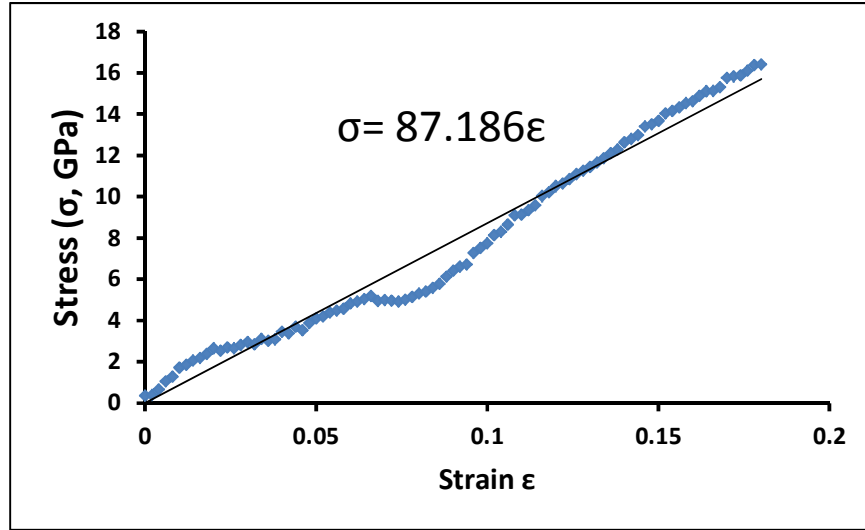


Figure 5.6 Linear fitting of stress-strain ( $\sigma$ - $\epsilon$ ) curve for the Cu rod under tension with DPD-only model.

It should be noted that for the DPD force expression used here (Gan et al. 2014), the values of the peak stress predicted by both the DPD-only model and the DPD/MPM-grid model are higher than that obtained from all-atom MD simulations (Jiang et al. 2010, Jiang, Shen, et al. 2013) shown in Chapter 3. This may be due to the fact that only the pressure-density relations from the DPD and all-atom MD systems were used in parameterizing the DPD force expression. Further work is required to improve the DPD force expression, for example, including additional information such as the stacking fault energy and surface energy in the DPD parameterization.

### 5.3 Concurrent DPD/MPM Model

Having demonstrated the consistency between DPD-only and coupled DPD/MPM-grid models, concurrent model wherein both DPD and MPM particles exist in a single computational domain (the DPD/MPM model) is tested in this section.

#### 5.3.1 Impact Test

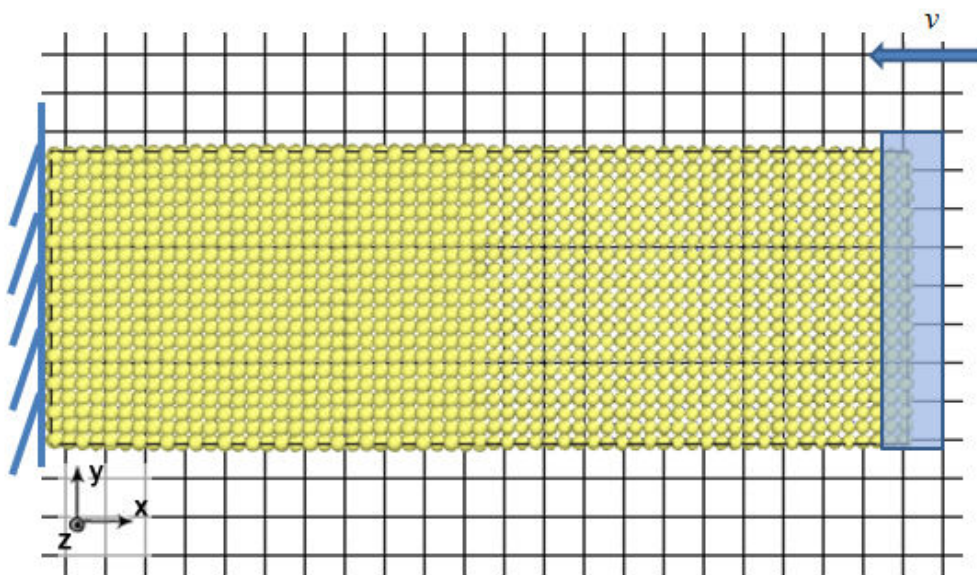


Figure 5.7 Schematic of a Cu target impacted by a Cu flyer, simulated using the concurrent DPD/MPM model. The physical situation is the same as in depicted Fig. 5.1 (see Section 5.2.1) except that in the present case the right half of the target (and the flyer) consists of DPD particles and the left half consists of MPM particles. The MPM particles are displayed with an artificially increased diameter for clarity of visualization.

As an initial validation case, elastic wave propagation across the interface between DPD and MPM subdomains are investigated, as illustrated in Fig. 5.7. The

flyer/target scenario studied is the same as discussed in Section 5.2.1 (see Fig. 5.1) except that here the left and right halves of the sample consist of MPM and DPD particles, respectively. Both particle types are the same size; the MPM particles in Fig. 5.7 are artificially increased in size for ease of visualization.

The dynamic response of the rod was first simulated separately with and without the interface treatment that was proposed in Chapter 2. As can be seen in Fig. 5.8, without the interface treatment, the particles in the interface region between the DPD and MPM regions have mismatched displacements and deformation. Hence, the interface region shows discontinuity and later collapses when the impact wave passes through.

By contrast, the rod can act as a whole structure subject to external impact with the use of interface treatment. As can be seen in the second panel of Fig. 5.8, there is no evident discontinuity at the interface of the DPD and MPM regions. Therefore, it is shown that the particles can remain in a perfect crystal lattice structure within the elastic regime if the external impact is not too strong.

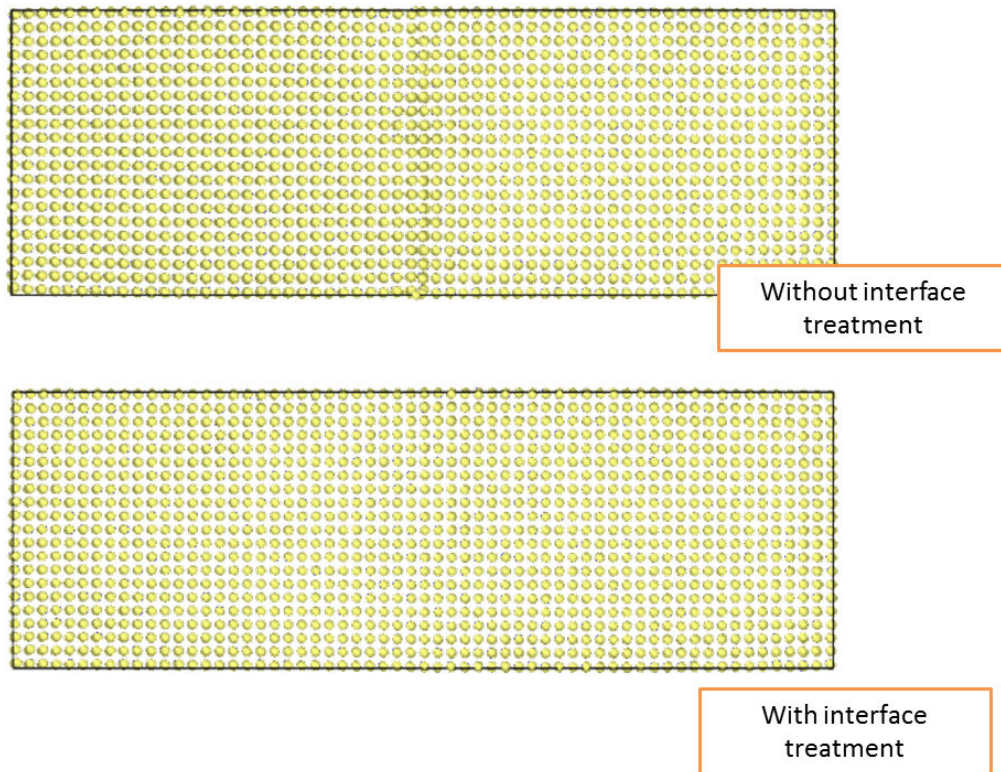


Figure 5.8 Configurations of the Cu rod subject to impact simulated with and without the interface treatment. The DPD/MPM interface is in the middle of the rod.

Figure 5.9 shows the displacement profiles for the concurrent DPD/MPM model at different times. Although there is some apparent effect of the coupling at the midpoint of the target at the shortest time shown, the wave propagates essentially smoothly through the interface between MPM and DPD regions. In addition, the elastic wave speed ( $\sim 6a/\text{ps}$ ,  $\sim 4338 \text{ m/s}$ ) estimated in this case is in a good agreement (at the same order) with those obtained in Section 5.2, and those from all-atoms MD simulations (Jiang et al. 2012). Note this value is much closer to the one obtained from the largest nanorod and “infinite-length” periodic samples ( $\sim 6.25a/\text{ps}$ ,  $\sim 4537 \text{ m/s}$ ) with MD simulation (Jiang et al. 2012). That the agreement is better for the case of large-cross-section nanobars or

periodic samples is not surprising because the MPM description is based on a constitutive model that does not include the effects of the free surfaces that significantly affect wave propagation in the smaller nanobars. Additional work would be required to incorporate such free-surface effects into the MPM constitutive description for the kinds of nanoscale structures studied here.

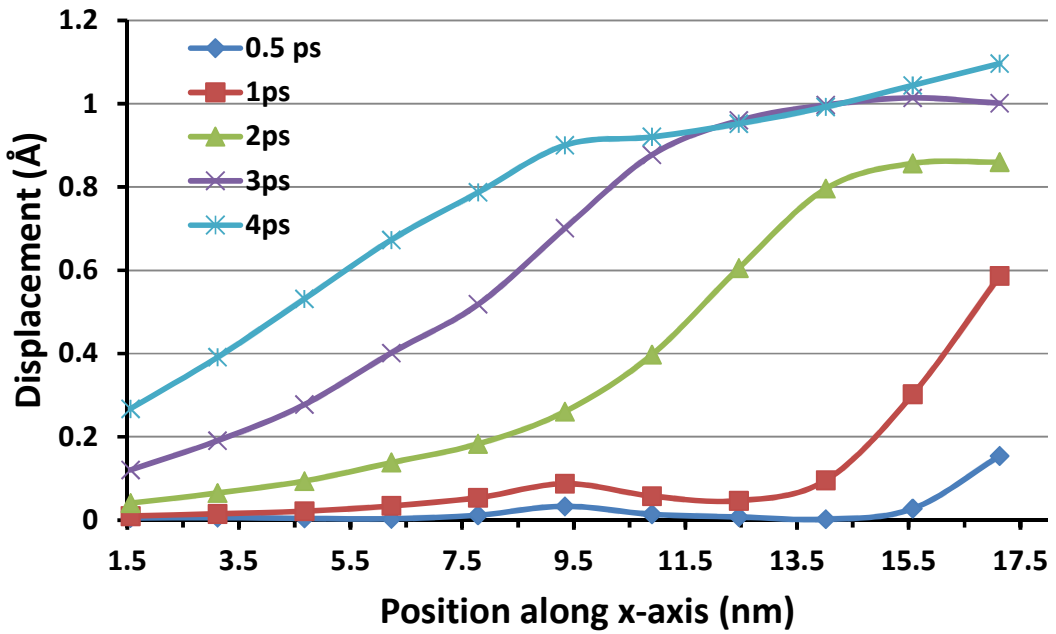


Figure 5.9 Displacement profiles at various times for the physical situation depicted in Fig. 5.6, simulated using the concurrent DPD/MPM model. The edge length of the MPM grid used is 4 Å. The interface between the DPD and MPM subdomains is initially located at  $x \approx 9.35$  nm.

### 5.3.2 Tension Test

Next, the concurrent method is used to simulate a Cu rod under tension, as shown in Fig. 5.10. The rod size is  $578 \text{ \AA} \times 72.3 \text{ \AA} \times 72.3 \text{ \AA}$  ( $80a \times 10a \times 10a$ , where  $a = 7.23 \text{ \AA}$ ). The rod is divided into three regions: one DPD region (with size  $40a \times 10a \times 10a$ ) in

the middle as shown in green, two identical MPM regions (with size  $20a \times 10a \times 10a$  each) symmetrically located at the two sides. The two ends, each of thickness  $15 \text{ \AA}$ , are treated as rigid bodies with a constant velocity of  $1 \text{ \AA /ps}$  applied in opposite directions.

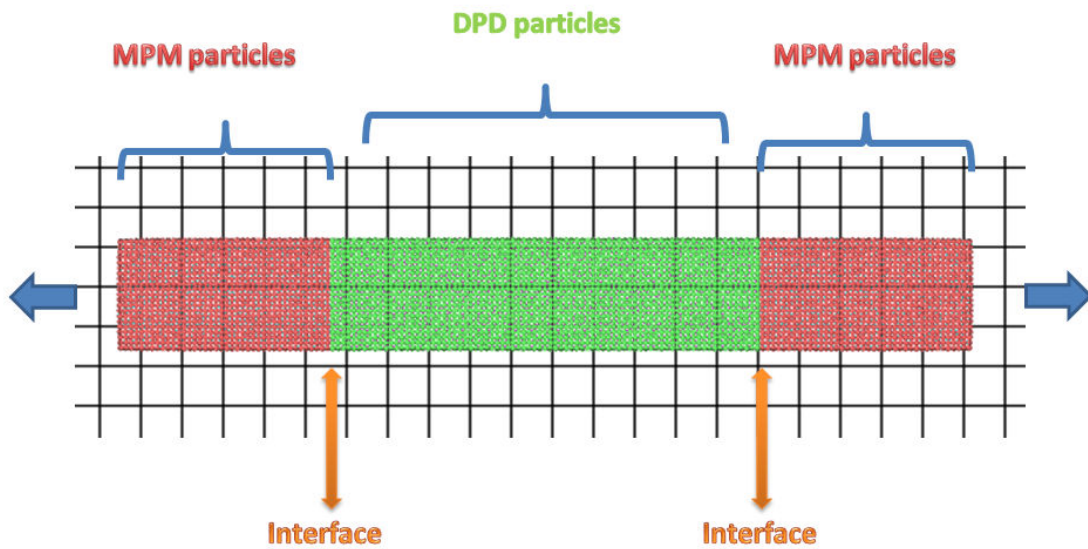


Figure 5.10 Schematic of the concurrent DPD/MPM simulation of a Cu rod under tension.

The rod is divided into three regions: one DPD region in the middle as shown in green, two equivalent MPM regions symmetrically located at the two sides.

Similar to the work in Section 5.3.1, the multiscale simulations of the stretching deformation of the rod were performed with and without the interface treatment. As can be seen in Fig. 5.11, there will be a strong discontinuity on the interfaces between the DPD and MPM regions if the interface treatment is not considered in the multiscale simulation procedure. The three parts of the single Cu rod are separated into independent blocks under the dynamic tensile loading, which is obviously not showing the true deformation of the structure. This is due to the reason that, in the model without the interface treatment, the force on each DPD particle is calculated only from its neighbor

DPD particles within its cutoff radius. The difference between the forces on DPD and MPM particles leads to the discontinuity of the deformation and makes the interface region the weakest point of the entire structure for the failure. Therefore, the fracture will first occur on these interfaces between the two types of particles. However, this is not true for a single computational domain if both DPD and MPM particles are used to describe the same material in the same structure.

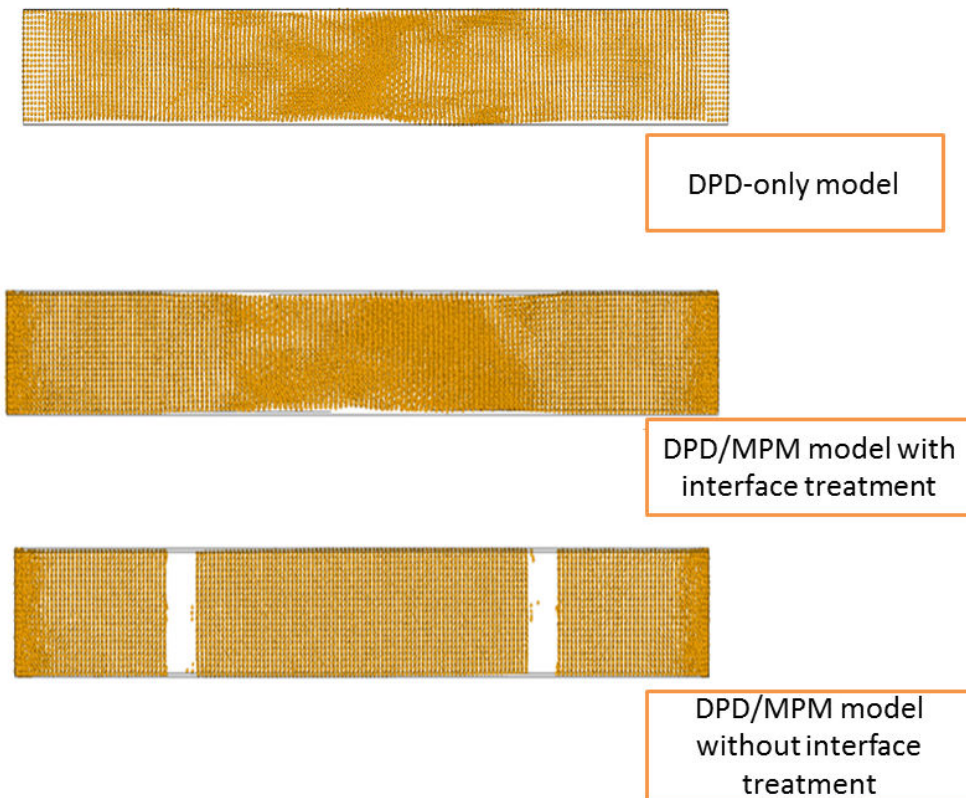


Figure 5.11 Deformation of the Cu rod under tension with DPD-only model, DPD/MPM models with and without interface treatment.

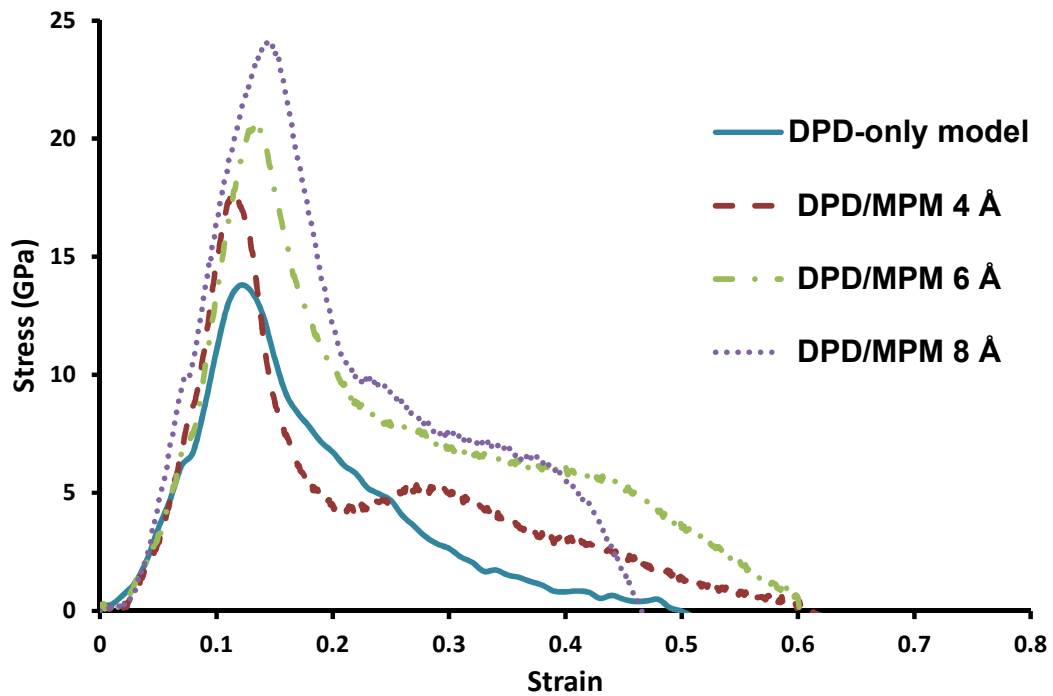


Figure 5.12 Stress-strain relations for the Cu rod under tensile loading at strain rate of 0.0035/ps., simulated using the DPD-only model (solid curve) and concurrent DPD/MPM model for different MPM cell edge lengths (dashed, dot-dashed, and dotted curves).

By using the interface treatment in the intermediate regions between DPD and MPM parts, as discussed in Chapter 2 and illustrated in Fig.2.1, the differences of force calculations will be smeared for the two parts. As can be seen in the second panel of Fig. 5.11, the Cu rod simulated by the concurrent DPD/MPM model shows a consistent mechanical behavior under tension as an integral structure, with the proposed interface treatment. As the strain becomes large enough, necking of the rod can be observed, which is much closer to the deformation configuration of the one simulated by the DPD-only model.

It is further demonstrated in Fig. 5.12 that the concurrent DPD/MPM model with the interface treatment is able to predict a good enough stress-strain relationship within

the elastic regime. Similarly to the curves in Fig. 5.5, the plots of the stress-strain relations of the Cu rod under tensile loading show that the elastic responses for the DPD-only model and the concurrent DPD/MPM model are still generally consistent with each other. This implies that, for suitable MPM grid edge length, the concurrent DPD/MPM model can predict the same elastic response but with less computational resource, since the MPM particles are introduced. Thus, they do not need any particle-neighbor searching algorithm for the force calculation. Compared to the coupled DPD/MPM-grid model, a similar trend of the concurrent DPD/MPM model for the convergence study can also be found, that is, as the resolution of the grid is increased, the peak stress approaches the value obtained by the DPD-only model.

In addition, for the concurrent DPD/MPM model and DPD-only model, one should note that although the general deformation modes are similar, the detailed defects distributions are not exactly the same for the two cases. Because the forces of the particles in the MPM regions are calculated by using the constitutive law at the continuum level (with the use of basic mechanical properties as initial input obtained from the mesoscale level), they are actually “coarse-grained” once again (MD particles are first coarse-grained to mesoscale DPD particles). Thus, the MPM regions are able to only predict the properties from continuum mechanics, with a loss of detailed material defects information. However, as long as the MPM particles can predict the general dynamic response of the structure without losing the essential mechanical properties, one could use them in the areas that do not require highly detailed material descriptions. In contrast, the DPD regions can be used in the areas where more detailed information of the

material deformation is required, such as the necking region of a bar under tension, or the impact surface where defects will initially nucleated and evolved.

## **5.4 Summary**

Based on the coupled DPD/MPM-grid model and concurrent DPD/MPM model described in Chapter 2, several numerical tests of the dynamic and impact responses of discrete nano structures have been performed in this chapter. For the impact problems, the multi-scale simulation can predict a wave speed that is similar to those obtained from all-atom MD simulation and DPD-only simulation. For the dynamic tension test, the proposed multi-scale procedure is able to predict the value of elastic modulus that is approximately the same as those from the MD and DPD-only simulations. The simulation results demonstrate that the DPD details can be effectively coarse grained through the use of a coarse MPM background grid (the DPD/MPM-grid model) while the concurrent link between the MPM and DPD enables the near-seamless integration of constitutive modeling at the continuum level with force-based modeling at the mesoparticle level (the DPD/MPM model).

## **CHAPTER 6. MULTI-SCALE SIMULATION OF NANOSTRUCTURE ASSEMBLY IN CONFINING FLUID**

### **6.1 Introductory Remarks**

As reviewed and discussed in Chapter 5, self-assembled composites of nanorods and nanoparticles (Apperson et al. 2007) have been synthesized recently with the purpose of realizing a better fuel and oxidizer assembly to optimize the performance of a nanothermite. Such composites have been simulated by using an equation of state at the continuum level, with a coupled computational scheme of both fluid and solid dynamics realized in the material point method. However, the previous simulation was performed under the assumption that the nanostructural features of the nanothermite could be neglected and no atomistic details were considered (Gan et al. 2010). In practical situations, the detonation behavior of nanothermite can be actually affected by many factors, such as composite morphology and constituent particle sizes and shapes. As an initial step toward understanding the dynamic response of these materials, the effects of impact velocity, aspect ratio, and sample size on the impact response of nanostructures were studied, as shown in Chapter 3. The nanostructure inclusions in hydrodynamic gaseous fluid were also simulated, to investigate the pressure-volume relationship and the nanostructural transition under high pressure. These simulations provided rich details at the atomic level. In addition to the study of the discrete nanostructures that subject to dynamic and impact loading by using the particle-based multi-scale simulation method

(shown in Chapter 5), the work described in this chapter will further demonstrate that the proposed procedure is able to predict the mechanical behavior of the inclusion of a single nanostructure as well as a nanostructure assembly in the hydrodynamic fluid. Compared with the results obtained by the atomistic simulations shown in Chapter 4, the pressure-volume relation of Cu inclusion will be evaluated first, to demonstrate the capability and accuracy of realizing the multi-scale simulations of nanoparticle inclusion in the fluid under high pressure. Then, the solid-state sintering behavior of the particle-particle and particle-rod assemblies in confining fluid will be further simulated with different initial arrangements.

## 6.2 Computational Set-up

### 6.2.1 Single Inclusion in Confining Fluid

Similar to the initial atomistic model (MD simulation) of Kr-Cu system shown in Chapter 4, a fluid system containing 7930 MPM particles in a cubic-shaped 3-D periodic simulation cell was first prepared in a fixed box with a size of  $144.6 \times 144.6 \times 144.6 \text{ \AA}^3$ . From the standard MPM algorithm discussed in Chapter 2, it can be found that the discretization procedure and numerical scheme should be valid for both solids and fluids because no constitutive equations are invoked in the development of MPM momentum equations. The major difference between fluid and solid material points is the constitutive laws at the continuum level they follow. For the current solid-fluid interaction model studied in this dissertation, the EoS of ideal gas is used for the MPM particles. For ideal gas, the EoS can be formulated as

$$P = (\gamma - 1)\rho I, \quad (6.1)$$

where  $P$  is the pressure,  $\rho$  is the density,  $I$  is the internal energy of the gas,  $\gamma$  is the ratio of specific heats (taken to be constant,  $\gamma = 1.4$ ). To investigate the influence of the hydrostatic pressure on the mechanical properties of the embedded inclusions, the initial pressure of the ideal gas can be set to different values, such as 0.01 GPa, 1 GPa, 3 GPa, and 5 GPa, which correspond to different values of internal energy. A detailed MPM simulation procedure for the fluid can be found in the previous work (Gan et al. 2010).

Figure 6.1 shows the sketch of the 3-D concurrent DPD/MPM model of a single inclusion (a cube of Cu particles) embedded into the geometric center of the simulation box filled with ideal gas. The solid Cu inclusion is represented by 4631 DPD particles with a size of  $10a \times 10a \times 10a$  ( $a = 7.23 \text{ \AA}$ ), which has the same lattice spacing and mesoparticle force expression used for the Cu material studied in Chapter 5. Before it was inserted into the fluid, the initial solid inclusion consisting of DPD particles was equilibrated for 500 ps at 298 K and zero pressure by using the Berendsen thermostat (Berendsen et al. 1984). The final phase space point from the equilibration was used as the initial condition and then embedded into the MPM particles for the concurrent DPD/MPM simulations. The coupled DPD/MPM model was then equilibrated at a desired pressure for 100 ps at 298 K with a time step of 0.01 ps.

Similar to what was done in Chapter 5, CNA (Faken and Jónsson 1994) with the lattice constant  $a$  was used to identify the local coarse-grained crystal structures of the DPD particles. In the results of this chapter with connection to the particle configurations, fcc coarse-grained particles are shown as green, hcp particles are shown as red, and the remaining atoms (classified as disordered or surface particles) are shown as white. The

MPM particles of the ideal gas are shown as cyan. Because the ideal gas has no ordered crystal structure, CNA is not applied.

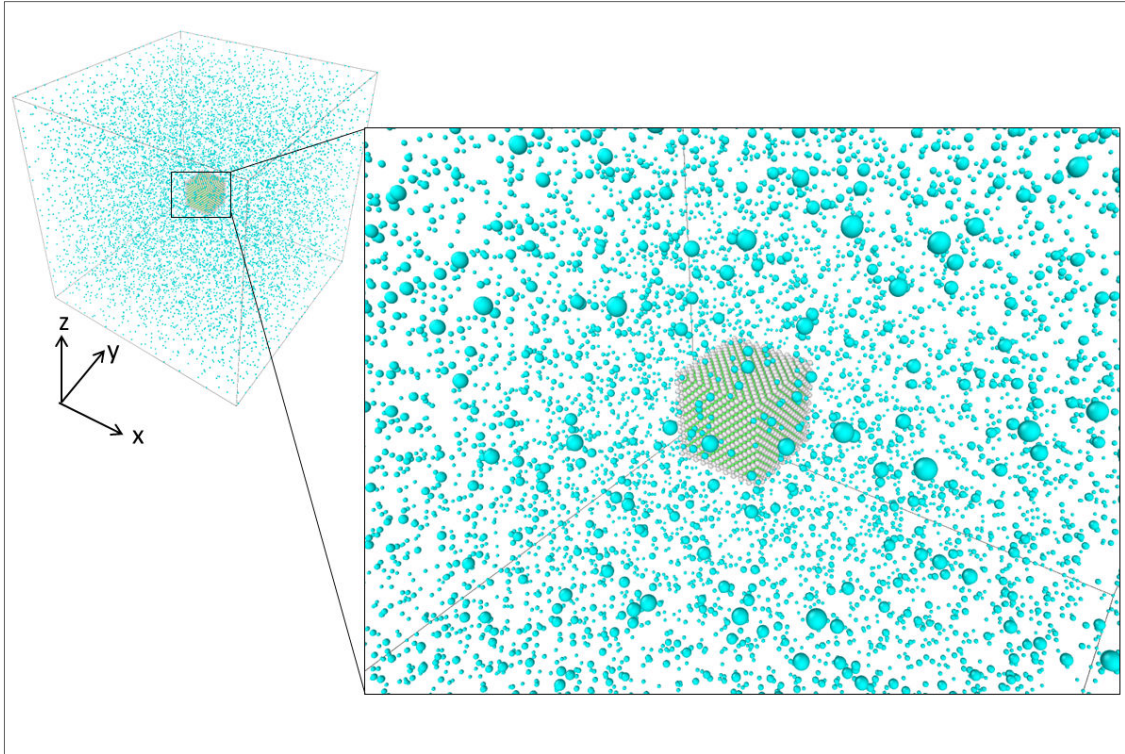


Figure 6.1 3-D configurations of the Cu inclusion in the fluid with the concurrent DPD/MPM model.

### 6.2.2 Particle/Rod Assembly in Confining Fluid

The coupled DPD/MPM model of particle/rod assembly in confining ideal gas is very similar to that of single inclusion in the fluid. Because there was more than one discrete nanostructures inside the fluid, the fixed simulation box was set with a larger size of  $216.9 \times 216.9 \times 216.9 \text{ \AA}^3$ . The fluid was considered as ideal gas consisting of 9261 MPM particles. Meanwhile, there were two basic models constructed for the particle/rod assemblies, namely, particle-particle model and particle-rod, which were both represented by DPD particles. In all cases considered in this chapter, each spherical nanoparticles

consists of 1048 DPD particles and the radius of the nanoparticle is  $4a$ . The rod simulated in the current work consists of 3647 DPD particles. It was considered as a cylinder with the radius  $4a$  and the length  $18a$ . All other parameters for the concurrent DPD/MPM simulation and basic numerical steps are the same as those given in Section 6.2.1.

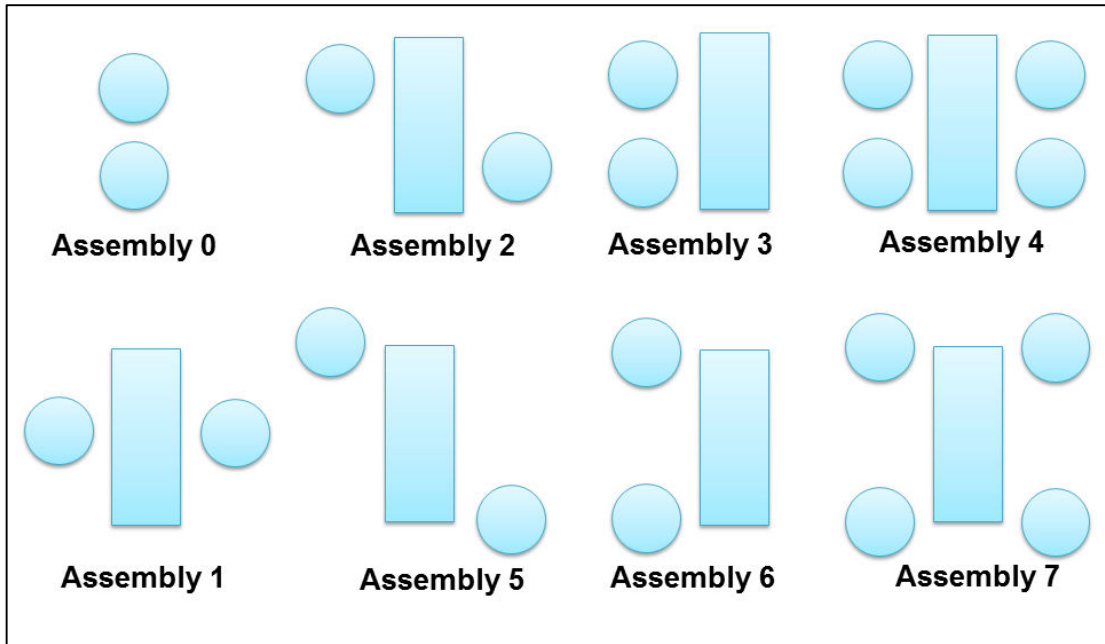


Figure 6.2 Sketches of the particle/rod assemblies with different arrangements of the components.

The sketches of the particle/rod assembly models are illustrated in Fig. 6.2. Eight assemblies with different particle/rod arrangements named after Assembly 0, Assembly 1, ..., Assembly 7, respectively, were considered in this work with the concurrent DPD/MPM model.

The model that was simulated first is Assembly 0, which is a basic model consisting of a particle-particle pair. In Assembly 0, no rod is included so that this kind of particle-particle model is similar to those commonly used in the atomistic simulations of

nanoparticle sintering (Jiang, Zhang, et al. 2013). The distance between the two particles (surface to surface) is 7.23 Å.

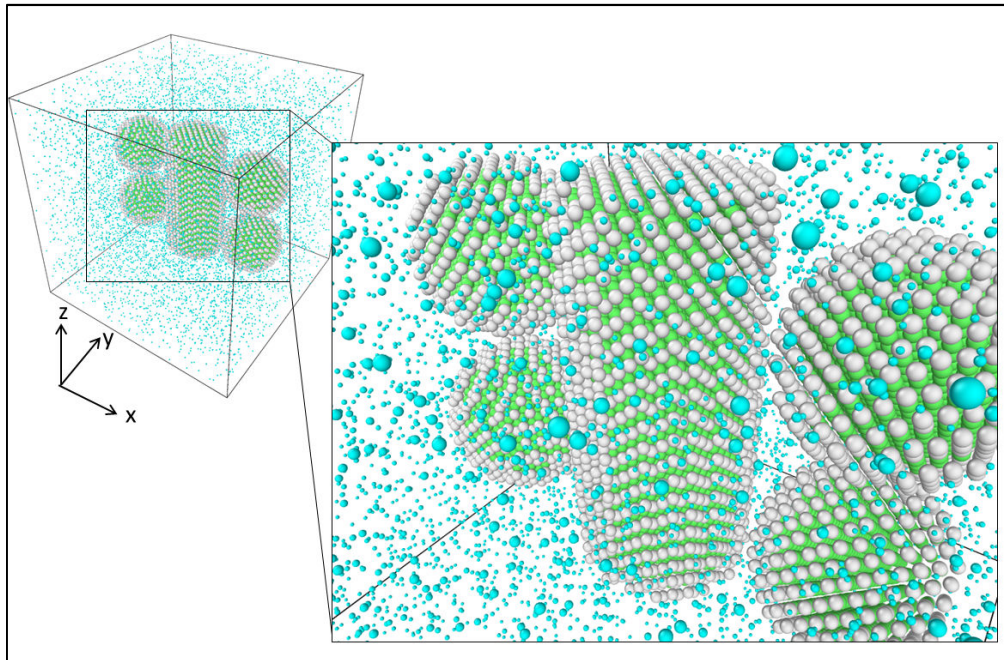


Figure 6.3 3-D configurations of a particle/rod assembly (Assembly 4 as an example) in the fluid with the concurrent DPD/MPM model.

Based on the model of Assembly 0, a nanorod was added into the assembly, which forms a particle-rod model. In Assemblies 1, 2, and 5, the two particles are located on opposite sides of the nanorod, while in Assemblies 3 and 6, the two particles are located on the same side of the nanorod. In Assemblies 4 and 7, there are four particles, with two on each side of the nanorod. The distance between the rod and particles (surface to surface) is 7.23 Å in all particle-rod assemblies. The vertical distance between the particles (surface to surface) is 7.23 Å in Assemblies 2, 3 and 4, and 72.3 Å in Assemblies 5, 6 and 7. Before the assembly was introduced into the fluid, the particle configuration of each component was equilibrated separately for 400 ps at 298 K and

zero pressure by using the Berendsen thermostat (Berendsen et al. 1984). After the components reached to the minimalized energy and pre-stress states, they were inserted into the fluid particles, following the arrangements shown in Fig. 6.2. As a typical assembly model, the 3-D configurations of Assembly 4 with four particles and one rod are shown in Fig. 6.3, wherein the expanded view to the right shows the a detailed configuration of the assembly.

### 6.3 Pressure-Volume Relationship

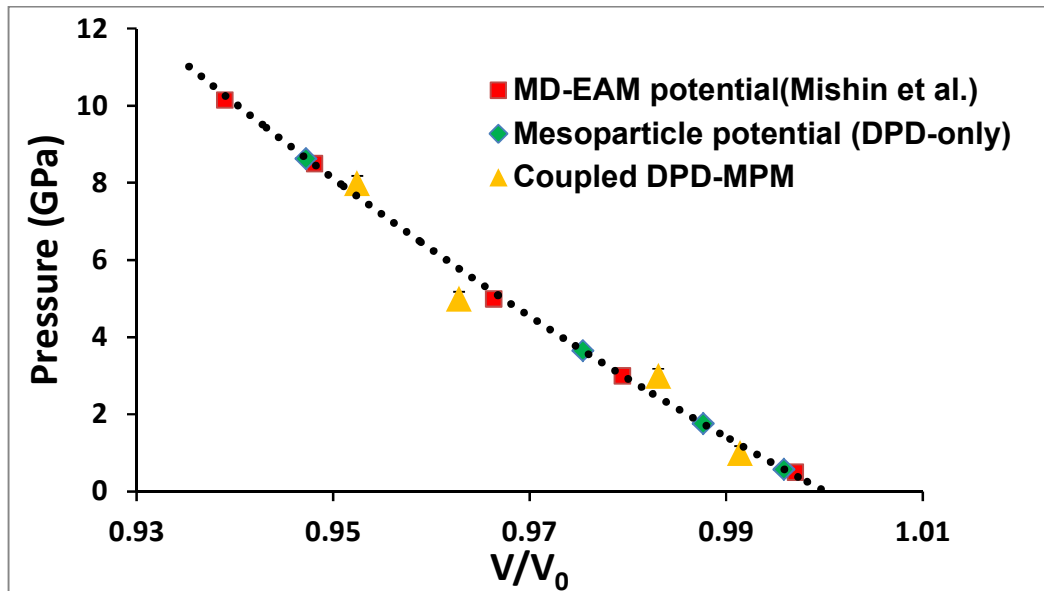


Figure 6.4 Pressure-volume curves for finite-size cubic (simulated by concurrent DPD/MPM model) and bulk (3-D periodic) Cu crystals (simulated by both MD and DPD simulations).

By using the computational model of a Cu inclusion in the confining fluid that was shown in Section 6.2.1, the Pressure-Volume (P-V) relationship is calculated in this section to demonstrate that the proposed particle-based concurrent DPD/MPM model has the capability of predicting a reasonable mechanical property of the material. Following

the same routine used for the atomistic simulations of Cu-Kr system (see the details in Chapter 4), the volume change ( $V/V_0$ ) of Cu inclusion is calculated.  $V_0$  is the initial volume of the Cu inclusion at 1 atm and 298 K.  $V$  is the current volume of the Cu inclusion at current pressure level. The volumes of the sample are estimated by calculating the products of the absolute lengths in three directions of the cubic sample.

For comparison purposes, the P-V curve of the periodic samples with the cell size of  $10a \times 10a \times 10a$  that was simulated by MD simulations in Section 4.3 are redrawn in Fig. 6.4. In addition, a periodic sample with the same cell size that only consists of DPD particles, are simulated with the mesoparticle potential (Gan et al. 2014) to serve as another set of referenced data points for the concurrent DPD/MPM simulations.

As can be seen from the curves of the pressure-volume compression ratio in Fig. 6.4, the result for the finite-size inclusions simulated with DPD/MPM model is very close to those from the samples simulated using MD and DPD. Also, the results shown here predict the same trend of the P-V curves that are plotted in Fig. 4.3 with the MD simulations. It can be inferred from the P-V curves that the bulk modulus of the Cu samples simulated with different methods (i.e., MD, DPD, and concurrent DPD/MPM) are close to each other. Thus, these results demonstrate that P-V relationship of the Cu inclusion inside the ideal gas can be well predicted by the proposed multi-scale simulation procedure which involves both DPD and MPM particles.

Furthermore, in the DPD/MPM model, it should be noted that the MPM particles are used to discretize the ideal gas, which provides an alternative approach to apply a hydrostatic loading to the solid inclusion inside. For the fluid medium, unlike the MD simulation of Kr gas (see Section 4.2) that requires searching a large number of

neighboring atoms to get the forces, the stresses on MPM particles are directly calculated from the constitutive law, and the loads are able to applied indirectly to the DPD particles of the inclusion by mapping onto the background mesh. Thus, compared to the atomistic model of Cu-Kr system discussed in Chapter 4, the proposed multi-scale model significantly reduces the required computation resource, by using only MPM particles and the EoS of the fluid.

#### **6.4 Particle/Rod Assembly in Confining Fluid**

In this section, the discrete nanostructures (nanorod and nanoparticles) that are extensively investigated in the previous studies by using atomistic simulations (also see Chapters 3 and 4) will be simulated by the proposed particle-based multi-scale simulation procedure. As reviewed in the introduction of this chapter, the self-assembled composite of nanorods and nanoparticles could realize a better fuel and oxidizer assembly to optimize the performance of the nanothermite. However, so far there has been very rare simulation study of the nanostructure assembly under high pressure, since the simulation procedure as well as the more accurate atomic potential function is still under development. As a preliminary investigation in this chapter, the computational models of particle/rod assembly under high pressure are studied by using the concurrent DPD/MPM simulation procedure. The study will show that the deformation patterns of the nanostructures under high pressure vary significantly if the initial arrangement of the components in the assembly differs.

The particle-particle model (Assembly 0) is first simulated to study the solid-state sintering process that usually automatically occurs at the nanoscale. In the past, atomistic simulations of the nanoparticle sintering have been extensively performed (Jiang, Zhang,

et al. 2013). By comparing the simulation-predicted neck growth with the empirical-theoretical formulations, the reliability of MD simulations has been proved for the sintering of metallic nanoparticles (Jiang, Zhang, et al. 2013). However, most MD simulations of these nanoparticles did not consider the effect of the environmental pressure. As discussed in the last section, the proposed DPD/MPM model in this dissertation provides a simple and applicable approach to simulate the environment surrounding the solid inclusions with a desired pressure value.

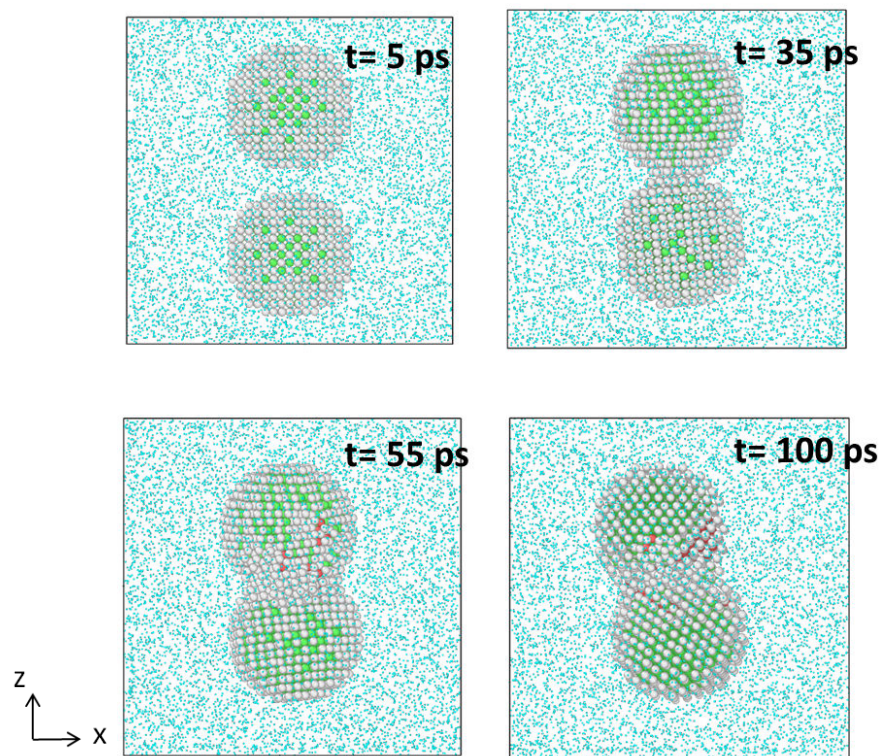


Figure 6.5 Snapshots of the solid-state sintering of the particle-particle model at 1 GPa (Assembly 0).

Figure 6.5 shows the solid-state sintering of the two particles at 1 GPa at room temperature. Similar to what was observed by using MD simulations, the solid-state sintering of the particle pair can also be predicted using the concurrent DPD/MPM

model. A major difference from the all-atom MD simulation is that the DPD/MPM model shown here includes gas particles that serve as the loading medium. Although some of the gas particles are filled in the gap ( $\sim 7.23 \text{ \AA}$ ) between the two spheres, the sintering of the two spheres can still happen by extruding these gas particles. From the snapshots it can be seen that the two nanoparticles are separated for times up to  $\sim 5 \text{ ps}$ . Then, the two nanoparticles move toward each other and become connected with a rapid neck formation. A relatively stable dumbbell-shaped particle is then formed in the later stage (from 55 ps to 100 ps), although the overall structure can exhibit rigid-body motion such as rotations and translations. This phenomenon of solid state sintering at room temperature can be observed for all geometric configurations and for different pressures of the ideal gas.

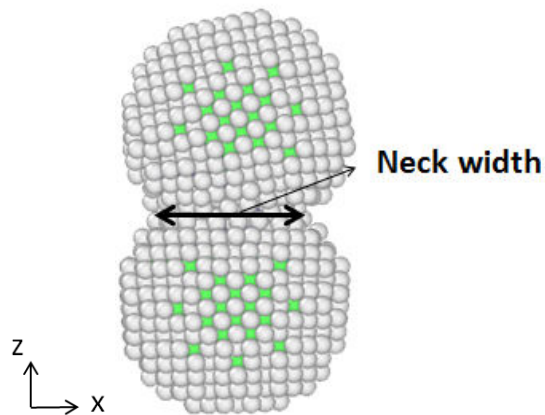


Figure 6.6 Configuration of the dumbbell-shaped particle-particle model after the solid-state sintering.

Figure 6.6 illustrates the formation of a stable neck after the solid-state sintering occurs. The neck width is measured by the smallest diameters of the circular plane in the neck region that is perpendicular to the line between the geometrical centers of the two

spheres, as indicated by the arrows on the configuration in Fig. 6.6. Figure 6.7 shows the time history of the neck width for the same particle pair during the solid-state sintering but with different simulation methods. For comparison, two nanoparticles with the same size are also simulated by using all-atom MD and DPD-only simulations but without any surrounding gas particles. From the curves of neck width in Fig. 6.7, it can be seen that the DPD-only model predicts a slightly higher value of the stable neck width than that obtained from MD simulation. This may be due to the error from the mesoparticle potential function that is still currently under development for the Cu material. The neck width predicted by the concurrent model at 0.01 GPa is almost the same as that of the DPD-only model, which suggests that concurrent DPD/MPM procedure is able to predict a reasonable solid-state sintering process at room temperature.

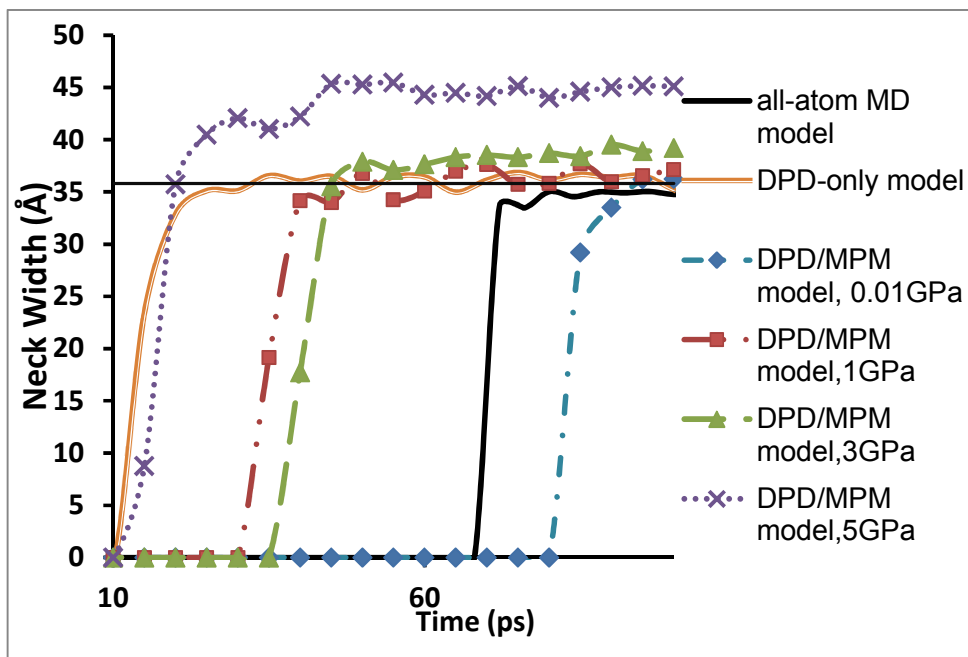


Figure 6.7 Time history of the neck width of the particle-particle model with the concurrent DPD/MPM model at different pressure levels, compared by that obtained from MD and DPD simulations

In addition, the effect of the pressure on the sintering of the nanoparticles is also studied. From the curves plotted in Fig. 6.7, it can be found that the value of stable neck width increases with the increase of the surrounding pressure of the gas. The stable neck width of the particle-pair at 5 GPa is much higher than those obtained at lower pressures. This means that as the pressure applied to the inclusions increases, the particle-pair can reach a more thoroughly sintering state.

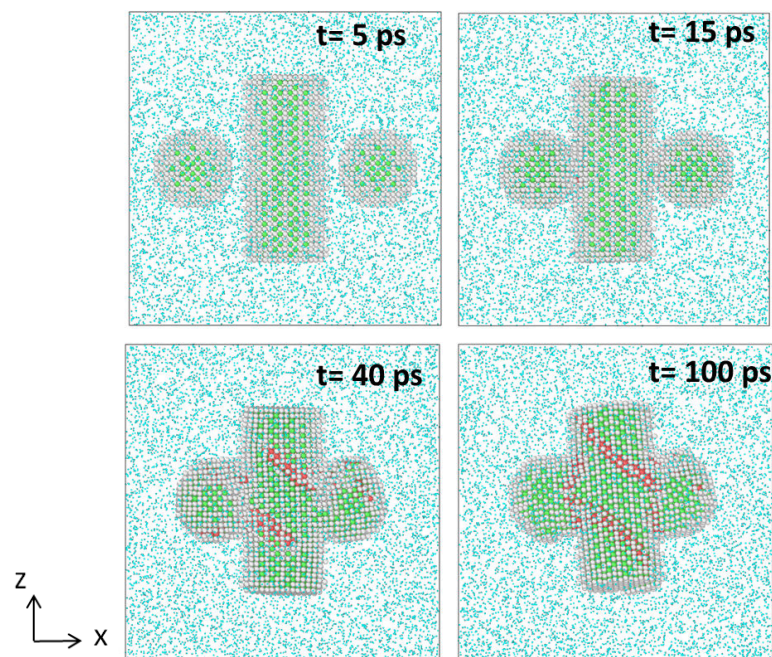


Figure 6.8 Snapshots of the particle/rod assembly model (Assembly 1) at 1 GPa.

Building on the particle-pair model, a rod is added into the assembly. The snapshots of the interactions between the particle and particle, as well as particle and rod, are shown in Figs. 6.8-6.16. Similar to the particle-particle interaction, the solid-state sintering can also occur between the particle and rod at different pressures with various initial arrangements. However, the deformation pattern of the assembly can differ due to the change of relative positions of the components.

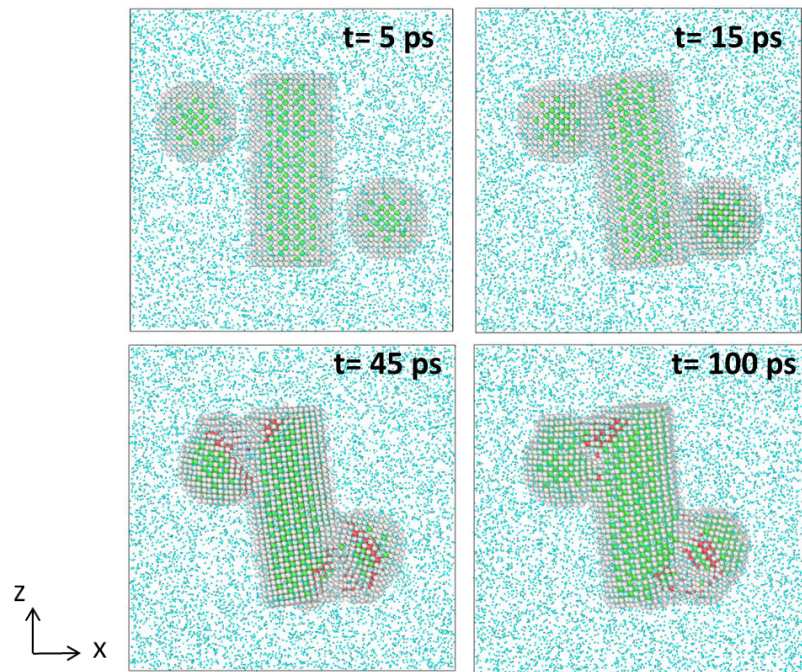


Figure 6.9 Snapshots of the particle/rod assembly model (Assembly 2) at 1 GPa.

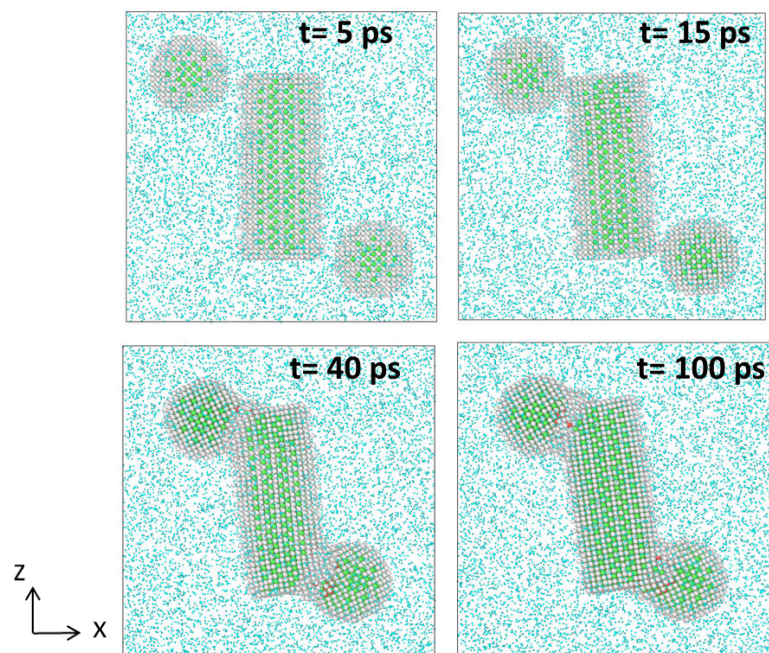


Figure 6.10 Snapshots of the particle/rod assembly model (Assembly 5) at 1 GPa.

Figure 6.8 shows the snapshots taken at different time steps during the simulation of the cross-like Assembly 1. The spheres first can move toward the rod, due to both the attractions between the rod and particles and the pressure from the surrounding gas (compare snapshots at  $t=5$  ps and  $t=15$  ps). Then the assembly becomes stable without too much change of the relative positions between the sphere and rod, although certain rigid body motions (such as translation and rotation) of the entire structure occur (by comparing snapshots at  $t=40$  ps and  $t=100$  ps). It was determined that the deformation of the material in the rod is mainly accommodated by the lattice slips on the  $\{111\}$  planes of the material, which is similar to that obtained in MD simulations. It can be demonstrated in the snapshot at 40 ps that the ‘stacking faults’ are formed near the contact surface in the coarse-grained mesoparticle structures of the rod. The slip events occur initially at the places in contact regions, which results in the emission of “partial dislocations” and forms a relatively stable parallel pattern of the ‘stacking faults’ on the same type of  $\{111\}$  planes (see the snapshot at  $t=100$  ps).

Figure 6.9 shows the snapshots of Assembly 2, which possesses rotational symmetry but non-centrosymmetric. As can be seen in the snapshot at  $t=15$  ps, the spheres attach onto the rod from both sides but on the different ends. Thus the axis of the rod tilts off the  $z$ -direction with the two ends leaning on the spheres at opposite directions. Then the nanoparticles began to rotate and reorient to yield a relatively minimized energy state of the crystal structure, as can be seen in the snapshot at  $t=45$  ps. Most transient ‘stacking faults’ are formed in the nanoparticles; relatively few are formed in the nanorod. This might be because the contact regions between the rod and particle in this assembly are near the corners, and there is limited space for the defects to expand.

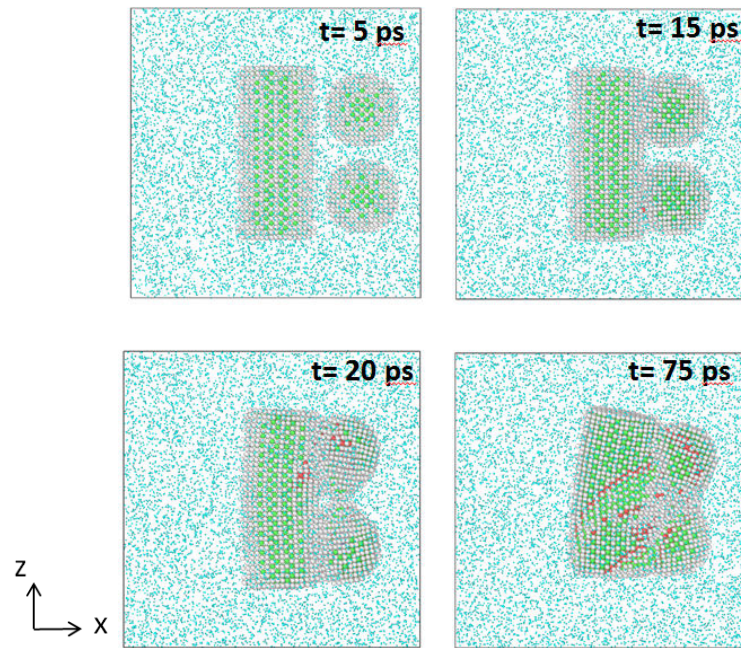


Figure 6.11 Snapshots of the particle/rod assembly model (Assembly 3) at 1 GPa.

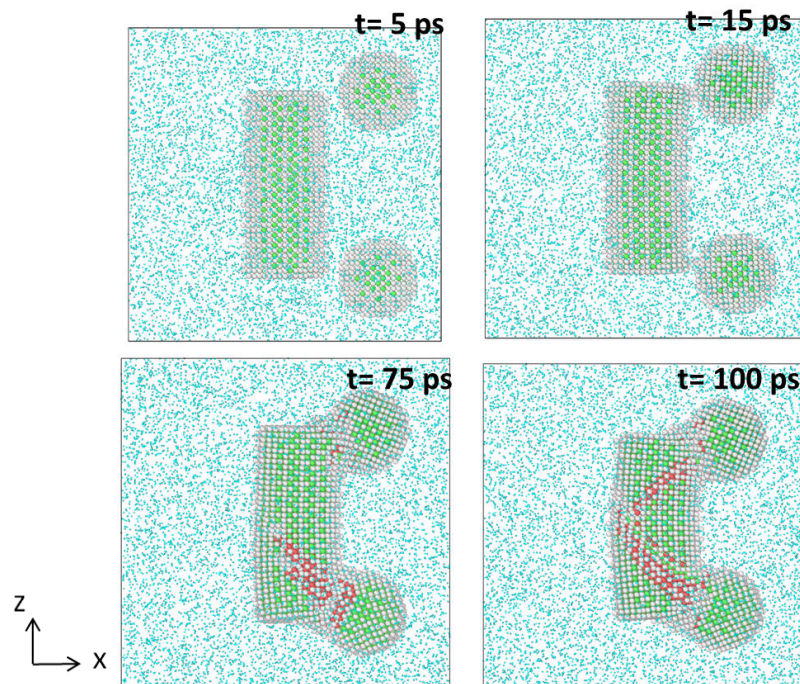


Figure 6.12 Snapshots of the particle/rod assembly model (Assembly 6) at 1 GPa.

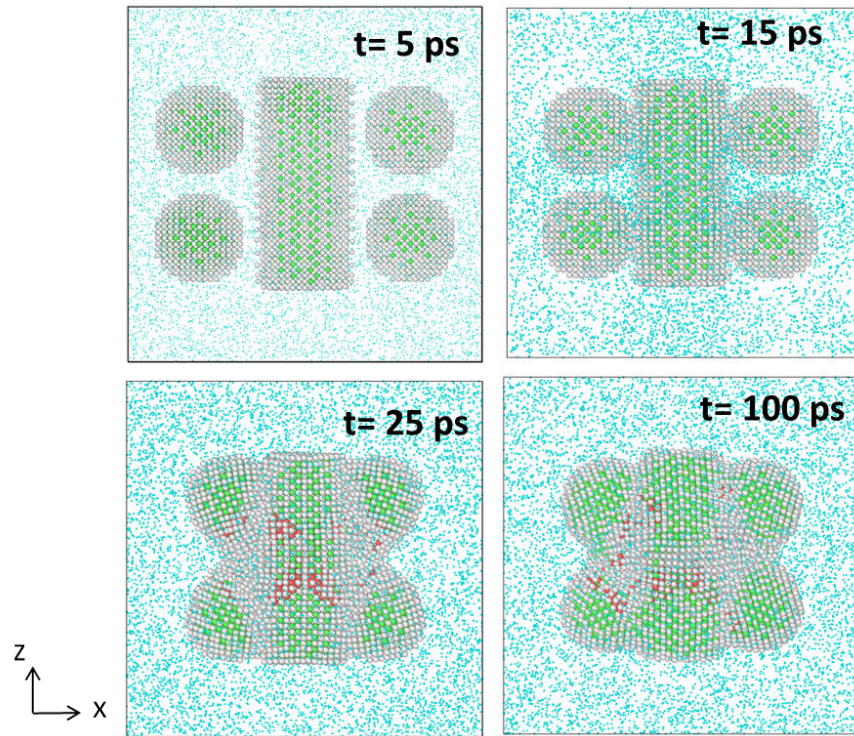


Figure 6.13 Snapshots of the particle/rod assembly model (Assembly 4) at 0.01 GPa.

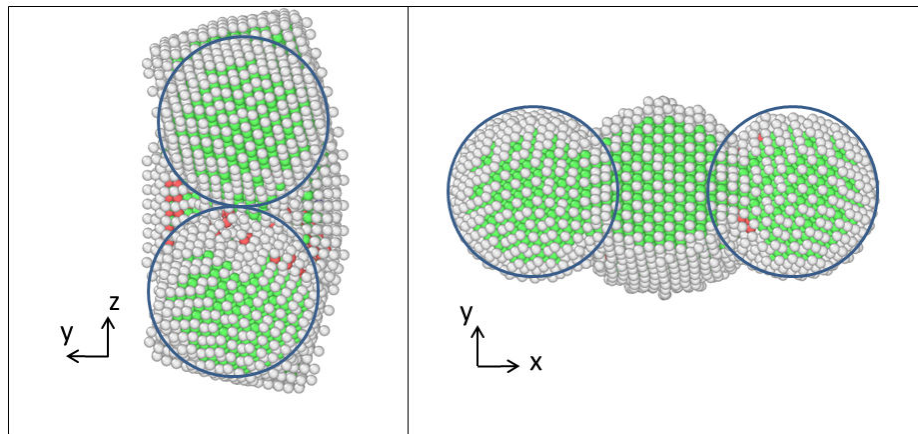


Figure 6.14 Snapshots of the particle/rod assembly model (Assembly 4) at 0.01 GPa.

A similar assembly (Assembly 5) but with a larger offset distance of the particles in the  $z$ -direction is simulated, as shown in Fig. 6.10. The deformation pattern is almost as the same as that of Assembly 2. But less lattice slip events are found because the

contact regions between the rod and particle are almost right on the corners of the rod, which provides little room for the “stacking faults”.

Fig. 6.11 shows the snapshots of Assembly 3 with both the two particles on the same side of the rod. It can be seen that at  $t=15$  ps, the two particles reach the surfaces of the rod. After they are connected to the rod, the two spheres start to move toward each other and the sintering of the nanoparticles occurs (see snapshot at  $t=20$  ps). The attraction between the two particles leads to the bending deformation that occurs in the nanorod. It can be seen from the snapshot at 75 ps that the solid-state sintering of the three components is completed. The assembly becomes more stable with a thoroughly reduced total free surface, since the gap between the two spheres and rod is totally filled up with the DPD particles after the sintering process is done. It can also be noticed that the ‘deformation twins’ can form in the rod due the bending of the rod, which is in a good agreement with the configurations of bending nanowires that were shown in Figs. 3.4 and 3.5 in Chapter 3.

Corresponding to Assembly 3, Assembly 6 was simulated with a larger setoff distance between the two spheres on the same side, as shown in Fig. 6.12. Different from the pattern in the Assembly 3, although the sintering between the rod and spheres happens, the spheres are unable to connect with each other through the sintering because of the increased distance between them. However, due the attraction as well as the surrounding pressure, the two particles still have a tendency to move towards each other to the middle, so that a slight bending deformation happens with two sets of “stack faults” on different types of  $\{111\}$  planes finally joining up in the middle of the rod.

Figure 6.13 shows the assembly (Assembly 4) in which each side of the rod has two particles located adjacently. The deformation pattern during the sintering process at a very low pressure (0.01 GPa) shows a quite symmetrical shape. It can be found that the four particles attach on the surface of the rod almost simultaneously (see the snapshot at  $t=15$  ps). Then, similar to the case of Assembly 3, the particle pair on each side begins to move attractively into the middle, shrinking the space of the gap circled by the spheres and rod, as can be seen in the snapshot at  $t=25$  ps. The sintering processes of both particle pairs are completed at almost the same time, so all components including four particles and the rod are assembled into one single nanostructure without any cavity inside. Hence, the rod looks to be balanced and the shape of the assembly after the solid-state sintering seems to be symmetric, from the view of  $x$ - $z$  plane shown in the snapshot at  $t=100$  ps. However, the rod is actually still bent due the sintering of the two particle pairs. As can be seen in Fig. 6.14 from different points of view, because the two pairs of the particles from both sides are competing with each other equally and get connected almost at the same time along the  $z$ -direction, the rod does not bend on the  $x$ - $z$  plain. Instead, since the spheres rotate on the  $y$ - $z$  plane, the bending deflection of the rod is shown to be on the  $y$ -axis after the particle pairs are sintered.

In contrast, the components in Assembly 4 do not always tend to form a symmetric pattern. Figure 6.15 displays a non-symmetric pattern of the assembly at the case of 1 GPa pressure. This may be due to the locally non-homogeneous distribution of the gas particles surrounding the discrete components that play a greater role in interacting with the spheres and rod at a higher pressure level.

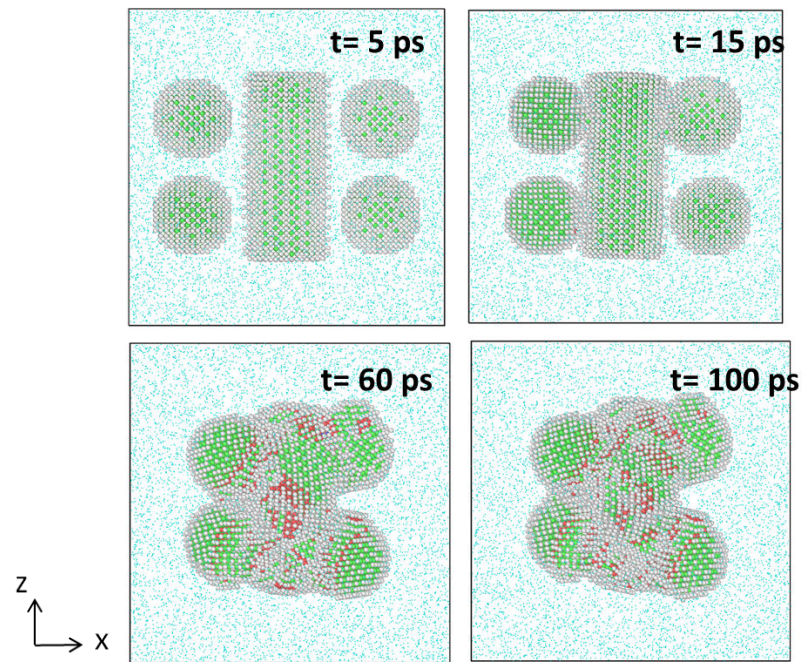


Figure 6.15 Snapshots of the particle/rod assembly model (Assembly 4) at 1 GPa.

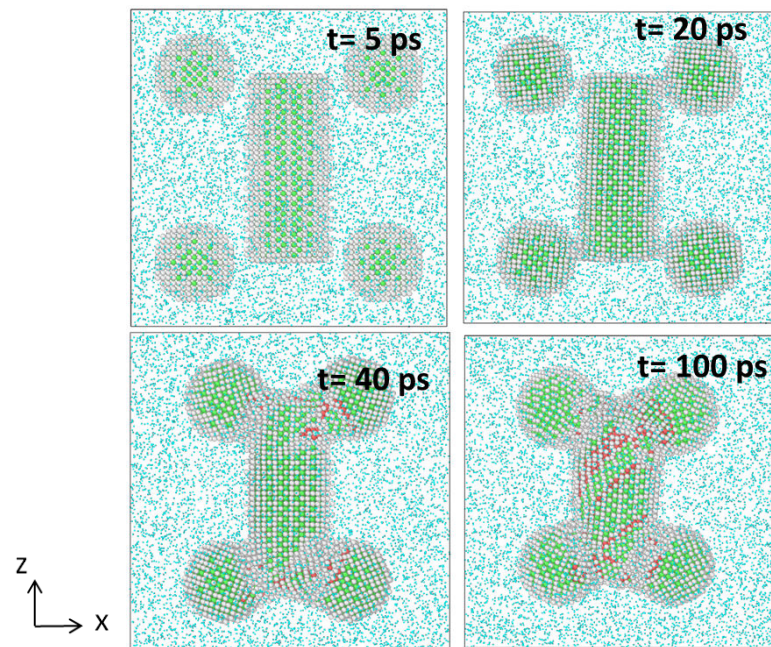


Figure 6.16 Snapshots of the particle/rod assembly model (Assembly 7) at 1 GPa.

Table 6.1 Comparison of the CPU time consumed for simulating a particle-particle solid-state sintering with different simulation methods

	MD simulation (serial)	MD simulation (parallel)	DPD/MPM simulation
Simulated inclusion size (radius, Å)	4	4	4
Total simulation time (ps)	100	100	100
Number of MD particles	17,178	17,178	N/A
Number of DPD particles	N/A	N/A	2,096
Number of MPM particles	N/A	N/A	8,482
Total number of particles	17,178	17,178	10,524
Number of processor used	1	8	1
Max. memory (MB)	51	306	98
Max. swap (MB)	458	1799	574
Total CPU time (sec)	2561.53	2976.54	663.35

As can be seen in the snapshot at  $t=15$  ps in Fig. 6.15, the spheres do not attach onto the rod simultaneously, so that the rod is tilted. The two particles on the left-hand side first reach the surface of the rod, so that they start to sinter with each other prior to the completely attachment of the lower particle on the right-hand side. As a result, the

first sintered particle pair causes the rod to bend toward the left-hand side (see in the snapshot at  $t=60$  ps). This in turn leads to a much larger distance between the spheres on the right-hand side, which makes it impossible for the two on the right to sinter together. Finally the non-symmetric deformation pattern becomes stable with a totally larger area of free surface in the assembly than that obtained in case shown in Fig. 6.13.

Corresponding to Assembly 4, Assembly 7 is simulated with a larger offset distance between the two spheres on each side. Similar to case shown in Fig. 6.15, at 1 GPa pressure, the particles do not tend to attach on the rod at the same time so that the rod can still be tilted, as can be found in the snapshot at  $t=20$  ps in Fig. 6.16. However, since at this case the gap between the spheres is increased, no sintering between the particle pairs can actually occur. Hence, there is no competition between the two pairs to cause the bending behavior of the rod (see the snapshot at  $t=40$  ps). The deformation pattern of this assembly can still show a symmetrical shape as what it initially looks like. As shown in the snapshot at  $t=100$  ps, finally the components form a “dog-bone” assembly when the sintering is completed between the particles and rod.

Finally, another important feature, the consumption of the computation resources that required by the proposed concurrent multi-scale procedure, is compared with those obtained from MD simulations. As can be seen from Table 6.1, to simulate the solid-state sintering process of the same particle-particle assembly (Assembly 0) for 100 ps, the concurrent DPD/MPM simulation consumed 663.35 seconds of CPU time, which was done on one 64-bit Intel Xeon processor. In contrast, both MD simulations (serial and parallel) took more than 2500 seconds of CPU time on the processors with the same model. The memory required by the concurrent DPD/MPM simulation (98 MB) is larger

than the serial MD simulation (51 MB), but is much smaller than the parallel MD simulation (306 MB). The comparison in table 6.1 demonstrates that great efficiency of the proposed multi-scale simulation procedure for simulating the similar sintering problem of two particles. Future work should be done to refine the concurrent DPD/MPM code with some more efficient algorithm (such as using neighboring-list algorithm instead of simple iteration algorithm searching for DPD neighbor particles), to further reduce the memory required for computation.

## **6.5 Summary**

The work shown in this chapter is an extension of the research in Chapter 4 to further explore the application of the proposed particle-based multi-scale simulation (concurrent DPD/MPM) procedure in the study of nanostructure assembly in the confining fluid at various pressure levels. The major results are summarized as follows:

First, the pressure-volume relationship has been calculated by using the computational model of a Cu inclusion in the confining fluid. The result for the finite-size inclusions simulated with DPD/MPM model is shown to be very close to those samples simulated with MD and DPD simulations.

Second, for the model of particle-particle assembly in the confining fluid, the result of neck width predicted by the concurrent DPD/MPM model is shown to be almost the same as that obtained from the DPD-only model, which suggests that proposed multi-scale procedure is able to predict a reasonable solid-state sintering process at room temperature. By using the concurrent model, the hydrodynamic loading of the solid inclusion is able to be realized through using the MPM particles, described by the EoS of

the fluid. The simulation results show that the more pressure applied to the inclusions, the more thoroughly sintering state the inclusions can reach.

Finally, the computational models of particle/rod assembly with different initial arrangements under high pressure have been studied by using the concurrent DPD/MPM simulation procedure. The simulation results show that with the change of initial positions of the components in the assembly, the deformation pattern of the nanostructure under high pressure can be varied largely. By tailoring the distance between the components, the discrete nanostructures can be assembled to form some particular shapes and a thoroughly solid-state sintering of the components can be obtained with the smallest area of entire free surface.

Overall, the simulation results shown in this chapter have demonstrated that the proposed particle-based concurrent DPD/MPM model has the capability of predicting reasonable mechanical properties of the material, and requires much less computational time than the atomistic simulations to simulate similar problems.

## CHAPTER 7. CONCLUSION AND FUTURE WORK

### 7.1 Summary of the Work

Due to the recent need for modeling and simulating multi-scale structural responses to extreme loading conditions, such as the infrastructural sensor network response to blast/impact as well as nano energetic structural response, a particle-based multi-scale simulation procedure within the MPM framework has been proposed and developed in this dissertation. This multi-scale simulation procedure includes a hierarchical bridge from MD to DPD and a concurrent link between DPD and the MPM. In addition, a simple interfacial treatment has been proposed for concurrent DPD/MPM simulations based on the features of the DPD force expression and the MPM constitutive model.

To gain a fundamental understanding of deformation mechanism at the atomic-scale and provide basic references for the multi-scale simulation firstly, atomistic modelling and simulation of discrete metallic nanostructures under various extreme loading conditions have been performed. The loading conditions considered in this work include basic mechanical loading (tension/torsion/bending), impact loading (transverse impact and longitudinal impact), and hydrodynamic loading. A detailed deformation mechanism and dynamic response of these nanostructures have been investigated. Meanwhile, the formation of some special nanostructures under the different simulated loading conditions has also been observed.

Based on these studies of the material/structure with the atomistic simulations, the proposed multi-scale (concurrent DPD/MPM) simulation procedure has been used to simulate the dynamic and impact responses of discrete nanostructures. Compared by the results obtained from MD simulations, the concurrent DPD/MPM model has shown the capability to predict some reasonable mechanical properties of the materials. Particularly, the mechanical behavior of the inclusions of a single nanostructure as well as the nanostructure assembly in the hydrodynamic fluid has also been studied by using the proposed concurrent DPD/MPM simulation.

## **7.2 Major Findings**

Major findings from the research of this dissertation are summarized as follows:

- The atomistic modeling and simulation of metallic nanostructures subject to various loading conditions have been presented in this dissertation, and have revealed interesting phenomena that are not expected to exist at the macroscopic scale. The general deformation mechanism of these low-dimensional nanostructures shows that the lattice slip can occur initially at the regions near free surfaces, which results in the emission of partial dislocations. Due to a large portion of surface atoms, surface-related activities play a dominant role in determining the mechanical properties of the nanostructure. MD simulation results show that the crystal plasticity and the deformation patterns of the nanostructures depends not only on the sample geometry (shape and size), but also on the loading conditions and stress states. Some special nanostructures can be formed during the deformation process, such as single and multiple conjoint fivefold twins, and quasi-icosahedral structures. For impact mechanics problems studied in this work, the size effect on the transverse impact response seems to be related to the

distance between sample corners (sources of stress or strain concentration), while the size effect on the longitudinal impact response relies on the ratio of free surface to volume.

- From the atomistic simulation results of nanoparticle inclusion in the fluid, the P-V relations of solid Cu nanoparticles have been obtained by inserting the particle inclusions into the Kr gaseous fluid at various hydrostatic states. The results can be used as baseline data to compare with those from multi-scale simulations. It is found that the P-V relation for the Cu inclusion embedded in the Kr is size-insensitive under high confining pressure. Meanwhile, Kr is predicted to exhibit a rate-dependent pressure-induced nanostructural transition. The nature of the resulting nanostructure is affected by the presence, size, and shape of Cu inclusion. For low pressure-loading rate, the stress state in Cu changes from hydrodynamic to non-hydrodynamic; the onset of the change appears to be correlated with the formation of a long-range orthotropic hcp/fcc layered nanostructure that forms in the Kr. The factors affecting this transition appear to include the Cu inclusion geometry and interactions at the hard-soft material interface.

- Based on the coupled DPD/MPM-grid model and concurrent DPD/MPM model, the dynamic and impact responses of discrete nanostructures have been performed. It was shown that the DPD details can be effectively coarse grained through the use of a coarse MPM background grid (the DPD/MPM-grid model) while the concurrent link between the MPM and DPD enables the near-seamless integration of constitutive modeling at the continuum level with force-based modeling at the mesoparticle level (the DPD/MPM model). The elastic responses predicted by the proposed procedure are reasonable. For both the impact and tension problems, the multi-scale simulation can

predict close values of wave speed as well as the elastic modulus that are comparable to those obtained from all-atom MD simulation and DPD-only simulation, which demonstrates that the proposed particle-based concurrent DPD/MPM model has the capability of predicting certain reasonable mechanical properties of the materials and structures.

- The application of the proposed particle-based multi-scale simulation procedure has been explored to the study of nanostructure assembly in the confining fluid at various pressure levels. By using the concurrent model, the hydrodynamic loading to the solid inclusions/assemblies (DPD particles) can be realized by introducing the surrounding fluid (MPM particles) described by EoS of the ideal gas. The P-V relationship has been calculated and shows that finite-size inclusions simulated with DPD/MPM model is very close to those samples simulated with MD and DPD simulations. For the model of particle-particle assembly in the confining fluid, neck width predicted by the concurrent DP/MPM model is shown to be almost the same as that obtained by using the DPD-only model. Furthermore, the computational models of particle/rod assembly with different initial arrangement under high pressure have been studied. The multi-scale simulation results shows that with the different initial positions of the components in the assembly, the deformation pattern of the nanostructure under high pressure can be varied largely. By tailoring the distance between the components, the discrete nanostructures can be assembled into a structure with some particular shapes, and a thoroughly solid-state sintering of the components can be obtained with the smallest area of entire free surface. In addition, the multi-scale simulation procedure

proposed in this work requires much less computational time than the atomistic simulations to simulate similar problems of interest.

### **7.3 Recommendations and Future Work**

The proposed particle-based multi-scale simulation procedure included in this dissertation has made a step forward in exploring the problems associated with multi-physic and multi-scale phenomena. In order to further improve this method and make it more robust to simulate more complicated and practical objects of interest, future work is recommended as following:

- **A More Accurate Mesoscale Potential for DPD Particles**

As discussed in Chapter 2, for the hierarchical bridge from MD to DPD, a model is built by coarse-graining a certain number of atoms into one mesoparticle. Based on the dissipative particle dynamics with conserved energy, an internal energy variable is defined to consider the energy exchange between the mesoparticle and its internal degrees of freedom. An optimization procedure using genetic algorithm is also developed to formulate the interaction potential between mesoparticles (Gan et al. 2014).

However, as can be found in the simulation results of the DPD-only model in Chapter 5, some basic mechanical properties, such as the yield stress and strain, are not exactly the same as those calculated by the MD simulations. It means that the coarse-grained mesoscale potential still cannot describe a good enough plastic behavior of the material. Therefore, further efforts should be made to develop a more accurate mesoscale force expression for the DPD particles, with the desirable capability of predicting more properties of the materials that are related to the plastic deformation, such as yield strength and stacking faults energy. It also should be note that the current mesoscale

particle potential has only been developed for the material of Cu. Based on the same procedure, the mesoparticle potentials for other metals and metal-oxides are expected to be formulated, which can extend the range of the application of multi-scale concurrent DPD/MPM model.

- **Coupling DPD with Other Improved Material Point Methods**

In the original material point method, the numerical error can be huge if no special treatment is used when the material point moves across the cell boundary, due to the discontinuity of the derivative of the linear shape function. In the past, some nonlocal mapping procedures have been developed to avoid the cell-crossing error. One of them is called as Dual Domain Material Point (DDMP) method (Zhang, Ma, and Giguere 2011). In this numerical scheme, only a modified calculation of the gradient enlarges the influence domain of a material point and node for quantities related to a gradient, while the influence domain of other quantities is unchanged from the original material point. This advantage could make it simplified and feasible to be included in the concurrent DPD/MPM method, and improve the stress calculation for the MPM region.

Some preliminary research on DDMP was also conducted in this work. For conciseness, only the results are briefly shown in Fig. 7.1. The problem geometry and computational codes can be found in Appendixes in detail. In this numerical example, the maximum particle number per cell can be 20, which means that the problem of cell-crossing can easily arise due to too many particles within one background cell. However, it can be seen that the stress profile of a 1-D problem of wave propagation becomes very smooth by using DDMP. This indicates that the cell-crossing problem can efficiently avoided by using the DDMP scheme. Although the MPM simulation is able to predict a

similar wave speed and stress values, the stress profile still shows many small oscillations. If too many particles are within one cell, and particles are able to pass through the cell boundaries easily even for a small loading increment, the numerical noise still cannot be eliminated by using the original MPM. Therefore, effort should be made in future to coupling DDMP into the concurrent DPD/MPM model to improve the calculation of internal force and velocity gradient and predict a better simulation results.

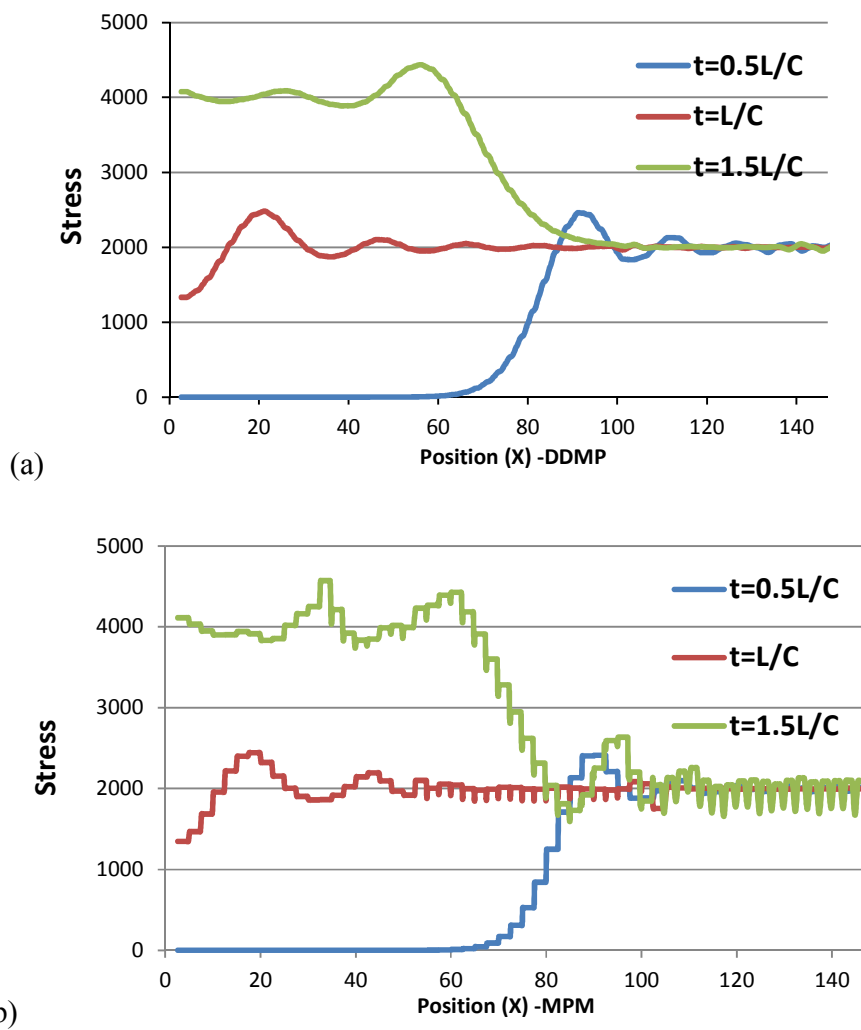


Figure 7.1 Stress profiles of a rod subject to a longitudinal force simulated with (a) DDMP and (b) MPM, respectively.  $L$  is the length and  $C$  is sound the speed in the rod.

## APPENDIXES

### Appendix 1. Units used for the Concurrent DPD/MPM Model

In the concurrent DPD/MPM model, the style of units for the DPD particles is particularly set to increase the precision for computational coding, and is similar to that adopted in the MD simulations for metals. Generally, the MPM code is dimensionless, so it will be converted into a dimensional one to be consistent with the units of DPD model.

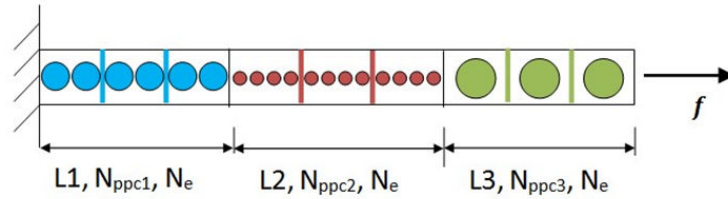
The units of the quantities specified are shown below:

- mass = grams/mole
- distance = Angstroms ( $\text{\AA}$ )
- time = picoseconds (ps)
- energy = eV
- velocity = Angstroms/picosecond ( $\text{\AA}/\text{ps}$ )
- force = eV/Angstrom ( $\text{eV}/\text{\AA}$ )
- temperature = Kelvin (K)
- pressure = bars

### Appendix 2. One-Dimensional MPM and DDMP Code for Wave Propagation

The problem geometry discussed in Section 7.3 for the MPM and DDMP is shown in Fig. A1.

Simulation Model :  
Changing the Number of Particles per Cell (Nppc)



- Total length:  $L=150$
- Three segments:  $L1=L2=L3=50$
- Number of particles per cell:  $N_{ppc1}=10$ ,  $N_{ppc2}=20$ ,  $N_{ppc3}=4$
- Number of cells per segment:  $N_e=20$
- Density:  $r = 1$
- Young's Modulus:  $E=1.0e6$
- External force:  $f=2.0e3$
- Cross-section area:  $A=1$

Figure A1. A bar subject to a tensile force. The bar is divided equally into three parts with different numbers of particles per cell (Nppc). The maximum Nppc part is in the middle of the bar where the mass of material particles are the smallest.

The computational code for MPM/DDMP is shown as following:

```
=====
% This is a one-dimension wave propagation program with the MPM.
% It was started by Luming Shen on Mar. 16 2001.
% It was designed to calculate a bar with its left end fixed and its right end exerted.
% One material point per cell is used initially. Comments were revised on 01/21/03.
% The original code is modified into MPM/DDMP code with different particle numbers
% per cell in a single computation domain, by Youqing Yang and Shan Jiang on
% Nov.6.2012
% Changing the alfa value to switch between the MPM and DDMP
% For more information about the MPM and DDMP, please refer to the following
% papers:
% D. Sulsky, Z. Chen, H.L. Schreyer, 1994, Computer methods in applied mechanics and
% engineering, vol. 118 pp.179-196.
% Z. Chen, W. Hu, L. Shen, X. Xin and and R. Brannon, 2002, Engineering Fracture
% Mechanics, vol. 69, pp. 1873-1890.
% D.Z.Zhang, X. Ma and P.T. Giguere, 2011, Journal of Computational Physics vol. 230,
% pp. 6379-6398.
close all;
clear all;
```

```

% NE=50; % number of elements; change NE to change cell size
% NE=NE*1;

NE1=20; % number of elements
NE2=20;
NE3=20;
NE=NE1+NE2+NE3;

nppc1=10; %number of particles per cell
nppc2=20;
nppc3=4;

npp=NE1*nppc1+NE2*nppc2+NE3*nppc3;

rho=1.0e0; % density
ys=1.0e6; % Young's modulus
c=sqrt(ys/rho); % wave speed
c1=0.2; c2=2.0; % form stress damping
A=1.; % cross section area of the bar
L=150.; % length of the bar

% set up the starting node
NS=2;

% set up the node number where a fixed boundary condition is applied.

fbc=NS;

% input the external force
fbn= 2.0e3; % magnitude of the external force
NB=NE+NS; % # of node on which the external force applied

dt=0.1*L/NE/c; % time step
tfinal=4.0*L/c; % total running time
ntime=round(tfinal*1.0/dt)+1; % total running steps
SIG=zeros(npp,8); % matrix to store stress of each point at each time step
xxp=zeros(npp,8); % matrix to store position of each point at each time step
history=zeros(ntime,9);history2=zeros(ntime,8);
%timep=zeros(ntime);

n1=round(ntime*1/8);n2=round(ntime*2/8);n3=round(ntime*3/8); n4=round(ntime*4/8);
n5=round(ntime*5/8);n6=round(ntime*6/8); n7=round(ntime*7/8);n8=round(ntime*8/8);
%- input nodal coordinates and connectivities

NN=round(3.0*NE); %total number of grid nodes

```

```

LOC=zeros(NN,1);
le=L/NE; % cell ( or element) size
% LOC(:)=[0:NN-1]*le; % grid node coordinates
%LOC(:)=[0:NN-1]*le; % grid node coordinates
LOC(1)=0;
for i=2:NN
LOC(i)=LOC(i-1)+le;
end
% set initial material point coordinates
xp=zeros(1,npp);

for i=1:nppc1*NE1
xp(i)=(NS-1+(i-0.5)/nppc1)*le;
end

for i=nppc1*NE1+1:nppc1*NE1+nppc2*NE2
xp(i)=LOC(NS+NE1)+((i-nppc1*NE1-0.5)/nppc2)*le;
end

for i=nppc1*NE1+nppc2*NE2+1:npp
xp(i)=LOC(NS+NE1+NE2)+((i-(nppc1*NE1+nppc2*NE2)-0.5)/nppc3)*le;
end

xp0=xp;
% xp5=(NS-1+(nppc*NE/2-0.5)/nppc)*le;
% xp9=(NS-1+(npp-0.5)/nppc)*le;
% Build global material points mass vector
MP=zeros(npp,1);

for i=1:nppc1*NE1
MP(i)=rho*A*le/nppc1;
end

for i=nppc1*NE1+1:nppc1*NE1+nppc2*NE2
MP(i)=rho*A*le/nppc2;
end

for i=nppc1*NE1+nppc2*NE2+1:npp
MP(i)=rho*A*le/nppc3;
end

% Set up initial value of Stress, Strain
ssp=zeros(npp,1); % stresses of points
snp=zeros(npp,1); % strains of points
dssp=zeros(npp,1); % stress increments of points
dsnp=zeros(npp,1); % strain increments of points

```

```

% Set up initial values of velocity, momentum, mass and external force
vg=zeros(NN,1); % velocities of node
vp=zeros(npp,1); % velocitie of points
dvp=zeros(npp,1); % velocity increments of points
fext=zeros(NN,1); % external forces on the nodes

%initialize time and step.

t=0.0;
n=1;
b=0;
rhou=rho*ones(npp,1);

% lp=0.5/nppc*le;
ssjpd=zeros(NN,1); %for gradient at nodes
% massmin=0.04*rho*A*le/nppc1;
massmin=zeros(NN,1);

for i=1:NS+NE1-1
    massmin(i)=0.04*rho*A*le/nppc1;
end

for i=NS+NE1:NS+NE1+NE2-1
    massmin(i)=rho*A*le/nppc2;
end

for i=NS+NE1+NE2:NN
    massmin(i)=rho*A*le/nppc3;
end

NC=zeros(1,npp);
xc=zeros(1,npp);
% iteration starts

while t<=tfinal*1.0/1+1.0e-9

    MVG=zeros(NN,1); % momentum at nodes
    MG=zeros(NN,1); % mass at nodes
    fint=zeros(NN,1); % internal forces at nodes
    Ffint=zeros(NN,1); % internal forces at nodes after distribution
    fb=zeros(NN,1); % body force

    % Find the number of cell in which the material point is located
    for i=1:npp

```

```

    NC(i)=fix(xp(i)/le)+1;
    xc(i)=(xp(i)-LOC(NC(i)))/le;
end

% key part of the MPM
for i=1:npp
    MG(NC(i))=MG(NC(i))+MP(i)*(1-xc(i)); % map mass from point to left grid node
    MG(NC(i)+1)=MG(NC(i)+1)+MP(i)*xc(i); % map mass from point to right grid
    node
    MVG(NC(i))=MVG(NC(i))+MP(i)*vp(i)*(1-xc(i)); % map momentum from point to
    left grid node
    MVG(NC(i)+1)=MVG(NC(i)+1)+MP(i)*vp(i)*xc(i); % map momentum from point
    to right grid node
    alfa=1.0; %
    %alfa=0.5*sin(xc(i)*pi);
    % alfa=4*(xc(i)*(1-xc(i)))^(3/2);
        %alfa=8*(xc(i)*(1-xc(i)))^(3/2);
    %alfa=4*(xc(i)*(1-xc(i)));
    alfa=alfa*MP(i)/rhou(i)*ssp(i)/le;
    fint(NC(i))=fint(NC(i))+alfa; % map internal force from point to left grid node
    fint(NC(i)+1)=fint(NC(i)+1)-alfa; % map internal force from point to right grid node
    fb(NC(i)) =fb(NC(i)) +MP(i)/rho*b*(1-xc(i)); % map body force from point to left
    grid node
    fb(NC(i)+1)=fb(NC(i)+1)+MP(i)/rho*b*xc(i); % map body force from point to right
    grid node
end
    fb(NC(npp)) =fb(NC(npp)) +fbn*A*(1-xc(i)); % apply stepwise force on particle
    then map to grid
    fb(NC(npp)+1)=fb(NC(npp)+1)+fbn*A*xc(i); % apply stepwise force on particle
    then map to grid
%modify fint using sspjd;
NS1=NC(1)+1; NB1=NC(npp)+1;
for i=NS1:NB1+1
    fint(i)=fint(i)+(sspjd(i+1)-sspjd(i-1))/2;
end

% distribute fint to small mass nodes
for i=2:NB1+1
    if MG(i-1)>massmin(i)
        coef0=0;
        else coef0=sqrt(MG(i))/(sqrt(MG(i-1))+sqrt(MG(i))+1e-12);
    end
    if MG(i)>massmin(i)
        coef1=1;
        else coef1=sqrt(MG(i))/(sqrt(MG(i-1))+sqrt(MG(i))+sqrt(MG(i+1))+1e-12);
    end
end

```

```

    if MG(i+1)>massmin(i)
        coef2=0;
        else coef2=sqrt(MG(i))/(sqrt(MG(i))+sqrt(MG(i+1))+1e-12);
    end
    Ffint(i)=coef0*fint(i-1)+coef1*fint(i)+coef2*fint(i+1);
end

%fext=fbn; %set force boundary condition
f=Ffint+fext+fb; % calculate total grid node force vector
f(fbc)=0.0; % apply the fixed boundary condition (total force=0)
MVG=MVG+f*dt; % update the momenta at the grid nodes
MVG(fbc)=0.0; % apply the fixed boundary condition (total momentun=0)

for i=1:npp
    % map the nodal velocity increment back to the pariticle
    dvp(i)=f(NC(i))*(1-xc(i))*dt/MG(NC(i))+f(NC(i+1))*xc(i)*dt/MG(NC(i+1));

    % map the current nodal velocity back to particle
    vpbar(i)=MVG(NC(i))*(1-xc(i))/MG(NC(i))+MVG(NC(i+1))*xc(i)/MG(NC(i+1));
end

vp=vp+dvp; % compute the current particle velocity
xp=xp+vpbar*dt; % compute the current particle position

% map the particle momentum back to the cell node
MVG=zeros(NN,1);
for i=1:npp
    MVG(NC(i))=MVG(NC(i))+MP(i)*vp(i)*(1-xc(i));
    MVG(NC(i+1))=MVG(NC(i+1))+MP(i)*vp(i)*xc(i);
end

% find the current nodal velocity
for i=1:npp
    vg(NC(i))=MVG(NC(i))/MG(NC(i));
    vg(NC(i+1))=MVG(NC(i+1))/MG(NC(i+1));
end

vg(fbc)=0.0; % apply the essential boundary conditions (velocity=0)

% get the strain increments from gradient of nodal velocities
NC1=NC(1);
NC9=NC(npp)+1;
x05=(LOC(NC1)+LOC(NC1+1))/2; x95=(LOC(NC9-1)+LOC(NC9))/2;

for i=1:npp
    alfa=1.00;

```

```

%alfa=0.5*sin(xc(i)*pi);
%alfa=4*(xc(i)*(1-xc(i)))^(3/2);
    %alfa=8*(xc(i)*(1-xc(i)))^(3/2);
%alfa=4*(xc(i)*(1-xc(i)));
beita=1-alfa;
dsnp(i)=alfa*(-vg(NC(i))+vg(NC(i+1)))/le;
if xp(i)<=x05 dsnp(i)=dsnp(i)+beita*(vg(NC1+1)-vg(NC1))/le;
elseif xp(i)>x95 dsnp(i)=dsnp(i)+beita*(vg(NC9)-vg(NC9-1))/le;
elseif xp(i)>x05 && xp(i)<=x95 && xc(i)<0.5 dsnp(i)=dsnp(i)+beita*(vg(NC(i+1))-
vg(NC(i-1)))/2/le;
    elseif xp(i)>x05 && xp(i)<=x95 && xc(i)>=0.5
dsnp(i)=dsnp(i)+beita*(vg(NC(i+2))-vg(NC(i)))/2/le;
    end
end
snp=snp+dsnp*dt; % update the particle strains
ssp=snp*ys; %without damping

q=zeros(npp,1);
for i=1:npp
    if dsnp(i)<0
q(i)=0.2*c*rho*abs(dsnp(i)*le)+2*rho*(dsnp(i)*le)^2;
    else
q(i)=0;
    end
end
end
ssp=ssp-q; %with damping

% stress at cell border (nodes) for DDMP,
sspjd=zeros(NN,1);
for i=1:npp
    alfa=1.00;
    %alfa=0.5*sin(xc(i)*pi);
    %alfa=4*(xc(i)*(1-xc(i)))^(3/2);
    %alfa=8*(xc(i)*(1-xc(i)))^(3/2);
    %alfa=4*(xc(i)*(1-xc(i)));
    beita=1-alfa;
    beita=beita*ssp(i)*MP(i)/rhou(i)/le;
    sspjd(NC(i))=sspjd(NC(i))+beita*(1-xc(i));
    sspjd(NC(i+1))=sspjd(NC(i+1))+beita*xc(i);

end
% for fixed boundary condition
sspjd(NC(1))=2*sspjd(NC(1));
sspjd(NC(npp)+1)=2*sspjd(NC(npp)+1);
history(n+1,1)=t+dt;
history(n+1,2)=ssp(1,1);

```

```

history(n+1,3)=ssp(round(nppc1*NE1-1),1);
history(n+1,4)=ssp(round(nppc1*NE1+0.6),1);
history(n+1,5)=ssp(round(nppc1*NE1+nppc2*NE2*2/4),1);
history(n+1,6)=ssp(round(nppc1*NE1+nppc2*NE2*2/4+0.6),1);
history(n+1,7)=ssp(round(nppc1*NE1+nppc2*NE2*2/4-1),1);
history(n+1,8)=ssp(round(nppc1*NE1+nppc2*NE2+nppc3*NE3*2/4-1),1);
history(n+1,9)=ssp(round(npp),1);

```

```

history2(n+1,1)=xp(1,1);
history2(n+1,2)=xp(1,round(nppc1*NE1-1));
history2(n+1,3)=xp(1,round(nppc1*NE1+0.6));
history2(n+1,4)=xp(1,round(nppc1*NE1+nppc2*NE2*2/4));
history2(n+1,5)=xp(1,round(nppc1*NE1+nppc2*NE2*2/4+0.6));
history2(n+1,6)=xp(1,round(nppc1*NE1+nppc2*NE2*2/4-1));
history2(n+1,7)=xp(1,round(nppc1*NE1+nppc2*NE2+nppc3*NE3*2/4-1));
history2(n+1,8)=xp(1,round(npp));

```

```

% save the new stress and output data
if n==n1
SIG(:,1)=ssp; % particle stresses at new time step
xyp(:,1)=xp'; % particle positions at new time step
end
if n==n2
SIG(:,2)=ssp; % particle stresses at new time step
xyp(:,2)=xp'; % particle positions at new time step
end
if n==n3
SIG(:,3)=ssp; % particle stresses at new time step
xyp(:,3)=xp'; % particle positions at new time step
end
if n==n4
SIG(:,4)=ssp; % particle stresses at new time step
xyp(:,4)=xp'; % particle positions at new time step
end
if n==n5
SIG(:,5)=ssp; % particle stresses at new time step
xyp(:,5)=xp'; % particle positions at new time step
end
if n==n6
SIG(:,6)=ssp; % particle stresses at new time step
xyp(:,6)=xp'; % particle positions at new time step
end
if n==n7
SIG(:,7)=ssp; % particle stresses at new time step
xyp(:,7)=xp'; % particle positions at new time step
end

```

```

    if n==n8
    SIG(:,8)=ssp; % particle stresses at new time step
    xxp(:,8)=xp'; % particle positions at new time step
    end

    %update n and t

    n=n+1;
    t=t+dt;
    %timep(n)=t;

end

% for output use only, may ignore them.
tt=linspace(0,tfinal,ntime);
xx=linspace(0,L,NE);

anax=zeros(npp); anaxx=zeros(npp);
anay=zeros(npp); anaz=zeros(npp);

% end of program

```

## Appendix 3. Publications Related to MD/DPD/MPM/FEM by the

### Author

(\* Academic advisor/Corresponding author)

#### Book Chapters

1. **Shan Jiang** and Yong Gan, “*Atomic-Level Modeling of Ultrafast Laser Interaction with Semiconductor*” (in “*Femtosecond Lasers: New Research*”, Nova Science Publishers, Inc, 2013)
2. Zhen Chen<sup>\*</sup>, **Shan Jiang**, Yong Gan, Thomas Sewell, and Donald Thompson, “*The Size Effect on the Impact Response of Nanostructure*” (in “*CRC Concise Encyclopedia of Nanotechnology*”, Taylor & Francis CRC Press, in progress)

#### Peer-Reviewed Journal Papers

1. **S. Jiang**, Y.G. Shen, Y.G. Zheng, and Z. Chen<sup>\*</sup>, Formation of quasi-icosahedral structures with multi-conjoint fivefold deformation twins in fivefold twinned metallic nanowires, *Applied Physics Letters*, 103, 041909 (2013).
2. **S. Jiang**, Y.W. Zhang<sup>\*</sup>, Y. Gan, Z. Chen<sup>\*</sup>, and P. Hao, Molecular dynamics study of neck growth in laser sintering of hollow silver nanoparticles with different heating rates, *Journal of Physics D: Applied Physics*, 46, 335302 (2013).
3. Y. Gan and **S. Jiang**, Ultrafast laser-induced premelting and structural transformation of gold nanorod, *Journal of Applied Physics*, 113, 073507 (2013).
4. **S. Jiang**, Z. Chen<sup>\*</sup>, H. Zhang, Y. Zheng, and H. Li, Impact-Induced Bending Response of the Single Crystal and Five-fold Twinned Nanowires, *International Journal for Multiscale Computational Engineering*, 11, 1-16 (2013).
5. H.T. Liu, Z. Chen<sup>\*</sup>, **S. Jiang**, Y. Gan, M.B. Liu, J.Z. Chang, and Z.H. Tong, Comparative Study of the Water Response to External Force at Nanoscale and Mesoscale. *CMES: Computer Modeling in Engineering & Sciences*, 95, 303-315 (2013).
6. Z. Chen<sup>\*</sup>, **S. Jiang**, Y. Gan, The “Inverse Hall–Petch” effect on the impact response of single crystal copper, *Acta Mechanica Sinica* 28, 1042-1048 (2012).
7. Z. Chen<sup>\*</sup>, **S. Jiang**, Y. Gan, S.Y. Oloriegbe, T.D. Sewell<sup>\*</sup>, and D.L. Thompson, Size and Aspect Ratio Effects on the Impact Response of Copper Nanobeams, *Journal of Applied Physics*, 111 113512, (2012).
8. **S. Jiang**, Z. Chen<sup>\*</sup>, Y. Gan, S.Y. Oloriegbe, T.D. Sewell<sup>\*</sup>, and D.L. Thompson, Size effects on the wave propagation and deformation pattern in copper nanobars under symmetric longitudinal impact loading, *Journal of Physics D: Applied Physics* 45 475305

(2012).

9. Y. Gan, J. Shi, and **S. Jiang**, Atomic-level study of a thickness-dependent phase change in gold thin films heated by an ultrafast laser, *Applied Optics* 51, 5946-5951 (2012).
10. Z. Chen\*, Y. Han, **S. Jiang**, Y. Gan, and T.D. Sewell, A multiscale material point method for impact simulation. *Theoretical and Applied Mechanics Letters*, 2, 051003 (2012).
11. **S. Jiang**, H. W. Zhang\*, Y.G. Zheng and Z. Chen\*, Loading path effect on the mechanical behaviour and fivefold twinning of copper nanowires, *Journal of Physics D: Applied Physics* 43, 335402 (2010).
12. **S. Jiang**, H.W. Zhang\*, Y.G. Zheng and Z. Chen, Atomistic study of the mechanical response of copper nanowires under torsion, *Journal of Physics D: Applied Physics* 42, 135408 (2009).
13. Y.G. Zheng, H.W. Zhang\*, Z. Chen and **S. Jiang**, Deformation and Stability of Copper Nanowires under Bending, *International Journal for Multiscale Computational Engineering*, 205 (2009).
14. Z. Zhang, S. Gu, M. Wang, Y. Wang, S. Wang, W. Tang, D. Zhu, J. Wu, J. Fang, **S. Jiang**, L. Dai, K. Zhan and C. Wu, Design and strength calculation of key components of main transformer and body of high-power electric locomotive, *Chinese Journal of Computational Mechanics* 26, 385 (2009). (in Chinese)
15. Z. Chen\*, **S. Jiang**, Y. Gan, H.T. Liu, T.D. Sewell, A Particle-Based Multiscale Simulation Procedure within the Material Point Method Framework, *Computational Particle Mechanics*, 2014. (Accepted)
16. H.T. Liu, **S. Jiang**, Z. Chen, M.B. Liu, J.Z. Chang, and Z.H. Tong, Mesoscale Study of a Fluid-Solid System with Inertia Effect Using Dissipative Particle Dynamics, submitted to *Microfluidics and Nanofluidics*, 2014.
17. Y. Gan, Z. Chen, **S. Jiang**, T.D. Sewell, D.L. Thompson, and S.Y. Oloriegbe, A mesoscopic-scale scheme for modeling shock wave propagation in metals, to be submitted to *Computational Particle Mechanics*, 2014.
18. Z. Chen, **S. Jiang**, T.D. Sewell, Y. Gan, S.Y. Oloriegbe, and D.L. Thompson, Rate-dependent nanostructural transition induced by soft-hard crystal interaction under high pressure, submitted to *Nano Letters*, 2014.

## REFERENCES

- Agrait, Nicolás, Alfredo Levy Yeyati, and Jan M Van Ruitenbeek. 2003. "Quantum properties of atomic-sized conductors." *Physics Reports* no. 377 (2):81-279.
- Allen, Mike P, and Dominic J Tildesley. 1989. *Computer simulation of liquids*: Oxford university press.
- An, XH, QY Lin, SD Wu, ZF Zhang, RB Figueiredo, N Gao, and TG Langdon. 2011. "The influence of stacking fault energy on the mechanical properties of nanostructured Cu and Cu–Al alloys processed by high-pressure torsion." *Scripta Materialia* no. 64 (10):954-957.
- Appell, David. 2002. "Nanotechnology: wired for success." *Nature* no. 419 (6907):553-555.
- Apperson, S, RV Shende, Senthil Subramanian, Daniel Tappmeyer, Shubhra Gangopadhyay, Z Chen, Keshab Gangopadhyay, P Redner, S Nicholich, and D Kapoor. 2007. "Generation of fast propagating combustion and shock waves with copper oxide/aluminum nanothermite composites." *Applied Physics Letters* no. 91 (24):243109-243109-3.
- Apra, Edoardo, Francesca Baletto, Riccardo Ferrando, and Alessandro Fortunelli. 2004. "Amorphization mechanism of icosahedral metal nanoclusters." *Physical review letters* no. 93 (6):065502.
- Ascencio, JA, C Gutiérrez-Wing, ME Espinosa, M Marin, S Tehuacanero, C Zorrilla, and M José-Yacamán. 1998. "Structure determination of small particles by HREM imaging: theory and experiment." *Surface science* no. 396 (1):349-368.
- Baletto, F, C Mottet, and R Ferrando. 2001. "Microscopic mechanisms of the growth of metastable silver icosahedra." *Physical Review B* no. 63 (15):155408.
- Bardenhagen, SG, and EM Kober. 2004. "The generalized interpolation material point method." *Computer Modeling in Engineering and Sciences* no. 5 (6):477-496.
- Bazant, Zdenek P, and Er-Ping Chen. 1997. "Scaling of structural failure." *Applied Mechanics Reviews* no. 50 (10):593-627.
- Berendsen, Herman JC, J Pl M Postma, Wilfred F van Gunsteren, ARHJ DiNola, and JR Haak. 1984. "Molecular dynamics with coupling to an external bath." *The Journal of chemical physics* no. 81 (8):3684-3690.

- Boek, Edo S, and Paul Van Der Schoot. 1998. "Resolution effects in dissipative particle dynamics simulations." *International Journal of Modern Physics C* no. 9 (08):1307-1318.
- Boek, ES, PV Coveney, HNW Lekkerkerker, and PPAM van der Schoot. 1997. "Simulating the rheology of dense colloidal suspensions using dissipative particle dynamics." *Physical Review E* no. 55 (3):3124.
- Branício, Paulo S., and José-Pedro Rino. 2000. "Large deformation and amorphization of Ni nanowires under uniaxial strain: a molecular dynamics study." *Physical Review B* no. 62 (24):16950.
- Bringa, E. M., J. U. Cazamias, P. Erhart, J. Stölken, N. Tanushev, B. D. Wirth, R. E. Rudd, and M. J. Caturla. 2004. "Atomistic shock Hugoniot simulation of single-crystal copper." *Journal of Applied Physics* no. 96 (7):3793-3799.
- Bringa, E. M., K. Rosolankova, R. E. Rudd, B. A. Remington, J. S. Wark, M. Duchaineau, D. H. Kalantar, J. Hawreliak, and J. Belak. 2006. "Shock deformation of face-centred-cubic metals on subnanosecond timescales." *Nature materials* no. 5 (10):805-809.
- Buffat, Philippe-André, Marc Flüeli, Roland Spycher, Pierre Stadelmann, and Jean-Pierre Borel. 1991. "Crystallographic structure of small gold particles studied by high-resolution electron microscopy." *Faraday Discussions* no. 92:173-187.
- Cao, AJ, and YG Wei. 2006a. "Formation of fivefold deformation twins in nanocrystalline face-centered-cubic copper based on molecular dynamics simulations." *Applied physics letters* no. 89 (4):041919.
- Cao, AJ, YG Wei, and Scott X Mao. 2007. "Deformation mechanisms of face-centered-cubic metal nanowires with twin boundaries." *Applied physics letters* no. 90 (15):151909.
- Cao, Ajing, and Yueguang Wei. 2006b. "Atomistic simulations of the mechanical behavior of fivefold twinned nanowires." *Physical Review B* no. 74 (21):214108.
- Chang, Pai-Chun, Zhiyong Fan, Dawei Wang, Wei-Yu Tseng, Wen-An Chiou, Juan Hong, and Jia G Lu. 2004. "ZnO nanowires synthesized by vapor trapping CVD method." *Chemistry of materials* no. 16 (24):5133-5137.
- Chau, R., J. Stölken, P. Asoka-Kumar, M. Kumar, and N. C. Holmes. 2010. "Shock Hugoniot of single crystal copper." *Journal of Applied Physics* no. 107 (2):023506.
- Chen, JK, JE Beraun, R Roybal, and DY Tzou. 2004. "Nano-to microscale modeling by cluster potentials." *Journal of thermophysics and heat transfer* no. 18 (2):253-262.

- Chen, Shuo, Nhan Phan-Thien, Boo Cheong Khoo, and Xi Jun Fan. 2006. "Flow around spheres by dissipative particle dynamics." *Physics of Fluids (1994-present)* no. 18 (10):103605.
- Chen, Z. 1996. "Continuous and discontinuous failure modes." *Journal of engineering mechanics* no. 122 (1):80-82.
- Chen, Z, R Feng, X Xin, and L Shen. 2003. "A computational model for impact failure with shear - induced dilatancy." *International journal for numerical methods in engineering* no. 56 (14):1979-1997.
- Chen, Z, W Hu, L Shen, X Xin, and R Brannon. 2002. "An evaluation of the MPM for simulating dynamic failure with damage diffusion." *Engineering Fracture Mechanics* no. 69 (17):1873-1890.
- Chen, Zhen, Yilong Han, Shan Jiang, Yong Gan, and Thomas D Sewell. 2012. "A multiscale material point method for impact simulation." *Theoretical and Applied Mechanics Letters* no. 2 (5):051003.
- Chen, Zhen, Shan Jiang, and Yong Gan. 2012. "The "Inverse Hall–Petch" effect on the impact response of single crystal copper." *Acta Mechanica Sinica* no. 28 (4):1042-1048.
- Chen, Zhen, Shan Jiang, Yong Gan, YS Oloriegbe, Thomas D Sewell, and Donald L Thompson. 2012. "Size effects on the impact response of copper nanobeams." *Journal of Applied Physics* no. 111 (11):113512.
- Cheung, Kin S, and Sidney Yip. 1991. "Atomic - level stress in an inhomogeneous system." *Journal of Applied Physics* no. 70 (10):5688-5690.
- Clausius, Rudolf. 1870. "XVI. On a mechanical theorem applicable to heat." *The London, Edinburgh, and Dublin Philosophical Magazine and Journal of Science* no. 40 (265):122-127.
- Cleveland, Charles L, Uzi Landman, Thomas G Schaaff, Marat N Shafigullin, Peter W Stephens, and Robert L Whetten. 1997. "Structural evolution of smaller gold nanocrystals: The truncated decahedral motif." *Physical review letters* no. 79 (10):1873-1876.
- Cleveland, Charles L, WD Luedtke, and Uzi Landman. 1998. "Melting of gold clusters: Icosahedral precursors." *Physical review letters* no. 81 (10):2036.
- Davidson, Alistair J, Raja Chellappa, S, Dana M Dattelbaum, and Choong-Shik Yoo. 2011. "Pressure Induced Isostructural Metastable Phase Transition of Ammonium Nitrate." *The Journal of Physical Chemistry A* no. 115 (42):11889-11896.
- Daw, Murray S, and Mi I Baskes. 1984. "Embedded-atom method: Derivation and application to impurities, surfaces, and other defects in metals." *Physical Review B* no. 29 (12):6443.

- Dreizin, Edward L. 2009. "Metal-based reactive nanomaterials." *Progress in Energy and Combustion Science* no. 35 (2):141-167.
- Espanol, Pep, and Patrick Warren. 1995. "Statistical mechanics of dissipative particle dynamics." *EPL (Europhysics Letters)* no. 30 (4):191.
- Faken, Daniel, and Hannes Jónsson. 1994. "Systematic analysis of local atomic structure combined with 3D computer graphics." *Computational Materials Science* no. 2 (2):279-286.
- Foiles, SM, MI Baskes, and MS Daw. 1986. "Embedded-atom-method functions for the fcc metals Cu, Ag, Au, Ni, Pd, Pt, and their alloys." *Physical Review B* no. 33 (12):7983.
- Gan, Yong, Zhen Chen, K Gangopadhyay, A Bezmelnitsyn, and S Gangopadhyay. 2010. "An equation of state for the detonation product of copper oxide/aluminum nanothermite composites." *Journal of Nanoparticle Research* no. 12 (3):719-726.
- Gan, Yong, Zhen Chen, Shan Jiang, Thomas D Sewell, Donald L Thompson, and Suleiman Y Oloriegbe. 2014. "A mesoscopic-scale scheme for modeling shock wave propagation in metals." *Computational Particle Method* no. To be submitted.
- Gan, Yong, and Shan Jiang. 2013. "Ultrafast laser-induced premelting and structural transformation of gold nanorod." *Journal of Applied Physics* no. 113 (7):073507-073507-5.
- Gan, Yong, Jixiang Shi, and Shan Jiang. 2012. "Atomic-level study of a thickness-dependent phase change in gold thin films heated by an ultrafast laser." *Applied optics* no. 51 (24):5946-5951.
- Gryaznov, V. G., J. Heydenreich, A. M. Kaprelov, S. A. Nepijko, A. E. Romanov, and J. Urban. 1999. "Pentagonal symmetry and disclinations in small particles." *Crystal Research and Technology* no. 34 (9):1091-1119.
- Guilkey, JE, and JA Weiss. 2003. "Implicit time integration for the material point method: Quantitative and algorithmic comparisons with the finite element method." *International Journal for Numerical Methods in Engineering* no. 57 (9):1323-1338.
- Han, W. Z., Q. An, S. N. Luo, T. C. Germann, D. L. Tonks, and W. A. Goddard Iii. 2012. "Deformation and spallation of shocked Cu bicrystals with  $\Sigma$  3 coherent and symmetric incoherent twin boundaries." *Physical Review B* no. 85 (2):024107.
- He, Lan, Thomas D. Sewell, and Donald L. Thompson. 2011. "Molecular dynamics simulations of shock waves in oriented nitromethane single crystals." *The Journal of chemical physics* no. 134 (12):124506.
- Hofmeister, H. 1998. "Forty years study of fivefold twinned structures in small particles and thin films." *Crystal Research and Technology* no. 33 (1):3-25.

- Holian, Brad Lee, and Peter S. Lomdahl. 1998. "Plasticity induced by shock waves in nonequilibrium molecular-dynamics simulations." *Science* no. 280 (5372):2085-2088.
- Hoogerbrugge, PJ, and JMVA Koelman. 1992. "Simulating microscopic hydrodynamic phenomena with dissipative particle dynamics." *EPL (Europhysics Letters)* no. 19 (3):155.
- Hoover, William G. 1985. "Canonical dynamics: equilibrium phase-space distributions." *Physical Review A* no. 31 (3):1695.
- Ikeda, Hideyuki, Yue Qi, Tahir Cagin, Konrad Samwer, William L Johnson, and William A Goddard III. 1999. "Strain rate induced amorphization in metallic nanowires." *Physical Review Letters* no. 82 (14):2900.
- Jiang, Shan. 2013. *Modeling and Simulation of the Low-Dimensional Metallic Single Crystal Nano-Structural Response under Extreme Loading*. Ph.D. Dissertation, Dalian University of Technology.
- Jiang, Shan, Zhen Chen, Yong Gan, Suleiman Y Oloriegbe, Thomas D Sewell, and Donald L Thompson. 2012. "Size effects on the wave propagation and deformation pattern in copper nanobars under symmetric longitudinal impact loading." *Journal of Physics D: Applied Physics* no. 45 (47):475305.
- Jiang, Shan, Zhen Chen, Hongwu Zhang, Yonggang Zheng, and Hao Li. 2013. "Impact-induced bending response of single crystal and five-fold twinned nanowires." *International Journal for Multiscale Computational Engineering* no. 11 (1).
- Jiang, Shan, Yonggang Shen, Yonggang Zheng, and Zhen Chen. 2013. "Formation of quasi-icosahedral structures with multi-conjoint fivefold deformation twins in fivefold twinned metallic nanowires." *Applied Physics Letters* no. 103 (4):041909.
- Jiang, Shan, Hongwu Zhang, Yonggang Zheng, and Zhen Chen. 2009. "Atomistic study of the mechanical response of copper nanowires under torsion." *Journal of Physics D: Applied Physics* no. 42:135408.
- Jiang, Shan, Hongwu Zhang, Yonggang Zheng, and Zhen Chen. 2010. "Loading path effect on the mechanical behaviour and fivefold twinning of copper nanowires." *Journal of Physics D: Applied Physics* no. 43:335402.
- Jiang, Shan, Yuwen Zhang, Yong Gan, Zhen Chen, and Hao Peng. 2013. "Molecular dynamics study of neck growth in laser sintering of hollow silver nanoparticles with different heating rates." *Journal of Physics D: Applied Physics* no. 46 (33):335302.
- Kang, Jeong-Won, and Ho-Jung Hwang. 2001. "Mechanical deformation study of copper nanowire using atomistic simulation." *Nanotechnology* no. 12 (3):295.

- Kim, Changwook, Wenhua Gu, Martha Briceno, Ian M Robertson, Hyungsoo Choi, and Kyekyoon Kevin Kim. 2008. "Copper Nanowires with a Five - Twinned Structure Grown by Chemical Vapor Deposition." *Advanced Materials* no. 20 (10):1859-1863.
- Kim, Jae Mo, and Ronald J Phillips. 2004. "Dissipative particle dynamics simulation of flow around spheres and cylinders at finite Reynolds numbers." *Chemical engineering science* no. 59 (20):4155-4168.
- Koh, S. J. A., and H. P. Lee. 2006. "Molecular dynamics simulation of size and strain rate dependent mechanical response of FCC metallic nanowires." *Nanotechnology* no. 17 (14):3451.
- Koh, SJA, HP Lee, C Lu, and QH Cheng. 2005. "Molecular dynamics simulation of a solid platinum nanowire under uniaxial tensile strain: Temperature and strain-rate effects." *Physical Review B* no. 72 (8):085414.
- Kondo, Yukihiro, and Kunio Takayanagi. 2000. "Synthesis and characterization of helical multi-shell gold nanowires." *Science* no. 289 (5479):606-608.
- Lee, Sangjin, Byeongyong Lee, and Maenghyo Cho. 2010. "Compressive pseudoelastic behavior in copper nanowires." *Physical Review B* no. 81 (22):224103.
- Li, Jingbo, and Lin-Wang Wang. 2003. "Shape effects on electronic states of nanocrystals." *Nano Letters* no. 3 (10):1357-1363.
- Li, Yanguang, Bing Tan, and Yiyang Wu. 2006. "Freestanding mesoporous quasi-single-crystalline Co<sub>3</sub>O<sub>4</sub> nanowire arrays." *Journal of the american chemical society* no. 128 (44):14258-14259.
- Liang, Wuwei, and Min Zhou. 2005. "Pseudoelasticity of single crystalline Cu nanowires through reversible lattice reorientations." *Journal of Engineering Materials and Technology* no. 127 (4):423-433.
- Liao, XZ, YH Zhao, SG Srinivasan, YT Zhu, RZ Valiev, and DV Gunderov. 2004. "Deformation twinning in nanocrystalline copper at room temperature and low strain rate." *Applied physics letters* no. 84 (4):592-594.
- Lieber, Charles M. 2003. "Nanoscale science and technology: building a big future from small things." *Mrs Bulletin* no. 28 (07):486-491.
- Lin, Yuan-Ching, and Dar-Jen Pen. 2007. "Analogous mechanical behaviors in  $\langle 100 \rangle$  and  $\langle 110 \rangle$  directions of Cu nanowires under tension and compression at a high strain rate." *Nanotechnology* no. 18 (39):395705.
- Lisal, Martin, John K Brennan, and William R Smith. 2006. "Mesoscale simulation of polymer reaction equilibrium: Combining dissipative particle dynamics with reaction ensemble Monte Carlo. I. Polydispersed polymer systems." *The Journal of chemical physics* no. 125 (16):164905.

- Lisiecki, I, A Filankembo, H Sack-Kongehl, K Weiss, M-P Pileni, and J Urban. 2000. "Structural investigations of copper nanorods by high-resolution TEM." *Physical Review B* no. 61 (7):4968.
- Liu, Yan, Han-Kui Wang, and Xiong Zhang. 2013. "A multiscale framework for high-velocity impact process with combined material point method and molecular dynamics." *International Journal of Mechanics and Materials in Design* no. 9 (2):127-139.
- Liu, Yunhong, Jianwei Zhao, and Fenying Wang. 2009. "Influence of length on shock-induced breaking behavior of copper nanowires." *Physical Review B* no. 80 (11):115417.
- Liu, Zuqin, Daihua Zhang, Song Han, Chao Li, Bo Lei, Weigang Lu, Jiye Fang, and Chongwu Zhou. 2005. "Single crystalline magnetite nanotubes." *Journal of the American Chemical Society* no. 127 (1):6-7.
- Lu, H, NP Daphalapurkar, B Wang, S Roy, and R Komanduri. 2006. "Multiscale simulation from atomistic to continuum–coupling molecular dynamics (MD) with the material point method (MPM)." *Philosophical Magazine* no. 86 (20):2971-2994.
- Luo, Sheng-Nian, Timothy C. Germann, Tapan G. Desai, Davis L. Tonks, and Qi An. 2010. "Anisotropic shock response of columnar nanocrystalline Cu." *Journal of Applied Physics* no. 107 (12):123507.
- Luo, Sheng-Nian, Timothy C. Germann, and Davis L. Tonks. 2009. "Spall damage of copper under supported and decaying shock loading." *Journal of Applied Physics* no. 106 (12):123518.
- Ma, J, H Lu, B Wang, S Roy, R Hornung, A Wissink, and R Komanduri. 2005. "Multiscale simulations using generalized interpolation material point (GIMP) method and SAMRAI parallel processing." *CMES: Computer Modeling in Engineering & Sciences* no. 8 (2):135-152.
- McDowell, Matthew T, Austin M Leach, and Ken Gall. 2008. "Bending and tensile deformation of metallic nanowires." *Modelling Simul. Mater. Sci. Eng.* no. 16 (4):5003.
- Mehendale, Bhushan, Rajesh Shende, Senthil Subramanian, Shubhra Gangopadhyay, Paul Redner, Deepak Kapoor, and Steven Nicolich. 2006. "Nanoenergetic composite of mesoporous iron oxide and aluminum nanoparticles." *Journal of Energetic Materials* no. 24 (4):341-360.
- Mishin, Yu, MJ Mehl, DA Papaconstantopoulos, AF Voter, and JD Kress. 2001. "Structural stability and lattice defects in copper: Ab initio, tight-binding, and embedded-atom calculations." *Physical Review B* no. 63 (22):224106.

- Nam, H-S, Nong M Hwang, BD Yu, and J-K Yoon. 2002. "Formation of an icosahedral structure during the freezing of gold nanoclusters: surface-induced mechanism." *Physical review letters* no. 89 (27):275502.
- Nix, William D, and Huajian Gao. 1998. "Indentation size effects in crystalline materials: a law for strain gradient plasticity." *Journal of the Mechanics and Physics of Solids* no. 46 (3):411-425.
- Nosé, Shuichi. 1984. "A unified formulation of the constant temperature molecular dynamics methods." *The Journal of Chemical Physics* no. 81 (1):511-519.
- Ohnishi, Hideaki, Yukihiro Kondo, and Kunio Takayanagi. 1998. "Quantized conductance through individual rows of suspended gold atoms." *Nature* no. 395 (6704):780-783.
- Park, Harold S, and Jonathan A Zimmerman. 2005. "Modeling inelasticity and failure in gold nanowires." *Physical Review B* no. 72 (5):054106.
- Plimpton, Steve. 1995. "Fast parallel algorithms for short-range molecular dynamics." *Journal of Computational Physics* no. 117 (1):1-19.
- Qu, Liangti, Gaoquan Shi, Xufeng Wu, and B Fan. 2004. "Facile route to silver nanotubes." *Advanced Materials* no. 16 (14):1200-1203.
- Rahman, A. 1964. "Correlations in the motion of atoms in liquid argon." *Physical Review* no. 136 (2A):A405.
- Rohatgi, Aashish, Kenneth S. Vecchio, and George T. Gray Iii. 2001. "The influence of stacking fault energy on the mechanical behavior of Cu and Cu-Al alloys: Deformation twinning, work hardening, and dynamic recovery." *Metallurgical and Materials Transactions A* no. 32 (1):135-145.
- Rossi, Carole, Kaili Zhang, Daniel Esteve, Pierre Alphonse, Philippe Tailhades, and Constantin Vahlas. 2007. "Nanoenergetic materials for MEMS: a review." *Microelectromechanical Systems, Journal of* no. 16 (4):919-931.
- Rowlinson, John Shipley, and Benjamin Widom. 2002. *Molecular theory of capillarity*. Vol. 8: Courier Dover Publications.
- Sadeghirad, A, RM Brannon, and J Burghardt. 2011. "A convected particle domain interpolation technique to extend applicability of the material point method for problems involving massive deformations." *International Journal for Numerical Methods in Engineering* no. 86 (12):1435-1456.
- San-Miguel, Alfonso. 2006. "Nanomaterials under high-pressure." *Chemical Society Reviews* no. 35 (10):876-889.
- Service, RF. 2001. "Breakthrough of the year. Molecules get wired." *Science (New York, NY)* no. 294 (5551):2442.

- Seryogin, George, Ilan Shalish, Warren Moberlychan, and Venkatesh Narayanamurti. 2005. "Catalytic hydride vapour phase epitaxy growth of GaN nanowires." *Nanotechnology* no. 16 (10):2342.
- Shen, Tong, YongQuan Wu, and XiongGang Lu. 2013. "Structural evolution of five-fold twins during the solidification of Fe5601 nanoparticle: a molecular dynamics simulation." *Journal of molecular modeling* no. 19 (2):751-755.
- Shimizu, H., N. Saitoh, and S. Sasaki. 1998. "High-pressure elastic properties of liquid and solid krypton to 8 GPa." *Physical Review B* no. 57 (1):230.
- Siavosh-Haghighi, Ali, Richard Dawes, Thomas D. Sewell, and Donald L. Thompson. 2009. "Shock-induced melting of (100)-oriented nitromethane: Structural relaxation." *The Journal of chemical physics* no. 131 (6):064503.
- Sofos, Filippou, Theodoros Karakasidis, and Antonios Liakopoulos. 2009. "Transport properties of liquid argon in krypton nanochannels: anisotropy and non-homogeneity introduced by the solid walls." *International Journal of Heat and Mass Transfer* no. 52 (3):735-743.
- Stoltz, G. 2006. "A reduced model for shock and detonation waves. I. The inert case." *EPL (Europhysics Letters)* no. 76 (5):849.
- Sulsky, Deborah, Zhen Chen, and Howard L Schreyer. 1994. "A particle method for history-dependent materials." *Computer Methods in Applied Mechanics and Engineering* no. 118 (1):179-196.
- Sun, XM, and YD Li. 2005. "Cylindrical silver nanowires: preparation, structure, and optical properties." *Advanced Materials* no. 17 (21):2626-2630.
- Sutton, AP, and J Chen. 1990. "Long-range finnis–sinclair potentials." *Philosophical Magazine Letters* no. 61 (3):139-146.
- Tan, EPS, Y Zhu, T Yu, L Dai, CH Sow, VBC Tan, and CT Lim. 2007. "Crystallinity and surface effects on Young's modulus of CuO nanowires." *Applied physics letters* no. 90 (16):163112.
- Tanguy, D., Michel Mareschal, Peter S. Lomdahl, Timothy C. Germann, Brad Lee Holian, and Ramon Ravelo. 2003. "Dislocation nucleation induced by a shock wave in a perfect crystal: Molecular dynamics simulations and elastic calculations." *Physical Review B* no. 68 (14):144111.
- Tsuzuki, Helio, Paulo S. Branicio, and José P. Rino. 2007. "Structural characterization of deformed crystals by analysis of common atomic neighborhood." *Computer physics communications* no. 177 (6):518-523.
- Uchic, Michael D, Dennis M Dimiduk, Jeffrey N Florando, and William D Nix. 2004. "Sample dimensions influence strength and crystal plasticity." *Science* no. 305 (5686):986-989.

- Van Swygenhoven, H, M Spaczer, A Caro, and D Farkas. 1999. "Competing plastic deformation mechanisms in nanophase metals." *Physical Review B* no. 60 (1):22.
- Verheijen, Marcel A, George Immink, Thierry de Smet, Magnus T Borgström, and Erik PAM Bakkers. 2006. "Growth kinetics of heterostructured GaP-GaAs nanowires." *Journal of the American Chemical Society* no. 128 (4):1353-1359.
- Wang, Yanting, S Teitel, and Christoph Dellago. 2005. "Melting of icosahedral gold nanoclusters from molecular dynamics simulations." *The Journal of chemical physics* no. 122 (21):214722.
- Wen, Yu-Hua, Rao Huang, Zi-Zhong Zhu, and Quan Wang. 2012. "Mechanical properties of platinum nanowires: An atomistic investigation on single-crystalline and twinned structures." *Computational Materials Science* no. 55:205-210.
- Wu, Bin, Andreas Heidelberg, and John J Boland. 2005. "Mechanical properties of ultrahigh-strength gold nanowires." *Nature materials* no. 4 (7):525-529.
- Wu, Bin, Andreas Heidelberg, John J Boland, John E Sader, XiaoMing Sun, and YaDong Li. 2006. "Microstructure-hardened silver nanowires." *Nano letters* no. 6 (3):468-472.
- Wu, J. Y., S. Nagao, J. Y. He, and Z. L. Zhang. 2011. "Role of five-fold twin boundary on the enhanced mechanical properties of fcc Fe nanowires." *Nano letters* no. 11 (12):5264-5273.
- Wu, X, G Ma, and Y Xia. 2005. "Propagation of Elastic Wave in Single-crystal Nano Copper Bar." *Acta Metallurgica Sinica* no. 4 (10):1037-1041.
- Yoo, Jun Hwan, Soo Ik Oh, and Myeong Sik Jeong. 2010. "The enhanced elastic modulus of nanowires associated with multitwins." *Journal of Applied Physics* no. 107 (9):094316.
- Yu, Shufang, Sang Bok Lee, and Charles R Martin. 2003. "Electrophoretic protein transport in gold nanotube membranes." *Analytical chemistry* no. 75 (6):1239-1244.
- Zhang, Duan Z, Xia Ma, and Paul T Giguere. 2011. "Material point method enhanced by modified gradient of shape function." *Journal of Computational Physics* no. 230 (16):6379-6398.
- Zheng, YG, HW Zhang, Z Chen, L Wang, ZQ Zhang, and JB Wang. 2008. "Formation of two conjoint fivefold deformation twins in copper nanowires with molecular dynamics simulation." *Applied Physics Letters* no. 92 (4):041913.
- Zheng, Yonggang, Hongwu Zhang, Zhen Chen, and Shan Jiang. 2009. "Deformation and Stability of Copper Nanowires under Bending." *International Journal for Multiscale Computational Engineering* no. 7 (3).

- Zhou, Shijian, John Stormont, and Zhen Chen. 1999. "Simulation of geomembrane response to settlement in landfills by using the material point method." *International journal for numerical and analytical methods in geomechanics* no. 23 (15):1977-1994.
- Zhu, Liangfang, Xiaoshuang Shen, Zhiyuan Zeng, Hong Wang, Hua Zhang, and Hongyu Chen. 2012. "Induced coiling action: exploring the intrinsic defects in five-fold twinned silver nanowires." *ACS nano* no. 6 (7):6033-6039.
- Zhu, YT, XL Wu, XZ Liao, J Narayan, SN Mathaudhu, and LJ Kecskes. 2009. "Twinning partial multiplication at grain boundary in nanocrystalline fcc metals." *Applied Physics Letters* no. 95 (3):031909.
- Zope, Rajendra R., and Yu Mishin. 2003. "Interatomic potentials for atomistic simulations of the Ti-Al system." *Physical Review B* no. 68 (2):024102.

## VITA

Shan Jiang was born in Dalian, China. He attended Dalian University of Technology, a top ranked academic institution in China, and received a B.S. in Engineering Mechanics in 2007 and a M.S. in Computational Mechanics in 2009. He began work toward a Ph.D. in Structural Engineering in the Department of Civil and Environmental Engineering, at the University of Missouri-Columbia College of Engineering, in Spring 2010. During this time, he also earned another Ph.D. degree in Computational Mechanics in Summer 2013 for a joint-degree program at Dalian University of Technology.

His research interests are broadly in the areas of Computational Mechanics, Solid Mechanics, Structural Engineering, Nano-mechanics and Multiscale Simulations. Work experience includes working as a research assistant in State Key Laboratory of Structural Analysis for Industrial Equipment at Dalian University of Technology, and in the Department of Civil and Environmental Engineering at the University of Missouri-Columbia. His research is funded by NSFC and DTRA grants with the principle investigators Prof. Zhen Chen, Prof. Thomas D. Sewell, and Prof. Donald L. Thompson. So far he has co-authored two book chapters and more than 15 peer-reviewed journal papers. He is a member of American Society of Civil Engineers, American Society of Mechanical Engineers, and United States Association for Computational Mechanics (ASCE, ASME, USACM).